International Journal of Physical Sciences

Volume 8 Number 37, 9 October, 2013
ISSN 1992-1950

Academic Journals

ABOUT IJPS

The **International Journal of Physical Sciences (IJPS)** is published weekly (one volume per year) by Academic Journals.

International Journal of Physical Sciences (IJPS) is an open access journal that publishes high-quality solicited and unsolicited articles, in English, in all Physics and chemistry including artificial intelligence, neural processing, nuclear and particle physics, geophysics, physics in medicine and biology, plasma physics, semiconductor science and technology, wireless and optical communications, materials science, energy and fuels, environmental science and technology, combinatorial chemistry, natural products, molecular therapeutics, geochemistry, cement and concrete research, metallurgy, crystallography and computer-aided materials design. All articles published in IJPS are peer-reviewed.

Submission of Manuscript

Submit manuscripts as e-mail attachment to the Editorial Office at: ijps@academicjournals.org. A manuscript number will be mailed to the corresponding author shortly after submission.

For all other correspondence that cannot be sent by e-mail, please contact the editorial office (at ijps@academicjournals.org).

The International Journal of Physical Sciences will only accept manuscripts submitted as e-mail attachments.

Please read the **Instructions for Authors** before submitting your manuscript. The manuscript files should be given the last name of the first author.

Editorial Board

Instructions for Author

Electronic submission of manuscripts is strongly encouraged, provided that the text, tables, and figures are included in a single Microsoft Word file (preferably in Arial font).

The **cover letter** should include the corresponding author's full address and telephone/fax numbers and should be in an e-mail message sent to the Editor, with the file, whose name should begin with the first author's surname, as an attachment.

Article Types

Three types of manuscripts may be submitted:

Regular articles: These should describe new and carefully confirmed findings, and experimental procedures should be given in sufficient detail for others to verify the work. The length of a full paper should be the minimum required to describe and interpret the work clearly.

Short Communications: A Short Communication is suitable for recording the results of complete small investigations or giving details of new models or hypotheses, innovative methods, techniques or apparatus. The style of main sections need not conform to that of full-length papers. Short communications are 2 to 4 printed pages (about 6 to 12 manuscript pages) in length.

Reviews: Submissions of reviews and perspectives covering topics of current interest are welcome and encouraged. Reviews should be concise and no longer than 4-6 printed pages (about 12 to 18 manuscript pages). Reviews are also peer-reviewed.

Review Process

All manuscripts are reviewed by an editor and members of the Editorial Board or qualified outside reviewers. Authors cannot nominate reviewers. Only reviewers randomly selected from our database with specialization in the subject area will be contacted to evaluate the manuscripts. The process will be blind review.

Decisions will be made as rapidly as possible, and the journal strives to return reviewers' comments to authors as fast as possible. The editorial board will re-review manuscripts that are accepted pending revision. It is the goal of the IJPS to publish manuscripts within weeks after submission.

Regular articles

All portions of the manuscript must be typed double-spaced and all pages numbered starting from the title page.

The Title should be a brief phrase describing the contents of the paper. The Title Page should include the authors' full names and affiliations, the name of the corresponding author along with phone, fax and E-mail information. Present addresses of authors should appear as a footnote.

The Abstract should be informative and completely self-explanatory, briefly present the topic, state the scope of the experiments, indicate significant data, and point out major findings and conclusions. The Abstract should be 100 to 200 words in length.. Complete sentences, active verbs, and the third person should be used, and the abstract should be written in the past tense. Standard nomenclature should be used and abbreviations should be avoided. No literature should be cited.

Following the abstract, about 3 to 10 key words that will provide indexing references should be listed.

A list of non-standard **Abbreviations** should be added. In general, non-standard abbreviations should be used only when the full term is very long and used often. Each abbreviation should be spelled out and introduced in parentheses the first time it is used in the text. Only recommended SI units should be used. Authors should use the solidus presentation (mg/ml). Standard abbreviations (such as ATP and DNA) need not be defined.

The Introduction should provide a clear statement of the problem, the relevant literature on the subject, and the proposed approach or solution. It should be understandable to colleagues from a broad range of scientific disciplines.

Materials and methods should be complete enough to allow experiments to be reproduced. However, only truly new procedures should be described in detail; previously published procedures should be cited, and important modifications of published procedures should be mentioned briefly. Capitalize trade names and include the manufacturer's name and address. Subheadings should be used. Methods in general use need not be described in detail.

Results should be presented with clarity and precision. The results should be written in the past tense when describing findings in the authors' experiments. Previously published findings should be written in the present tense. Results should be explained, but largely without referring to the literature. Discussion, speculation and detailed interpretation of data should not be included in the Results but should be put into the Discussion section.

The Discussion should interpret the findings in view of the results obtained in this and in past studies on this topic. State the conclusions in a few sentences at the end of the paper. The Results and Discussion sections can include subheadings, and when appropriate, both sections can be combined.

The Acknowledgments of people, grants, funds, etc should be brief.

Tables should be kept to a minimum and be designed to be as simple as possible. Tables are to be typed double-spaced throughout, including headings and footnotes. Each table should be on a separate page, numbered consecutively in Arabic numerals and supplied with a heading and a legend. Tables should be self-explanatory without reference to the text. The details of the methods used in the experiments should preferably be described in the legend instead of in the text. The same data should not be presented in both table and graph form or repeated in the text.

Figure legends should be typed in numerical order on a separate sheet. Graphics should be prepared using applications capable of generating high resolution GIF, TIFF, JPEG or Powerpoint before pasting in the Microsoft Word manuscript file. Tables should be prepared in Microsoft Word. Use Arabic numerals to designate figures and upper case letters for their parts (Figure 1). Begin each legend with a title and include sufficient description so that the figure is understandable without reading the text of the manuscript. Information given in legends should not be repeated in the text.

References: In the text, a reference identified by means of an author‘s name should be followed by the date of the reference in parentheses. When there are more than two authors, only the first author‘s name should be mentioned, followed by ’et al‘. In the event that an author cited has had two or more works published during the same year, the reference, both in the text and in the reference list, should be identified by a lower case letter like ’a‘ and ’b‘ after the date to distinguish the works.

Examples:

Abayomi (2000), Agindotan et al. (2003), (Kelebeni, 1983), (Usman and Smith, 1992), (Chege, 1998; 1987a,b; Tijani, 1993,1995), (Kumasi et al., 2001)

References should be listed at the end of the paper in alphabetical order. Articles in preparation or articles submitted for publication, unpublished observations, personal communications, etc. should not be included in the reference list but should only be mentioned in the article text (e.g., A. Kingori, University of Nairobi, Kenya, personal communication). Journal names are abbreviated according to Chemical Abstracts. Authors are fully responsible for the accuracy of the references.

Examples:

Ogunseitan OA (1998). Protein method for investigating mercuric reductase gene expression in aquatic environments. Appl. Environ. Microbiol. 64:695-702.

Gueye M, Ndoye I, Dianda M, Danso SKA, Dreyfus B (1997). Active N2 fixation in several Faidherbia albida provenances. Ar. Soil Res. Rehabil. 11:63-70.

Charnley AK (1992). Mechanisms of fungal pathogenesis in insects with particular reference to locusts. In: Lomer CJ, Prior C (eds) Biological Controls of Locusts and Grasshoppers: Proceedings of an international workshop held at Cotonou, Benin. Oxford: CAB International, pp 181-190.

Mundree SG, Farrant JM (2000). Some physiological and molecular insights into the mechanisms of desiccation tolerance in the resurrection plant Xerophyta viscasa Baker. In Cherry et al. (eds) Plant tolerance to abiotic stresses in Agriculture: Role of Genetic Engineering, Kluwer Academic Publishers, Netherlands, pp 201-222.

Short Communications

Short Communications are limited to a maximum of two figures and one table. They should present a complete study that is more limited in scope than is found in full-length papers. The items of manuscript preparation listed above apply to Short Communications with the following differences: (1) Abstracts are limited to 100 words; (2) instead of a separate Materials and Methods section, experimental procedures may be incorporated into Figure Legends and Table footnotes; (3) Results and Discussion should be combined into a single section.

Proofs and Reprints: Electronic proofs will be sent (e-mail attachment) to the corresponding author as a PDF file. Page proofs are considered to be the final version of the manuscript. With the exception of typographical or minor clerical errors, no changes will be made in the manuscript at the proof stage.

International Journal of Physical Sciences

Table of Contents: Volume 8 Number 37, 9 October, 2013

ARTICLES

academicJournals

Vol. 8(37), pp. 1824-1829, 9 October, 2013
DOI: 10.5897/IJPS2013.3985
ISSN 1992 - 1950 © 2013 Academic Journals
http://www.academicjournals.org/IJPS

International Journal of Physical Sciences

Review

Possible internuclear interaction of atoms

Boris A. Mosienko

Siberian Research Institute of Geology, Geophysics and Mineral Resources, Krasnii pr. 67, Novosibirsk, 630104 Russia.

Accepted 26 September, 2013

This work had been devoted to the problem of the nature of forces between molecules of second liquid. A hypothesis of the internuclear interaction of atoms was proposed. But this hypothesis turned out to be suitable also for the interpretation of the chemical covalent bond. It was offered a new model of hydrogen molecule, based on the corpuscular properties of electrons (together with the wave ones). This model did not yield to the interpretation with electromagnetic interaction, but could be explained with internuclear forces. A method of the experimental check-up of the proposed hypothesis was pointed out.

Key words: Second liquid, π-mesons, chemical covalent bond, hydrogen molecule model, proton accelerator.

INTRODUCTION

In the beginning of the 20th century liquid was considered nonstructural (that is, similar to very dense gas). But as it was proved by experiment in 1933, liquid had complicated intermolecular structure (Bernal and Fowler, 1933). This was the first important broadening of our notions of liquid. From that time on, the liquid structure is studying in many scientific laboratories of the world (Turnbull, 1952; Reichert et al., 2000).

The second broadening had been developed for a long time in some stages; it was concerned with phase transitions of the first kind, in particular, with melting. It turned out that, the melting of crystal on its surface begins at the temperature essentially more low than it was considered before. This phenomenon for the first time was noticed and studied by M. Faraday (1850), but the results of his investigations did not gain recognition at that time. The existence of this phenomenon was definitely proved experimentally in 1985 only; it was named “premelting” (Dash et al., 1995).

Premelting of ice enables one to interpret plenty of natural phenomena (the flow of glaciers, ice slippery, heaving of frozen ground etc). Investigations on these subjects were carried out now on a large scale in many countries (Bluhm et al., 2002; Engemann et al., 2004).

Author of this article has made an attempt to extend further our notions of liquid. It is considered now that, sublimation is a direct transition from solid (crystalline) state of matter into gas. The author has propounded and substantiated the principle of least time for first-order phase transition; it is shown by means of this principle that, sublimation goes in two steps through a certain intermediate state in the form of surface film. It is concluded that, this film consists of nonstructural liquid like matter which is a certain antipode of liquid; this liquid like state of matter is named “second liquid” (Mosienko, 2008, 2009).

Subsequently, the mentioned subject is continued and developed. It is assumed from theoretical reasons, that second liquid can exist in all area of ordinary liquid. The point comes to the sizes of liquid objects: if only one dimension of a liquid object does not exceed a certain critical size, it has to consist of second liquid. This conclusion ought to be of important applied significance. It is shown that the second liquid conception could throw light upon the following problems:

1) the cause of uniquity of solid nanomaterial properties;
2) the ion-induced nucleation in atmosphere;
3) some unusual properties of liquid water in nanocavities (particularly, in the cells of living organisms) (Mosienko, 2012).

The notion of second liquid cannot be completed, till the

Email: b.mosienko@ngs.ru.

problem of the nature of forces between its molecules will be solved. An assumption which contains the appropriate solution is proposed in the paper. However, it turned out that, this solution is suitable for explanation of the chemical covalent bonding. So, we have come up to more important topic (a different interpretation of covalent bond) which became the main subject of the article. The critical remarks of the existent interpretation of covalent bond have been adduced; a new model of hydrogen molecule has been presented.

ASSUMPTION ON INTERNUCLEUS FORCES

As known, the Mechanism M_1 is due to Van der Waals' (London's) forces, that is, to electromagnetic interaction. But which interaction is the Mechanism M_2 to due?

At present, four fundamental interactions of nature are known: gravitational, electromagnetic, strong nuclear and weak nuclear interaction. The gravitational interaction of atoms and molecules is insignificant, one can disregard them. The nuclear interactions display themselves inside atomic nuclei only. There is electromagnetic interaction which is left; it is known that, first of all, the existence of atoms themselves is caused by this interaction. Van der Waals' forces are due to electromagnetic interaction too. Besides, the chemical bond between atoms in molecule is explained by this interaction.

If one would suppose that, Mechanism M_2 also is due to electromagnetic interaction, the question would arise: if there is too much demand from electromagnetic interaction? But the great thing is not this quantitative aspect of the problem. The most important point is the following: liquid and second liquid are some antipodes by their physical properties, mechanisms of their intermolecular forces scarcely could be within the framework of the same fundamental interaction. So, we are forced to seek and bring in some new suitable fundamental interaction.

Could one be able to search for a source of these forces? We have a small choice:

i) Atom of any substance consists of a nucleus and surrounding electrons (electron cloud). It is considered that, Van der Waals' forces are due to the configuration of electron cloud as the element which is more light and mobile in comparison with atomic nucleus. Therefore, it is necessary to look for a source of sought-for forces in atomic nuclei.

ii) Atomic nucleus consists of protons and neutrons. It is known that, internuclear distances of molecules hydrogen (H_2) and deuterium (D_2) are equal; it is the experimental fact (Erdey-Grus, 1973). Since the D_2 atomic nucleus contains neutron, and the H_2 atomic nucleus does not contain it we may conclude that, neutrons cannot take part in the formation of sought for forces. So, this source must be found in protons. Protons (together with neutrons) are the source of nuclear forces.

The carriers of the nuclear forces are considered the virtual π-mesons with a mass of about 300 m_e, where m_e is electron mass. The effective range r of the nuclear forces is determined by the mass m of the carriers (π-mesons):

$$r = h/mc,$$

where h is Planck constant and c is the velocity of the light.

It is known that, the size of the atomic nucleus is approximately in 10^5 times less than the size of atom. Let us assume that, protons of atomic nuclei give off (together with virtual π^0-mesons) some light-weight and electroneutral virtual x^0-mesons of the mass $(300m_e)/10^5 = 0.003m_e$. In this case, we would receive a new force analogous with the nuclear force. This force operates between the nuclei of the neighboring (that is, being in contact) atoms. It might be called *internuclear force*.

CHEMICAL COVALENT BOND

It is clear that, now we cannot pass over the problem of chemical bond. Indeed, if atomic nuclei are the source of some internuclear forces, these forces must manifest themselves not only in the mutual attraction of the second liquid molecules, but still to a greater extent in the mutual attraction of atoms in molecules, since in this case, the distances between nuclei are less. Thus, we come to the possibility of existence of another source of the chemical covalent bond.

On the existent notions of covalent bond

As it is known, Schrödinger equation is the wave equation; it takes into account the wave properties of electrons only, but the corpuscular ones remain in the background. Of course, there are considered just such waves which correspond to the electron momentum; none the least, this is the wave question. Meantime, electron, first of all, is a particle and already then it is a wave.

It is considered that, to imagine a movement of electron in atom along a certain trajectory is impossible. W. Heisenberg (1927) especially insisted on this statement. But it is difficult to agree with that; many outstanding physicists (including Einstein, Planck, and Laue) considered it too categorical.

Let us consider that, electron in molecule does not lose its individuality as a particle; we accept this statement by a way of postulate. We know that, the electron trajectory in molecule cannot be determined by real experiments. But we may use this notion in imaginary experiments; moreover, we shall construct a hydrogen molecule model with the aid of this notion. Of course, it will be a

hypothetical model. However, according to Feynman (1965), the great thing is that, the consequences of our hypothesis can be compared with the results of experiments. Electron in atom has a definite wavelength, and this wavelength, according to de Broglie is given by:

$\lambda = h/mv$

where *h* is Planck constant, *m* is the mass of electron, *v* is the electron velocity. The electron wave moves with a definite and constant velocity. If electron is in unexcited state, only one wavelength gets in around the nucleus on the surface of atom. The middle of this configuration can be considered the place where electron (as a particle) is found. So, we fancy the electron trajectory in atom while imagining the uniform motion of the wave on the circumference, let us remind of the essence of existent notions of chemical covalent bond.

It is considered that, pair of shared electrons is drawn into the space between the two atomic nuclei. Here the negatively charged electrons are attracted to the positive charges of both nuclei. This overcomes the repulsion between the two positively charged nuclei of two atoms; just this overwhelming attraction is the covalent bond.

But why are the shared electrons are drawn into the internuclear space? As known, the sharing of electrons means only that, electrons are on the same energy level (that is, they move on the same orbit); of course, by this they must repel each other in accordance with Coulomb law and, therefore, to be on the utmost distance from each other. Or else, their movement must be uniform and mutually coordinated. The drawing of electrons into internuclear space (that is, their mutual attraction) contradicts Coulomb law. However, one could agree with this, taking into account that, the mutual approach of electrons leads to a decrease of the potential energy of two atomic system on the whole. Much the worse is another thing: in such a case, the uniformity and mutually coordination around nuclei would be broken. Indeed, in order to create an abundant negative charge in the space between nuclei, electrons must slow down the movement in this space. One can see from de Broglie formula that, a decrease of the electron velocity must lead to an increase of their wavelength. Such behavior of electrons seems unnatural.

The arguments adduced above, concern the corpuscular properties of electrons in molecule. Meantime, the conclusion about electrons, which are drawn into the space between two atomic nuclei, is received from Schrödinger equation which takes into account the wave properties of electrons only. Emphasize that, corpuscular-wave dualism is not ignored by this. But corpuscular properties of electrons are considered on the stage of the interpretation of Shrödinger equation solution. In our variant, they are considered on the stage of the model constructing (see the following section). This is just the significant difference of the proposed approach from the existent one.

A proposed model of hydrogen molecule

We know that molecules are very stable constructions. One could put a question: why does it happen? The completed external electron shell of atom contains two electrons with opposite spins. Helium atoms have just such shells; that's why they have high strength and practically do not deform by collisions. It is quite naturally, that electrons behave in accordance with Coulomb law (that is, are on the greatest distances from one another) and with de Broglie formula. Such behavior of electrons corresponds to minimum of its potential energies. It is known that, electron of ion H_2^+ moves around its nuclei on the trajectory in the form of an eight.

As known, the nature is simple in its own way: it does not make with much, what can be made with one. So, it is reasonable to expect that if, one will unite the said in two preceding paragraphs, it will be received a stable and strong construction of hydrogen molecule.

Let us consider this in detail. The only electron of H_2 on the lower energy level (in a unexcited state) moves around his nucleus so that the length of his wave is equal $2\pi r_0$, where r_0 is the atomic radius (Figure 1). As the electron shell is not closed, it is highly pliant and so easily deforms by collisions of atoms. Let atoms bring together (by collision) at a distance r_0 (that is, in the two times nearer than at the quiet state) and let electrons have opposite spins. In this case, each electron can begin to move along a trajectory which embraces the both nuclei; this trajectory has a form of the eight. So, atoms find themselves connected in molecule (Figure 2). Incidentally, the wavelengths of electrons (and, consequently, their velocities) do not alter; but the form of each electron orbit turns into figure-of-eight. As to the coordination of electrons movement, it consists in the following: electrons move uniformly on the same orbit and in the same direction with the relative phase shift of $\lambda/4$. One could easily understand with Figure 3 that, electrons in any time are in diametrically opposed points in respect of one another, that is, on the greatest distance from one another in accordance with Coulomb law (the distance here must be understood in an integral meaning). This transition happens spontaneously with an emission of energy 435 kJ/mol; just this value determines the bond strength of hydrogen molecule.

It is easy to understand that, a half of electron wavelength cannot form the closed construction around nucleus of individual atom: the beginning and the end of such construction cannot joint as they are in the different (opposite) phases. But this is possible for molecule: there is one half of the wave around each of atoms; besides, the beginning of the second half is in phase with the end of the first half, and the end of the second half is in phase with the beginning of the first one. Indeed, these halves

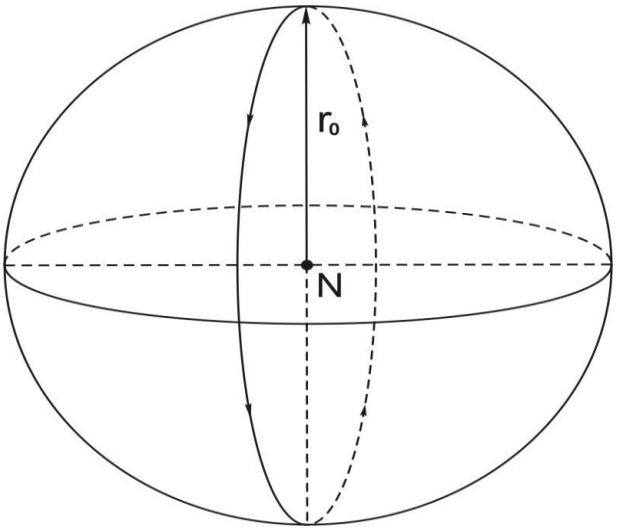

Figure 1. The model of hydrogen atom. Here, N is the nucleus of the atom, the electron orbit plane changes its disposition in the space by chance; therefore, the average density of the electron cloud on the surface of sphere is the same.

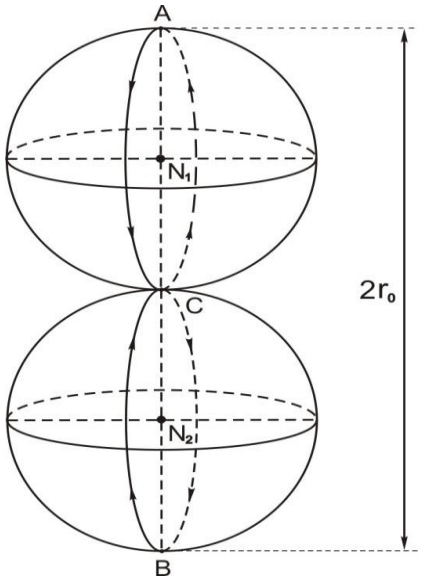

Figure 2. The model of hydrogen molecule. It is as if the two globes which are put on the same axle, here N_1 and N_2 are the nuclei of the molecule. If electron orbit plane (which has the form of an eight) rotates around the axis AB, the average density of the electron cloud must have an axial symmetry. Using by geographic terminology, one may say that this density does not depend on a meridian, but essentially depends on a latitude: it is minimal on the equators and maximal on the poles. (Pay attention, that the scales of Figures 1 and 2 are the same.)

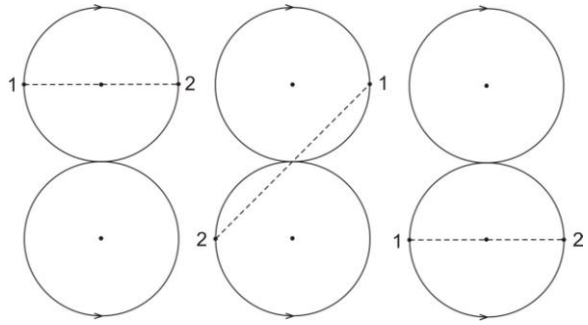

Figure 3. The scheme of electrons movement along the hydrogen molecule orbit in the form of an eight. They are represented as the three electrons positions being at the quarter of an orbit period from each other.

belong to the same wave, which at first was around atom but now is stationed in a different way (Figure 2).

The eight-form of the electron trajectories of hydrogen molecule is a principal link of the proposed model. Such closed construction is a simple and reliable mechanism which connects the two identical atoms in molecule. It is suitable for all atoms having only one electron on the external orbit. Such successful finding of nature (a peculiar molecular lock), apparently, is realized also in more complicated cases.

Note that, there are none of some intermediate stages between the states represented in Figures 1 and 2; otherwise, it is a typical quantum jump (analogous to the electron transition from the second energy level to the first one).

Every one of the hydrogen molecule halves in the given model is analogous to helium atom in some respects: each electron shell of the both molecular halves consists of the two shared electrons and is closed. These shells cannot overlap because this contradicts to Pauli principle. Consequently, they have the high strength and, practically, do not deform by collisions. It is clear that, the traditional interpretation of covalent bond is unacceptable for the proposed model.

Since electrons of our model move around nuclei on the same orbit (in the shape of an eight) with a constant speed, the average linear density of negative charge on the orbit is constant. If the orbit plane rotates uniformly around the axis AB, the electron cloud of molecule can be considered symmetric about AB. One can see that, the electron cloud of each half of hydrogen molecule is symmetric also about its equator plane; this means that, an interaction force of each nucleus with its electron cloud is equal zero.

Let us appeal to the simplest molecular construction - ion H_2^+. Electrostatic interaction of the electron clouds (shells) of its halves also is equal to zero; indeed, there is only one electron on the orbit, therefore there is nothing to interact with it. So, electrostatic interaction of the halves of this construction consists of a nuclei mutual

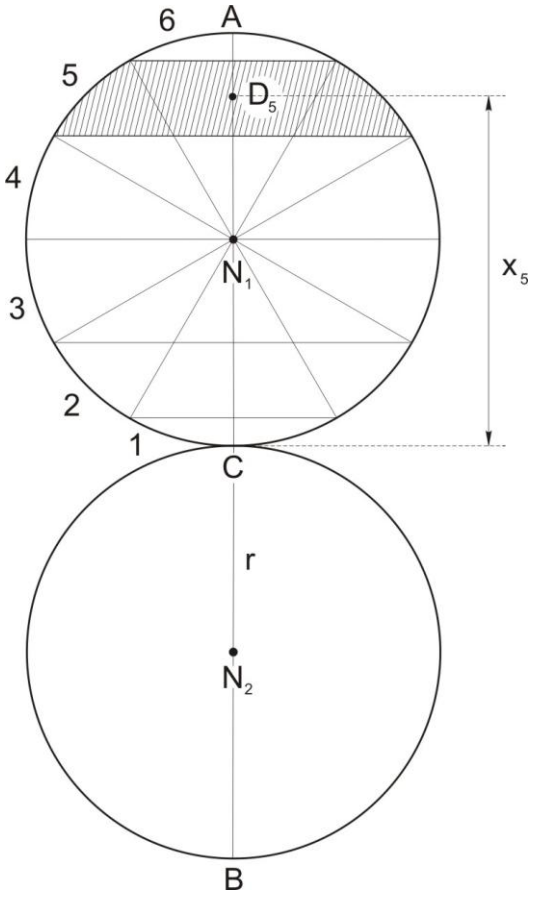

Figure 4. The scheme of an interaction of nucleus of ion H_2^+ with the electron shell of another nucleus (aspect from the side); the electron shell is divided in 6 latitude zones, numbers of which are pointed at the left side, the point D_5 is the centre of the fifth zone; x_5 is the distance from the centre C of ion to the point D_5.

repulsion with a force F_1 and an attraction of each nucleus to the electron shell of other half with a force F_2.

Let us produce the results of such calculation (in the conditional units). Each nucleus is repelled from other one with Coulomb force:

$$F_1 = \frac{e^2}{(2r)^2} = 0{,}25\frac{e^2}{r^2} = 0{,}25\ cond.un.$$

Here, *r* is the radius of sphere of the construction half.

The force F_2 can be calculated with the method of successive approaches; for this, it is a necessary preliminary to divide the spherical surface of the molecule half in several latitude rings of the same charge (Figure 4). Let us replace the charge of each latitude ring (zone) by equal point charge situated at the centre of this zone. The force of interaction of nucleus with this charge of one zone is:

$$F_{2k} = e \cdot \frac{e}{2n} \cdot \frac{1}{(r+x_k)^2},$$

where, x_k is the distance from the centre C of ion to the centre of the given zone. (The size of x_k can be measured on figure similar to Figure 4.) So:

$$F_2 = \frac{e^2}{r^2} \cdot \frac{1}{2n} \sum_{k=1}^{n} \frac{1}{\left(1+\frac{x_k}{r}\right)^2} = \frac{1}{2n} \sum_{k=1}^{n} \frac{1}{\left(1+\frac{x_k}{r}\right)^2}\ cond.un.$$

The calculation is fulfilled with four approaches by n = 3, 6, 12, and 24. The results are presented in Table 1.

It is clear that, successive approaches are quickly converged to the value which is approximately equals to 0.19 cond. un. To sum up we have: $F = F_1 - F_2 = 0.25 - 0.19 = 0.06$ cond. un. Thus, the halves of such construction are repelled from one other, that is, electrostatic interaction (in the given model) cannot explain the existence of ion H_2^+. Meantime, this ion exists, the energy of its chemical bond is equal 256 kJ/mol; so, it is a very strong compound. But if one supposes that the nuclei of neutral atoms (or of the hydrogen molecule halves) are mutually attracted, everything falls into place.

As one can see, electrons in the proposed model play "an administrative" role: they define on which minimal distance could bring together atomic nuclei. The source of interaction forces of atoms (or of the molecule parts) is in atomic nuclei. Emphasize, that just the imaginary experiment, where the notion of the electron trajectory in atom is considered quite reasonable and acceptable, has led to the hydrogen molecule model described above. However, it is the very case when the consequence of the hypothesis can be compared with the results of experiments (Feynman, 1965).

ON A POSSIBLE EXPERIMENTAL VERIFICATION

The energy of the π-meson at rest is equal about 150 MeV. As is known, π^0-mesons are got with the aid of the charged particles accelerator during the collisions of protons. A necessary minimal energy of the moving proton (by his collision with the motionless proton) is about 300 MeV. Note that, π-mesons are unstable particles. The lifetime of the real π^0-meson is about 10^{-16} sec; it breaks down into the two photons with the energy of which is about 75 MeV.

Each of these photons, travelling through the substance of the register apparatus (counter), generates the electron pair (electron plus positron). But positron cannot exist a long time in the substance; it annihilates by a collision with the first approaching electron. As a result, there are formed two photons, which again generate electron pairs (with the energy less than that at he preceding stage). And so on, till a photon energy

Table 1. The results of the four approaches.

n	3	6	12	24
F2	0.1860	0.1875	0.1885	0.1890

becomes less than 1 MeV (such photons cannot generate electron pairs). The appearance of electron pairs is surely registered with the counter; their tracks make it possible to restore the picture of the break-up. With the aid of analogy between nuclear and internuclear interactions, we come to the following scheme. The energy of the hypothetical resting x^0-mesons must be about (150 MeV)/10^5=1500 eV. The minimal energy of the moving proton must be 3000 eV. Let us consider that, x^0-meson (similarly to π^0-meson) is unstable and breaks down into the two photons with the energy 750 eV each. At this point, the process comes to its close since the energy is less than 1 MeV.

Imagine that, the energy of protons in the beam of proton-proton accelerator increases, and by 3000 eV suddenly photons with energy about 750 eV appear. (This energy corresponds to the wavelength 2.0×10^{-10} m, that is, we have Röntgen rays.) Hence, one may deduce that, the collisions of protons have led to the origin of x^0-mesons. So, the existence of x^0-mesons can be checked up experimentally. As this prediction is rather approximate, it would be able to carry out the search in the sufficiently broad range of the proton energy (for example, from 1000 to 9000 eV).

Emphasize, that analogy gives only the hint on a certain possible solution; it is necessary to have in mind the probability of existence of some other unknown mechanism.

Conclusion

One could ask: why the traditional version of covalent bond does not generate the doubts of researchers in spite of some its artificiality? Let us attempt to answer to it.

The doubts, apparently, take place; but they do not exceed a certain psychological barrier. Strange as this may seem, the principle of simplicity plays a part of such barrier: it turned out that, the covalent bond between atoms may be explained in the framework of well-known fundamental interaction, namely with electromagnetic forces. Of course, such understanding leads to some difficulties; physicists and chemists well know about this. But there had been no a special necessity to go out of the limits of the existing paradigm. This presented itself reasonable and logical.

The new approach to the problem came up from an unexpected side and somewhat by chance: to explain the forces between the molecules of the second liquid, we were forced to assume the existence of an internuclear interaction. This enabled to come up to the problem of the chemical covalent bond from a different angle.

REFERENCES

Bernal JD, Fowler RH (1933). A theory of water and ionic solution, with particular reference to hydrogen and hydroxyl ions. J. Chem, Phys. 1: 515.

Bluhm H, Ogletree DF, Fadley CS, Hussain Z and Salmeron MJ (2002). The premelting of ice studied with photoelectron spectroscopy. J. Phys. Condens. Matter 14:L227.

Dash JG, Fu H, Wettlaufer JS (1995). The premelting of ice and its environmental consequences. Rep. Prog. Phys. 58:115 and references therein.

Engemann S, Reichert H, Dosh H, Bilgram J, Honkimäki V, Snigirev A (2004). Interfacial melting of ice in contact with SiO_2. Phys. Rev. Lett. 92:205701.

Erdey-Grus T (1973). Grundlagen der Structur der Materie. Budapest, Chap. 5.

Feynman R (1965). The character of physical law. London, 1965. Lecture 7.

Heisenberg W (1927). Uber den anschaulichen Inhalt der quantentheoretischen Kinematik und Mechanik. Z. Phys. 43:172.

Mosienko BA (2008). Sublimation: a two-step phase transition. Z. Phys. Chem. 222:1533.

Mosienko BA (2009). Second liquid - an intermediate phase of sublimation. Z. Phys. Chem. 223:905.

Mosienko BA (2012). Nanoscale liquid is second liquid. In Vivek Patel (ed.) *Chemical kinetics*. Published by In Tech. Croatia, pp 309-322.

Reichert H, Klein O, Dosh H, Denk M, Honkimäki V, Lippmann T, Reiter G (2000). Observation of five-fold local simmetry in liquid lead. Nature (London) 408:839.

Turnbull D (1952). Kinetics of solidification of supercooled liquid mercury droplets J. Chem. Phys. 20:411.

academicJournals

Vol. 8(37), pp. 1830-1835, 9 October, 2013
DOI: 10.5897/IJPS2013.3968
ISSN 1992-1950 © 2013 Academic Journals
http://www.academicjournals.org/IJPS

International Journal of Physical Sciences

Full Length Research Paper

Determination of trace elements in nutrition materials in Kingdom of Saudi Arabia

Badriah Saad Al-Farhan

Department of Chemistry, Faculty of Girls for Science, King Khalid University, Abha, KSA, Saudi Arabia.

Accepted 26 September, 2013

Four types of edible tubercular roots cultivated in Saudi Arabia are analysed through sequential determination of certain essential and toxic trace elements by inductively coupled plasma atomic emission spectrometry (ICP-AES). Comparable runs carried out using both flame and graphite atomic absorption spectroscopy (AAS). Radish proved to contain the highest concentration level of iron (>21 µg/g), onion contains high concentration of zinc and strontium (~ 6 and 9 µg/g) and potato was found to contain the highest concentration level of copper (~2 µg/g). Samples of carrots, radish and potato collected from different locations are also analysed to study the effect of cultivation area on the concentration levels of trace elements in edible tubercular roots. Variation in the concentration levels of iron, zinc, copper, cobalt, strontium, cadmium and lead in each type of test samples seem not to be significant. Detailed studies seem necessary to throw further light on the effect of different of sample location on the concentration levels of both essential and toxic trace elements in different vegetable materials; especially those cultivated in areas neighboring various industrial and other human activities in Saudi Arabia.

Key words: Tubercular roots, trace elements, inductively coupled plasma atomic emission spectrometry (ICP-AES), atomic absorption spectroscopy (AAS) analysis.

INTRODUCTION

Human beings are encouraged to consume more food materials such as vegetables and fruits, which are good sources of vitamins and minerals beneficial to human health (Mohamed et al., 2005). Heavy metal contamination in agricultural environments can come from atmospheric fall-out, pesticide formulations, contamination by chemical fertilizer and irrigation with water of poor quality (Marcovecchio et al., 2007).

Trace elements in nutrition materials play significant role in human health. Trace concentration of iron, zinc, copper, manganese, nickel, cobalt, molybdenum, selenium, iodine, and fluorine are considered essential for human life (Clemente et al., 1977; Roberts, 1981). The absence or deficiency of one of these elements in certain body organs leads to physiological abnormalities in a number of biological processes which can be remedied by addition of limited quantities from the deficient element (Cotzias, 1970). Few other elements such as lead, cadmium, tin and mercury are highly toxic for both animal and human lives and may lead to death when ingested with high doses. The presence of different concentration levels of several trace elements (including those with toxic effects) in individual food articles and integrated human diets is mainly due to the uncontrolled release of various types of toxic pollutants in the different environmental compartment from increased industrial and other human activities (Underwood, 1971). It is therefore necessary to monitor the concentration level of toxic and essential elements in common food items for daily intake (Qureshi et al., 1990; Noel et al., 2011). In the present work, four edible tubercular roots including carrots, onion, potato, radish that are mostly consumed by a wide spectrum

E-mail: shahd_bb@hotmail.com

Table 1. Analysed vegetable tubercular roots.

Common name	Family	Botanic name
Carrots	Umbelliferae	*Daucus carota*
Potato	Solanacea	*Solanum tuberosum*
Onion	Amarylilaceae	*Allium cepa*
Radish	Cruciferae	*Raphanus sativum*

of the King of Saudi Arabia population have been analysed to comment on their suitability for human intake.

EXPERIMENTAL

Sampling and sample preparation

The test samples were collected from a number of agricultural areas. A list of test species is given in Table 1, with their botanical names and respective families. To investigate the effect of sample location on the concentration of trace elements in test items; carrots, radish, potato were collected from three areas. From the cultivated part of the southern region in Saudi Arabia, from the northern region, and from eastern region as shown in Figure 1. For sample preparation, collected samples were thoroughly washed and air dried at room temperature. After recording the wet weight, each species was oven- dried at 60°C for 72 h) (Zaidi et al., 1990) and the corresponding dry weight and moisture content determined. Representative dried samples were powdered by using a teflon ball mill, sieved to ≅200 mesh and finally stored in pre-cleaned polyethylene capped bottles. Nitric acid – hydrogen peroxide – perchloric acid mixture was used to digest different test samples.
For (2 to 10 g) of dried matter, the mixture used includes 20 ml of 14.4 mol l^{-1} nitric acid, 10 ml of 30% hydrogen peroxide and 10 ml of 9.9 mol l^{-1} perchloric acid. In addition, 18.0 mol l^{-1} sulphuric acid (for 10 g of dried matter, 2.0 ml of acid was added to prevent losses of metal halides by volatilization (Feinberg and Ducauze, 1980; Erwin and Ivo, 1992). Digestion normally took place in all glass containers under reflux at 170°C until a clear digest was obtained after approximately 3 h (Yaman and Gucer, 1995). The digest was centrifuged to separate the clear solution and the residue washed with bidistilled water and re-centrifuged to prevent any elemental losses. The first washing was added to the original solution before being diluted to known volume.

Instrumentation

(i) Inductively coupled plasma atomic emission spectrometry (ICP-AES) measurements were done with a compact tuned – oscillator coupled with high resolution Echelle grating spectrometer, minicomputer control services, peristaltic pump and an automated sample changer. The system includes a plasma spectrometer, type Leeman from USA, 2.5 KW generator, a three -turn copper load coil and a Hidebrand Grid nebulizer. The spectrometric system is of a fixed optics model with a PMT for sequential operation (type f18 Echelle), with a single pass prism / lens used for stray light reduction to cover a wavelength range from 190 to 800 nm.
(ii) The atomic absorption spectroscopy (AAS) measurements were carried out with AA spectrometer, model Z -8100 polarized Zeeman, manufactured by Hitachi, Ltd., from Japan Hitachi single – element hollow cathode lamps were used with air- acetylene flow rate ranging from 0.5 to 4.0 L/min with an auxiliary oxidant gas pressure ranging from 140 to 120 kpa. The instrument is provided with

Figure 1. Samples location

temperature regulation device and automated sampling by a built in auto sampler, type SSC -200. Selection of wavelength ranged from 190 to 900 nm.

Spectroscopic measurements

(i) ICP- measurements were done in sequential multi- element mode. An analytical programme was established both for calibration and routine analysis. The selected analytical wavelengths represent the characteristic lines which are almost free from spectral interference to eliminate any correction at the concentration levels of interest, these are:

(a) Iron - 259.94 (nm)
(b) Copper - 324.75
(c) Zinc - 213.86
(d) Cadmium - 214.44

Measurements were done in triplicates according to the following operating conditions:

(a) Forward r.f. power 1.00 KW (0.5A)
(b) Argon flow rate 12 L/min
(c) Nebulizer gas 0.3-0.5 L/min
(d) Sample uptake rate 1 L/min

(ii) AAS measurements were carried out under a constant air flow rate or (15.0 L/min), according to the following operational condition for each element as in Table 2.

Chemicals and reagents

All chemicals used were of A.R or extra pure grades. A set of standards were prepared from readily made standard solutions provided from Merck, AG, Darmstadt, Germany by dissolution in, or adequate dilution with dilute nitric acid solution. Bidistilled water in all glass apparatus was used for preparation of different solutions, used standards and for final glass ware washing. In the digestion procedure, concentrated nitric acid (65%, 14.4 mol l^{-1}), sulphuric acid (98%, 18 mol l^{-1}), hydrogen peroxide (30%) and perchloric acid (65%, 9.9 mol l^{-1}) were used.

Table 2. Operational conditions for AAS measurements.

Condition	Fe	Zn	Cu	Co	Sr	Cd	Pb
Wavelength, nm	248.3	213.9	324.8	240.7	460.7	228.8	283.3
Lamp current ,mA	15	7.5	7.5	15	10	7.5	10
Slit width	0.2	1.3	1.3	0.2	0.5	1.3	1.3
Acetylene flow rate,$Lmin^{-1}$	1.5	1.5	1.7	1.7	1.7	-----	-----
Heating program drying temp., °C	-----	-----	-----	-----	-----	80-120	80-120
Time/sec	-----	-----	-----	-----	-----	30	30
Ashing temp., °C	-----	-----	-----	-----	-----	300	400
Time/sec	-----	-----	-----	-----	-----	30	30
Atomization temp., °C	-----	-----	-----	-----	-----	1700	2100
Time/sec	-----	-----	-----	-----	-----	7	7
Cleaning temp., °C	-----	-----	-----	-----	-----	2600	3000
Time/sec	-----	-----	-----	-----	-----	30	30

Table 3. Concentration of trace elements in edible tubercular roots*).

Element	Carrots	Onion	Radish	Potato	Intake levels **)
a)Assessment of trace elements by ICP-AES (in µg/g wet weight)					
Iron	4.68±0.1	16.25±0.1	20.84±1.2	6.63±0.1	25-75 mg
Zinc	2.21±0.1	5.74±0.0	2.82±0.2	3.43±0.0	10-20 mg
Copper	1.51±0.2	1.42±0.2	0.31±0.02	1.66±0.05	--------
Cobalt	0.32±0.0	0.54±0.01	0.36±0.0	0.56±0.02	150-580 µg
Cadmium	0.17±0.01	0.34±0.02	0.25±0.01	0.41±0.01	--------
b)Assessment of trace elements by FAAS (in µg/g wet weight)					
Iron	4.79±1.2	16.18±0.4	21.26±0.5	5.82±0.7	25-75 mg
Zinc	2.68±0.2	5.63±0.1	2.67±0.1	3.45±0.2	10-20 mg
Copper	1.39±0.1	1.44±0.3	0.38±0.0	1.92±0.1	--------
Cobalt	0.30±0.0	0.50±0.0	0.38±0.1	0.57±0.02	150-580 µg
Strontium	3.37±0.0	9.19±0.1	4.94±0.05	3.66±0.05	42-1240 µg
c)Assessment of trace elements by GAAs (in µg/g wet weight)					
Cadmium	0.19±0.01	0.34±0.02	0.22±0.01	0.44±0.01	--------
Lead	0.55±0.0	0.68±0.01	0.31±0.04	0.67±0.01	54-500 µg

*) the results are mean of at least triplicate measurements; based on determination of each trace element in aliquot portions of sample solution containing known amounts of respective dried tuber, final concentration levels and the results based on wet weight are calculated from respective dry weight results.**) acceptable levels of daily intake concentration.

RESULTS AND DISCUSSION

Trace elements in tubers

The results in Table 3, show that iron, zinc, copper, cobalt, strontium, cadmium and lead proved to be present in different concentration levels in various types of tubercular roots. The examined species including carrots, onion, radish and potato are among the common vegetables for human nutrition in Saudi Arabia. The choice of these species aims to define the role of different soils, fertilizers and mode of irrigation as possible pathways for trace elements to man through the food chain (Husain et al., 1995; Ozores-Hampton et al., 1997; Millour et al., 2011). To get reliable and comparable results, the assessment of trace elemental concentrations in different samples is based on atomic spectroscopy using ICP-AES, flame and graphite AAS techniques. ICP-AES has the advantage of being rapid in providing analytical data for several elements in a single run. All used techniques proved to give comparable and reliable results. This is clearly illustrated by the results of iron,

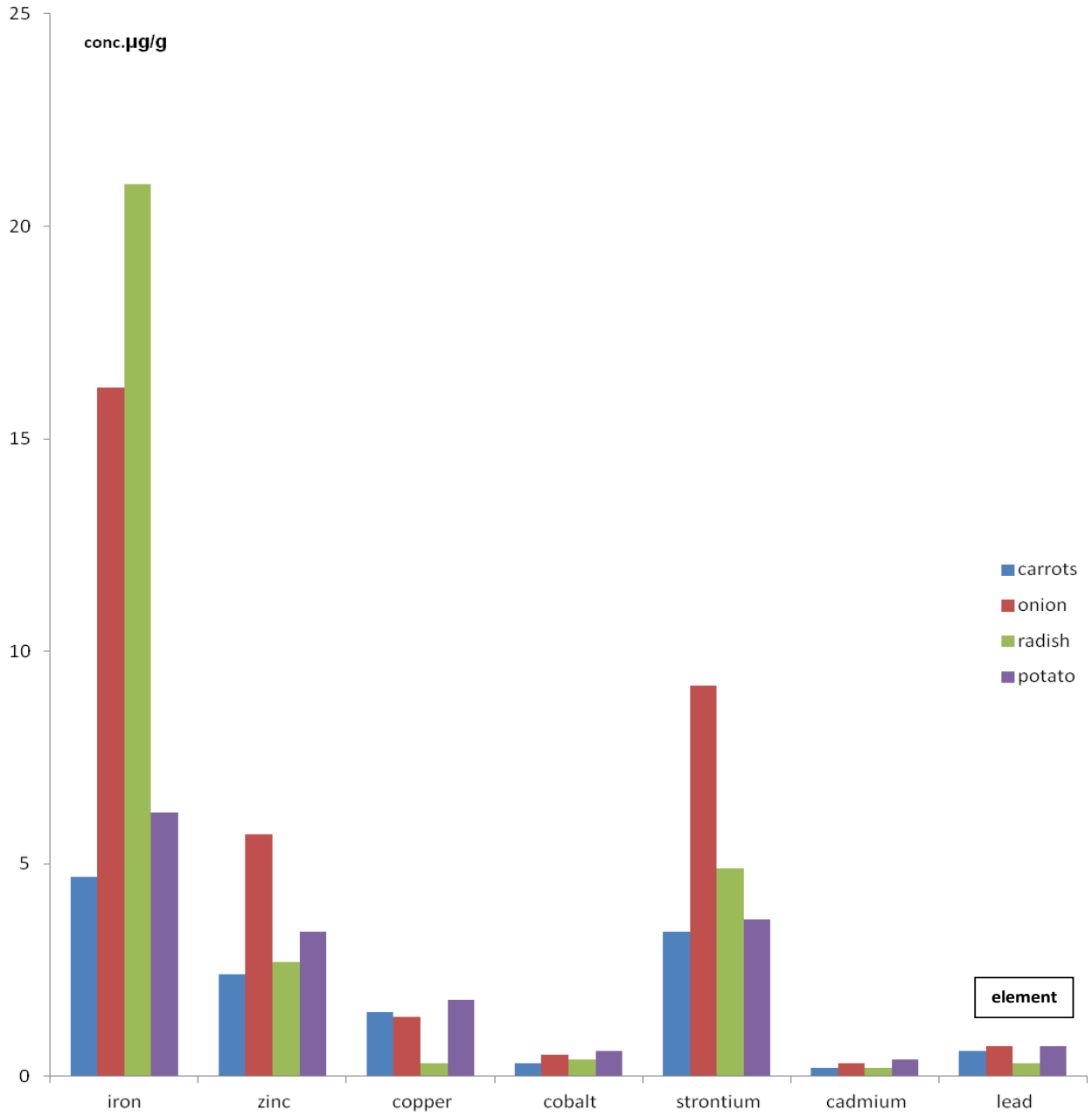

Figure 2. Concentration levels of Trace elements in test samples

zinc, copper, cobalt and cadmium in all types of tested species which proved to be subject to almost the same mean standard deviation for each analyte.

The results (expressed in terms of µg/g of wet weight) showed that radish contains the highest concentration levels of iron (21.26 µg/g), onion proved to contain the highest concentration of zinc (5.74 µg/g) and strontium (9.19 µg/g). Potato contains the highest levels of copper (1.92 µg/g). For toxic elements, it was found that potato contains the highest concentration levels of both cadmium and lead (0.44 and 0.67 µg/g), (Figure 2). The concentration levels of iron, zinc and copper are almost of the same order or even less than those previously reported by several workers (Finch and Monsen, 1974; Thomas et al., 1952). While the concentration of cobalt and strontium is several orders of magnitude higher than the values reported by other workers (Schroeder et al., 1967; Wikelsk et al., 1993).

In general, one assumes that changes in the concentration levels of trace elements in the examined species can be mainly attributed to changes in the chemical composition of water used for irrigation, the type

Table 4. Trace element concentrations in different carrot, radish and potato samples*).

Element	Sarat Ebeda	Alehssa	Algoff	Mean δ_n
		a) Carrots		
Iron	4.6±0.2	5.03±0.1	4.76±0.5	0.2
Zinc	2.33±0.1	3.13±0.1	2.6±0.5	0.2
Copper	0.78±0.1	1.03±0.1	0.806±0.1	0.0
Cobalt	0.28±0.2	0.33±0.1	0.30±0.2	0.05
Strontium	3.16±1.0	3.57±1.0	3.37±1.2	0.1
Cadmium	0.14±0.01	0.21±0.01	0.21±0.01	0.0
Lead	0.50±0.01	0.59±0.01	0.55±0.01	0.0
		b) Radish		
Iron	20.46±1.0	21.8±1.2	21.53±1.0	0.1
Zinc	2.26±0.1	2.90±0.2	2.86±0.1	0.05
Copper	0.33±0.1	0.33±0.05	0.47±0.1	0.02
Cobalt	0.35±0.1	0.42±0.2	0.38±0.1	0.05
Strontium	4.56±1.0	5.50±1.0	4.76±0.5	0.2
Cadmium	0.21±0.01	0.24±0.01	0.22±0.01	0.0
Lead	0.30±0.01	0.32±0.01	0.32±0.01	0.0
		c) Potato		
Iron	5.03±0.2	6.43±0.1	6.00±0.1	0.05
Zinc	2.93±0.1	4.26±0.1	3.16±0.2	0.05
Copper	1.56±0.5	2.36±0.1	1.83±0.2	0.2
Cobalt	0.51±0.1	0.63±0.1	0.58±0.2	0.05
Strontium	3.03±0.5	4.17±1.0	3.77±0.5	0.2
Cadmium	0.40±0.02	0.49±0.02	0.44±0.02	0.0
Lead	0.67±0.01	0.71±0.01	0.67±0.01	0.0

*) concentrations in µg/g, on wet weight basis.

of soil in various agricultural areas, and seasonal changes in ambient temperature.

Under comparable irrigation conditions, however, trace elemental concentrations may be affected by the sorptive capacity of different roots, the physical characteristics of the edible body in different species and the chemical composition of organic compounds in each type that might form different complexes with various metallic species. Thus, the increased concentration levels of cobalt, strontium than the mean values so far reported may be attributed to cultivation in areas rich with different minerals, especially when using water contaminated with industrial waste effluents, including trace concentrations of either or more of these elements. Never the less, the high concentration levels determined in all test samples, do not exceed the acceptable levels for daily intake. These are almost about 150 to 580 µg for cobalt, and 42 to 1240 µg for strontium. For iron, zinc and lead on the other hand, the concentration levels determined are far below those reported for daily intake lying within 25 to 75 mg for iron, 10 to 20 mg for zinc and 54 to 500 µg for lead (Dabeka et al., 1987; Galal-Gorchev, 1991).

Effect of sample location

To study the effect of sample location on the concentration levels of both essential and toxic trace elements in tubercular roots, carrots, radish and potato were collected as test samples from three different areas. These include an agricultural area near the industrial zone of the eastern region of Saudi Arabia (Alehssa), an agricultural area free from any industrial activities at the southern region of Saudi Arabia (Sarat Ebeda), and from the northern region of Saudi Arabia (Algoff). The essential trace elements investigated include iron, zinc, copper, cobalt and strontium, and the toxic elements are represented by cadmium and lead. This was specifically verified by successive triplicate analysis using not only ICP-AES but also, flame and graphite AAS measurements.

In Table 4, the concentration levels of iron, zinc, copper, cobalt, strontium, cadmium and lead in different

samples of carrots, radish and potatoes collected from the three above mentioned areas are presented. It is observed that iron has a mean concentration value of 4.78 µg/g in carrots with a highest concentration level of 5.03 µg/g in samples collected from Alehssa and a lowest concentration level of 4.6 µg/g in those from Sarat Ebeda. For radish and potato, iron proved to have a mean value of 21.26 and 5.82 µg/g respectively. For zinc, the same trend is followed, showing mean concentration levels 2.68, 2.67 and 3.45 µg/g, the highest values of 3.13, 2.90 and 4.26 µg/g for carrots, radish and potato, respectively. On the other hand, copper, cobalt, strontium, cadmium and lead also follow the same trend.

It was found that the concentration levels of the trace elements determined in carrots, radish and potato samples collected from the three different areas are almost of the same order. Samples collected from areas neighboring several industrial activities in (Alehssa) proved to contain slightly higher concentration levels of all the tested elements than those collected from (SaratEbada) and from (Algoff).

Conclusion

The results obtained show that radish contains the highest concentration level of iron, onion contains high concentrations and strontium and potato was found to contain the highest concentration levels of copper. The standard deviations in the results obtained for almost all determined elements are relatively low ranging from 1.5 for strontium determined by FAAS in onion to 0.0 in case of determination of several elements by the different used techniques indicating the reliability of ICP, flame and graphite AAS techniques for the determination of the concerned elements.

In the light of the obtained data, one may conclude that samples cultivated in areas far from industrial and other human activities tend to contain lower concentration levels of both essential and toxic elements than others. This can be noted in particular by considering the change in the concentration levels of the different elements determined in test samples collected from the agricultural area of Sarat Ebeda which seem to be lower than those collected from areas neighboring the industrial zone of Alehssa.

The difference in the concentration levels of all analysed trace elements collected from the different areas give a mean standard deviation not exceeding 0.2 with a percentage difference ≤10%, which lies within the experimental error in optical measurements especially when dealing with low concentration levels of different analytes. It is recommended from the present study that the work needs further investigation referring to soil types and irrigation water that affect on sample location results.

REFERENCES

Clemente GF, Cigna Rossi L, Santaroni GP (1977). Trace element intake and excretion in the italian population. J. Radioanal. Chem. 37:549-558.

Cotzias GC (1970). Trace subst. Environ. Health-Proc. University Mo. Annual Conference, 1 st ed, P. 5.

Dabeka RW, McKenzie AD, Lacroix GM.A (1987). Dietary intakes of lead, cadmium, arsenic and fluoride by Canadian adults: a 24-hour duplicate diet study. Food additives contaminants 4:89-101.

Erwin JM, Ivo N (1992). Determination of Lead in tissues: A pitfall due to wet digestion procedures in the presence of sulphuric acid. Analyst 23:117.

Feinberg M, Ducauze C (1980). High temperature dry ashing of foods. J. Anal. Chem. 52:207.

Finch CA, Monsen ER (1974). Iron nutrition and the fortification of food with iron. J. American Medical Association 219:1462.

Galal-Gorchev H (1991). Dietary intake of pesticide residues, cadmium, mercury and lead. Food additives and contaminants, 6:793-806.

Husain A, Baroon Z, Al-Ati T, Sawaya W (1995). Heavy metals in fruits and vegetables grown in Kuwait during the oil well fires. Arab Gulf J. Sci. Res. 3:535-542.

Marcovecchio JE, Botté SE, Freije RH (2007). Heavy metals, major metals, trace elements. In L.M. L. Nollet (Ed.), Handbook of water analysis (2 nd ed, pp. 270-311). Boca Raton: CRC Press.

Millour S, Noel L, Kadar Ali, Chekri R, Vastel C, Sirot V, Guerin T (2011). Pb, Hg, Cd, As, Sb and Al levels in foodstuffs from the 2nd French total diet study. J. food chem. 126:1787-1799.

Mohamed AE, Rashed MN, Mofty A (2005). Assessment of essential and toxic elements in some kinds of vegetables. J. Ecotoxi. Environ. Safety 55:251-260.

Noel L, Millour S, Kadar Ali, Chekri R, Vastel C, Guerin T (2011). Simultaneous of 21 elements in foodstuffs by ICP-MS after closed-vessel microwave digestion:Method validation. J. food chem. 24: 111-120.

Ozores-Hampton M, Hanlon E, Bryan H, Schaffer B (1997). Cadmium, copper, lead, nickel and zinc concentrations in tomato and squash grown in MSW compost-amended calcareous soil. Compost Sci. Utilization, 4:40-45.

Qureshi IH, Mannan A, Zaidi JH, Arif M, Khalid N (1990). A Comparative Determination of Heavy Metals in Moss Tissue by Atomic. Int. J. Anal. Chem., 38:565-577.

Roberts HR (1981). Food safety. Wiley, New York. Chapter 3, pp. 77.

Schroeder HA, Nason AP, Tipton IH (1967). Essential Trace Metals in Man: Cobalt. J. Chronic Diseases, 20:869.

Thomas B, Thompson A, Oyenuga VA, Armstrong RH (1952). dardization of Analytical Methodology for Feeds: Proc. Int. The ash constituents of some herbage plants at different stages of Workshop, Ottawa, ON. 12–14 Mar. 1979. Rep. IRDC-134e. Int. maturity. Emp. J. Exp. Agric. 20:10–22.

Underwood EJ (1971). Trace elements in human and animal nutrition. Academic Press, New York, USA, P. 545.

Wikelsk M, Gall B, Trillmich F (1993). Ontogenetic changes in food intake and digestion rate of the herbivorous marine iguana. J. Oecologia, 94:373-379.

Yaman M, Gucer S (1995). Determination of cadmium and lead in vegetables after activated carbon enrichment by atomic absorption spectrometry. Analyst 120:101-105.

Zaidi JH, Qureshi IH, Arif M, Fatima I (1990). Critical evaluation of a Trace elements. Intr. J. Anal Chem. 43:25.

academicJournals

Vol. 8(37), pp. 1836-1856, 9 October, 2013
DOI: 10.5897/IJPS11.1611
ISSN 1992 - 1950 © 2013 Academic Journals
http://www.academicjournals.org/IJPS

International Journal of Physical Sciences

Full Length Research Paper

Solitary wave solutions of fifth-order (1+1)-dimensional Caudrey-Dodd-Gibbon equation

M. Ali Akbar[1,2], Norhashidah Hj. Mohd. Ali[1], M. Usman[3], M. Shakeel[3], Yang Xiao-Jun[4] and Syed Tauseef Mohyud-Din[3]*

[1]School of Mathematical Sciences, University Sains Malaysia, Malaysia.
[2]Department of Applied Mathematics, University of Rajshahi, Bangladesh.
[3]Department of Mathematics, Faculty of Sciences, HITEC University, Taxila Cantt, Pakistan.
[4]College of Science, China University of Mining and Technology, Xuzhou, Jiangsu, 221008, China.

Accepted 26 September, 2013

The manuscript deals with the abundant travelling wave solutions of the Caudrey-Dodd-Gibbon (CDG) equation which have been obtained in a uniform way by using alternative (G'/G)–expansion method wherein the generalized Riccati equation is used. Moreover, a relatively new technique which is called (U'/U)-expansion is also used to find solitary wave solutions of CDG equation. The solutions obtained in this article may be imperative and significant for the explanation of some practical physical phenomena. Numerical results coupled with the graphical representation explicitly reveal the complete reliability and high efficiency of the proposed algorithms.

Key words: (G'/G)-expansion method, travelling wave solutions, (U'/U)-expansion method, Caudrey-Dodd-Gibbon (CDG) equation, nonlinear evolution equations.

INTRODUCTION

The rapid development of nonlinear sciences witnesses a wide range of reliable and efficient techniques which are of great help in tackling physical problems even of highly complex nature. After the observation of solitonary phenomena by John Scott Russell (Wazwaz, 2009) in 1834 and since the KdV equation was solved by Gardner et al. (1967) by the inverse scattering method, finding exact solutions of nonlinear evolution equations (NLEEs) has turned out to be one of the most exciting and particularly active areas of research. The appearance of solitary wave solutions in nature is quite common. Bell-shaped Sech-solutions and kink-shaped Tanh-solutions model wave phenomena in elastic media, plasmas, solid state physics, condensed matter physics, electrical circuits, optical fibers, chemical kinematics, fluids, bio-genetics etc. The travelling wave solutions of the KdV equation and the Boussinesq equation which describe water waves are well-known examples. Apart from their physical relevance, the closed-form solutions of NLEEs if available facilitate the numerical solvers in comparison, and aids in the stability analysis. In soliton theory, there are many methods and techniques to deal with the problem of solitary wave solutions for NLEEs, such as, Backlund transformation (Rogers and Shadwick, 1982), Hirota's bilinear transformation (Hirota, 1971), Variational Iteration (Mohyud-Din, 2008), homogeneous balance (Wang, 1996), Tanh-function (Malfliet, 1992), Jacobi elliptic function (Ali, 2011), F-expansion (Zhou et al., 2003),

*Corresponding author. E-mail: syedtauseefs@hotmail.com

Mathematical Subject Classification: 35K99, 35P05, 35P99.

Homotopy Analysis (Liao, 1992a, b), Homotopy Perturbation (Mohyud-Din, 2007), Adomian's Decomposition (Adomian, 1994), First Integration (Taghizadeh and Mirzazadeh, 2011), Exp-function (He and Wu, 2006; Abdou et al., 2007; Akbar and Ali, 2011b; Mohyud-Din et al., 2010; Naher et al., 2011b), and others (Abbasbandy, 2007a, b; Mohyud-Din et al., 2009, 2011a, b; Usman et al., 2011).

In the similar context, Wang et al. (2008) established a widely used direct and concise technique which is called the (G'/G)-expansion method for obtaining the exact travelling wave solutions of NLEEs, where $G(\xi)$ satisfies the second order linear ordinary differential equation (ODE) $G''+\lambda G'+\mu G=0$, where λ and μ are arbitrary constants. In the articles, Abazari (2010), Akbar and Ali (2011a), Bekir (2008), Liu et al. (2010), Naher et al. (2011a), Zayed (2009a), Zayed and Gepreel (2009), Zhang et al. (2008a, b), Zayed and Al-Joudi (2010), the (G'/G)-expansion method is applied to investigate solutions of nonlinear partial differential equations in mathematical physics. It is to be highlighted that Zhang et al. (2010) presented an improved (G'/G)-expansion method to seek more general travelling wave solutions. Zayed (2009b) presented a new approach of the (G'/G)-expansion method where $G(\xi)$ satisfies the Jacobi elliptic equation $[G'(\xi)]^2=e_2G^4(\xi)+e_1G^2(\xi)+e_0$, e_2,e_1,e_0 are arbitrary constants, and obtained new exact solutions. Zayed (2011) again presented an alternative approach of this method in which $G(\xi)$ satisfies the Riccati equation $G'(\xi)=A+BG^2(\xi)$, where A and B are arbitrary constants. Inspired and motivated by the ongoing research in this area, we investigate ample new travelling wave solutions of the CDG equation in a uniform way by making use of the alternative (G'/G)–expansion method wherein the generalized Riccati equation is functioned. Moreover, we have also applied a relatively new technique namely (U`/U)-expansion Method to tackle the CDG equation. Numerical results coupled with the graphical representations explicitly reveal the complete reliability and high efficiency of the proposed algorithms.

METHODOLOGY

Suppose the general nonlinear partial differential equation

$$F(u,u_t,u_x,u_{tt},u_{tx},u_{xx},\cdots)=0 \tag{1}$$

where $u=u(x,t)$ is an unknown function, F is a polynomial in $u(x,t)$ and its partial derivatives in which the highest order partial derivatives and the nonlinear terms are involved. The main steps of the alternative (G'/G)-expansion method combined with the generalized Riccati equation are as follows:

Step 1: The travelling wave variable

$$u(x,t)=u(\xi),\ \xi=x-Vt \tag{2}$$

where V is the speed of the travelling wave, and permits us to transform the Equation (1) into an ODE:

$$Q(u,u',u'',\cdots)=0 \tag{3}$$

where the superscripts stands for the ordinary derivatives with respect to ξ.

Step 2: If Equation (3) is integrable, integrate term by term one or more times, yields constant(s) of integration.

Alternative (*G*`/*G*)-expansion method with generalized Riccati equation

Step 3: Suppose the traveling wave solution of Equation (3) can be expressed by a polynomial in (G'/G) as follows:

$$u(\xi)=\sum_{n=0}^{m}a_n\left(\frac{G'}{G}\right)^n,\quad a_m\neq 0 \tag{4}$$

where $G=G(\xi)$ satisfies the generalized Riccati equation,

$$G'=r+pG+qG^2, \tag{5}$$

where a_n $(n=0,1,2,\cdots,m)$, r, p and q are arbitrary constants to be determined later.

The generalized Riccati Equation (5) has the following twenty seven solutions (Zhu, 2008).

Family 1: When $p^2-4qr<0$ and $pq\neq 0$ (or $rq\neq 0$), the solutions of Equation (5) are:

$$G_1=\frac{1}{2q}\left[-p+\sqrt{4qr-p^2}\tan\left(\frac{1}{2}\sqrt{4qr-p^2}\xi\right)\right],$$

$$G_2=-\frac{1}{2q}\left[p+\sqrt{4qr-p^2}\cot\left(\frac{1}{2}\sqrt{4qr-p^2}\xi\right)\right],$$

$$G_3=\frac{1}{2q}\left[-p+\sqrt{4qr-p^2}\left(\tan\left(\sqrt{4qr-p^2}\xi\right)\pm\sec\left(\sqrt{4qr-p^2}\xi\right)\right)\right],$$

$$G_4 = -\frac{1}{2q}\left[p + \sqrt{4qr - p^2}\left(\cot\left(\sqrt{4qr - p^2}\xi\right) \pm \csc\left(\sqrt{4qr - p^2}\xi\right)\right)\right],$$

$$G_5 = \frac{1}{4q}\left[-2p + \sqrt{4qr - p^2}\left(\tan\left(\frac{1}{4}\sqrt{4qr - p^2}\xi\right) - \cot\left(\frac{1}{4}\sqrt{4qr - p^2}\xi\right)\right)\right],$$

$$G_6 = \frac{1}{2q}\left[-p + \frac{\sqrt{(A^2 - B^2)(4qr - p^2)} - A\sqrt{4qr - p^2}\cos\left(\sqrt{4qr - p^2}\xi\right)}{A\sin\left(\sqrt{4qr - p^2}\xi\right) + B}\right],$$

$$G_7 = \frac{1}{2q}\left[-p + \frac{\sqrt{(A^2 - B^2)(4qr - p^2)} + A\sqrt{4qr - p^2}\cos\left(\sqrt{4qr - p^2}\xi\right)}{A\sin\left(\sqrt{4qr - p^2}\xi\right) + B}\right],$$

where A and B are two non-zero real constants and satisfies the condition $A^2 - B^2 > 0$.

$$G_8 = \frac{-2r\cos\left(\frac{1}{2}\sqrt{4qr - p^2}\xi\right)}{\sqrt{4qr - p^2}\sin\left(\frac{1}{2}\sqrt{4qr - p^2}\xi\right) + p\cos\left(\frac{1}{2}\sqrt{4qr - p^2}\xi\right)},$$

$$G_9 = \frac{2r\sin\left(\frac{1}{2}\sqrt{4qr - p^2}\xi\right)}{-p\sin\left(\frac{1}{2}\sqrt{4qr - p^2}\xi\right) + \sqrt{(4qr - p^2)}\cos\left(\frac{1}{2}\sqrt{4qr - p^2}\xi\right)},$$

$$G_{10} = \frac{-2r\cos\left(\sqrt{4qr - p^2}\xi\right)}{\sqrt{(4qr - p^2)}\sin\left(\sqrt{4qr - p^2}\xi\right) + p\cos\left(\sqrt{4qr - p^2}\xi\right) \pm \sqrt{(4qr - p^2)}},$$

$$G_{11} = \frac{2r\sin\left(\sqrt{4qr - p^2}\xi\right)}{-p\sin\left(\sqrt{4qr - p^2}\xi\right) + \sqrt{(4qr - p^2)}\cos\left(\sqrt{4qr - p^2}\xi\right) \pm \sqrt{(4qr - p^2)}},$$

$$G_{12} = \frac{4r\sin\left(\frac{1}{4}\sqrt{4qr - p^2}\xi\right)\cos\left(\frac{1}{4}\sqrt{4qr - p^2}\xi\right)}{-2p\sin\left(\frac{1}{4}\sqrt{4qr - p^2}\xi\right)\cos\left(\frac{1}{4}\sqrt{4qr - p^2}\xi\right) + 2\sqrt{(4qr - p^2)}\cos^2\left(\frac{1}{4}\sqrt{4qr - p^2}\xi\right) - \sqrt{(4qr - p^2)}}.$$

Family 2: When $p^2 - 4qr > 0$ and $pq \neq 0$ (or $rq \neq 0$), the solutions of Equation (5) are:

$$G_{13} = -\frac{1}{2q}\left[p + \sqrt{p^2 - 4qr}\tanh\left(\frac{1}{2}\sqrt{p^2 - 4qr}\xi\right)\right],$$

$$G_{14}=-\frac{1}{2q}\left[p+\sqrt{p^2-4qr}\coth\left(\frac{1}{2}\sqrt{p^2-4qr}\xi\right)\right],$$

$$G_{15}=-\frac{1}{2q}\left[p+\sqrt{p^2-4qr}\left(\tanh\left(\sqrt{p^2-4qr}\xi\right)\pm i\sec h\left(\sqrt{p^2-4qr}\xi\right)\right)\right],$$

$$G_{16}=-\frac{1}{2q}\left[p+\sqrt{p^2-4qr}\left(\coth\left(\sqrt{p^2-4qr}\xi\right)\pm \csc h\left(\sqrt{p^2-4qr}\xi\right)\right)\right],$$

$$G_{17}=-\frac{1}{4q}\left[2p+\sqrt{p^2-4qr}\left(\tanh\left(\frac{1}{4}\sqrt{p^2-4qr}\xi\right)+\coth\left(\frac{1}{4}\sqrt{p^2-4qr}\xi\right)\right)\right],$$

$$G_{18}=\frac{1}{2q}\left[-p+\frac{\sqrt{(A^2+B^2)(p^2-4qr)}-A\sqrt{p^2-4qr}\cosh\left(\sqrt{p^2-4qr}\xi\right)}{A\sinh\left(\sqrt{p^2-4qr}\xi\right)+B}\right],$$

$$G_{19}=\frac{1}{2q}\left[-p-\frac{\sqrt{(B^2-A^2)(p^2-4qr)}+A\sqrt{p^2-4qr}\cosh\left(\sqrt{p^2-4qr}\xi\right)}{A\sinh\left(\sqrt{p^2-4qr}\xi\right)+B}\right],$$

where A and B are two non-zero real constants and satisfies the condition $B^2-A^2>0$.

$$G_{20}=\frac{2r\cosh\left(\frac{1}{2}\sqrt{p^2-4qr}\xi\right)}{\sqrt{p^2-4qr}\sinh\left(\frac{1}{2}\sqrt{p^2-4qr}\xi\right)-p\cosh\left(\frac{1}{2}\sqrt{p^2-4qr}\xi\right)},$$

$$G_{21}=\frac{2r\sinh\left(\frac{1}{2}\sqrt{p^2-4qr}\xi\right)}{\sqrt{p^2-4qr}\cosh\left(\frac{1}{2}\sqrt{p^2-4qr}\xi\right)-p\sinh\left(\frac{1}{2}\sqrt{p^2-4qr}\xi\right)},$$

$$G_{22}=\frac{2r\cosh\left(\sqrt{p^2-4qr}\xi\right)}{\sqrt{p^2-4qr}\sinh\left(\sqrt{p^2-4qr}\xi\right)-p\cosh\left(\sqrt{p^2-4qr}\xi\right)\pm i\sqrt{p^2-4qr}},$$

$$G_{23}=\frac{2r\sinh\left(\sqrt{p^2-4qr}\xi\right)}{-p\sinh\left(\sqrt{p^2-4qr}\xi\right)+\sqrt{p^2-4qr}\cosh\left(\sqrt{p^2-4qr}\xi\right)\pm\sqrt{p^2-4qr}},$$

$$G_{24}=\frac{4r\sinh\left(\frac{1}{4}\sqrt{p^2-4qr}\xi\right)\cosh\left(\frac{1}{4}\sqrt{p^2-4qr}\xi\right)}{-2p\sinh\left(\frac{1}{4}\sqrt{p^2-4qr}\xi\right)\cosh\left(\frac{1}{4}\sqrt{p^2-4qr}\xi\right)+2\sqrt{p^2-4qr}\cosh^2\left(\frac{1}{4}\sqrt{p^2-4qr}\xi\right)-\sqrt{p^2-4qr}}.$$

Family 3: When $r=0$ and $pq\neq 0$, the solutions of Equation (5) are:

$$G_{25}=\frac{-pd}{q\left[d+\cosh(p\xi)-\sinh(p\xi)\right]},$$

$$G_{26}=-\frac{p\left[\cosh(p\xi)+\sinh(p\xi)\right]}{q\left[d+\cosh(p\xi)+\sinh(p\xi)\right]},$$

where d is an arbitrary constant.

Family 4: When $q\neq 0$ and $r=p=0$, the solution of Equation (5) is:

$$G_{27}=-\frac{1}{q\xi+c_1},$$

where c_1 is an arbitrary constant.

Step 4: To determine the positive integer m, substitute solution Equation (4) along with Equation (5) into Equation (3) and then consider homogeneous balance between the highest order derivatives and the nonlinear terms appearing in Equation (3).

Step 5: Substituting Equation (4) together with Equation (5) into Equation (3) together with the value of m obtained in step 3, we obtain polynomials in G^i and $G^{-i}\ (i=0,1,2,3\cdots)$ and vanishing each coefficient of the resulted polynomial to zero, yields a set of algebraic equations for a_n p, q, r and V.

Step 6: Suppose the value of the constants a_n p, q, r and V can be obtained by solving the set of algebraic equations obtained in step 5. Since the general solutions of Equation (5) are known for us, substituting, a_n p, q, r and V together with the general solution of Equation (5) into Equation (4), we obtain new exact traveling wave solutions of the nonlinear evolution Equation (1).

New approach of (*G*`/*G*)-expansion method

Step 3: According to new approach of (*G*`/*G*)-expansion method, we assume that the wave solution can be expressed in the following form

$$u(\xi)=a_0+\sum_{n=1}^{M}a_n\left(\frac{G(\xi)}{G(\xi)}\right)^M, \tag{6}$$

where $G(\xi)$ is the solution of first order nonlinear equation in the form

$$G(\xi)G''(\xi)-\delta_1 G^2(\xi)+\delta_2(G'(\xi))^2=0, \tag{7}$$

$$\left(\frac{G(\xi)'}{G(\xi)}\right)'=\delta_1-\delta_2\left(\frac{G(\xi)'}{G(\xi)}\right)^2-\left(\frac{G(\xi)'}{G(\xi)}\right)^2,$$

$$\left(\frac{G(\xi)'}{G(\xi)}\right)''=-2\delta_2\delta_1\left(\frac{G(\xi)'}{G(\xi)}\right)'+2\delta_2^2\left(\frac{G(\xi)'}{G(\xi)}\right)^3+4\delta_2\left(\frac{G(\xi)'}{G(\xi)}\right)^3-2\delta_1\left(\frac{G(\xi)'}{G(\xi)}\right)+2\left(\frac{G(\xi)'}{G(\xi)}\right)^3,$$

where δ_1 and δ_2 are real constants. The Riccati Equation (5) plays important role in manipulating nonlinear equations to get exact solutions by the (*G*′/*G*)-expansion method. It has the following type of exact solutions.

Family 1: When $\delta_1,\delta_2\neq 0$,

$$\left(\frac{G'(\xi)}{G(\xi)}\right)=\frac{\left[\cosh\left(2\sqrt{\delta_2(1+\delta_2)}\xi\right)+\sinh\left(2\sqrt{\delta_2(1+\delta_2)}\xi\right)\right]\sqrt{\delta_2}+\sqrt{\delta_2}}{\left[\cosh\left(2\sqrt{\delta_2(1+\delta_2)}\xi\right)+\sinh\left(2\sqrt{\delta_2(1+\delta_2)}\xi\right)\right]\sqrt{1+\delta_2}-\sqrt{1+\delta_2}}.$$

Family 2: When $\delta_1<0$, and $(1+\delta_2)>0$, or $\delta_1>0$, and $(1+\delta_2)<0$

$$\left(\frac{G'(\xi)}{G(\xi)}\right)=\frac{\left[\cos\left(2\sqrt{-\delta_2(1+\delta_2)}\xi\right)-\sin\left(2\sqrt{-\delta_2(1+\delta_2)}\xi\right)\right]\sqrt{-\delta_2}+\sqrt{-\delta_2}}{\left[\cos\left(2\sqrt{-\delta_2(1+\delta_2)}\xi\right)+\sin\left(2\sqrt{-\delta_2(1+\delta_2)}\xi\right)\right]\sqrt{1+\delta_2}-\sqrt{1+\delta_2}}.$$

Family 3: When $\delta_1\neq 0$, and $\delta_2=0$,

$$\left(\frac{G'(\xi)}{G(\xi)}\right)=\frac{\left[\cosh\left(2\sqrt{\delta_2}\xi\right)+\sinh\left(2\sqrt{\delta_2}\xi\right)\right]\sqrt{\delta_2}+\sqrt{\delta_2}}{\left[\cosh\left(2\sqrt{\delta_2}\xi\right)+\sinh\left(2\sqrt{\delta_2}\xi\right)\right]-1}.$$

Family 4: When $\delta_1=0$, and $\delta_2\neq 0$,

$$\left(\frac{G'(\xi)}{G(\xi)}\right)=\frac{1}{1+\xi}\frac{1}{1+\delta_2}.$$

Family 5: When $\delta_1 = 0$, and $\delta_2 = 0$.

$$\left(\frac{G'(\xi)}{G(\xi)}\right) = \frac{1}{1+\xi}.$$

Step 4: Determine M. This, usually, can be accomplished by balancing the linear term(s) of highest order with the highest order nonlinear term(s) in Equation (4).

Step 5: Substituting Equation (6) into Equation (4) with (7) will yields an algebraic equation involving power of (*G′*/*G*). Equating the coefficients of like power of (*G′*/*G*) to zero gives a system of algebraic equations for a_i, k, l, m and ω. Then, we solve the system with the aid of a computer algebra system (CAS), such as MAPLE 13, to determine these constants.

Step 6: Putting these constant into Equation (6), coupled with the well known solutions of Equation (7), we can obtained the more general type and new exact travelling wave solution of the nonlinear partial differential Equation (1).

(*U*`/*U*)-expansion method

Step 3: According to (*U*`/*U*)-expansion method, we assume that the wave solution can be expressed in the following form

$$u(\xi) = \sum_{n=0}^{M} a_n \left(\frac{U^{\alpha}}{U}\right)^n, \quad (8)$$

where U is the solution of first order nonlinear equation in the form

$$U' = AU + B, \quad (9)$$

where A and B are real constants, M is a positive integer to be determined and the Equation (9) has solution

$$\frac{U'(\xi)}{U(\xi)} = \left(\frac{Ac\exp[A\xi]}{-\frac{B}{A}+c\exp[A\xi]}\right).$$

Step 4: Determine M. This, usually, can be accomplished by balancing the linear term(s) of highest order with the highest order nonlinear term(s) in Equation (4).

Step 5: Substituting (9) into ODE with (8) yields an algebraic equation involving power of *U*. Equating the coefficients of like power of *U* to zero gives a system of algebraic equations for a_i, k, l, m and ω. Then, we solve the system with the aid of a computer algebra system (CAS), such as MAPLE 13, to determine these constants.

Step 6: Putting these constant into Equation (8), coupled with the well known solutions of Equation (9), we obtained the more general type and new exact travelling wave solution of the nonlinear partial differential Equation (1).

New travelling wave solutions of Cuadrey-Dodd-Gibbon (CDG) equation

Here, the alternative (G'/G)-expansion method together with the generalized Riccati equation is employed to construct some new travelling wave solutions for the (1+1)-dimensional Cuadrey-Dodd-Gibbon (CDG) equation which is a very important nonlinear evolution equation in mathematical physics and engineering and have been paid attention by many researchers. Some exact solutions of the CDG equation are found in the literature. In general, the solutions of the CDG equation have been obtained by means of an Ansatz method. Included in the methods are the sin-cosine method and the rational Exp-function method (Abdollahzadeh et al., 2010), the Hirota's bilinear transformation method (Jiang and Bi, 2010), the Exp-function method (Xu, 2008), the variational iteration method (Jin, 2010), the multi-wave method (Shi et al., 2010), and the variable separation method (Zheng, 2010). In this paper, we apply the alternative (G'/G)-expansion method together with generalized Riccati equation for searching its solitary wave solutions. Let us consider the CDG equation:

$$u_t + u_{xxxxx} + 30uu_{xxx} + 30u_x u_{xx} + 180u^2 u_x = 0 \quad (10)$$

NUMERICAL RESULTS AND DISCUSSION

Alternative (*G*`/*G*)-expansion method using generalized Riccati equation

Now, we use the wave transformation equation into Equation (10), which yield:

$$-V u' + u^{(5)} + 30u u''' + 30u'u'' + 180u^2 u' = 0, \quad (11)$$

where $u^{(5)}$ denotes the fifth derivative of u with respect to ξ. Equation (11) is integrable, therefore, integrating we obtain

$$C - V u + u^{(4)} + 30u u'' + 60u^3 = 0 \quad (12)$$

According to step 3, the solution of Equation (12) can be expressed by a polynomial in (G'/G) as follows:

$$u(\xi) = a_0 + a_1\left(\frac{G'}{G}\right) + a_2\left(\frac{G'}{G}\right)^2 + \cdots + a_m\left(\frac{G'}{G}\right)^m, \ a_m \neq 0 \quad (13)$$

where $a_n, (n = 0,1,2,\cdots,m)$ are constants to be determined and $G = G(\xi)$ satisfies the generalized Riccati Equation (10). Considering the homogeneous balance between the highest order derivative and the nonlinear terms in Equation (12), we obtain $m = 2$.

Therefore, the solution Equation (13) takes the form,

$$u(\xi) = a_0 + a_1\left(\frac{G'}{G}\right) + a_2\left(\frac{G'}{G}\right)^2, \ a_2 \neq 0 \quad (14)$$

Using Equation (5), Equation (14) can be rewritten as,

$$u(\xi) = a_0 + a_1(p + rG^{-1} + qG) + a_2(p + rG^{-1} + qG)^2 \quad (15)$$

Substituting Equation (15) into (12), the left hand side is converted into polynomials in G^i and $G^{-i},(i=0,1,2,3,\cdots)$. Setting each coefficient of these resulted polynomials to zero, we obtain a set of simultaneous algebraic equations (we will omit to display them for simplicity) for a_0, a_1, a_2, p, q, r and V.

Solving the over-determined set of algebraic equations by using the symbolic computation software, such as Maple, we obtain

$$C=\frac{p^6}{9}-\frac{4}{3}p^4rq+\frac{16}{3}p^2q^2r^2-\frac{64}{9}q^3r^3,\ V=p^4-8p^2q\mathrm{r}+16q^2r^2,\ a_2=-1,\ a_1=p,\ a_0=-\frac{p^2}{6}+\frac{2}{3}qr, \tag{16}$$

where p, q and r are arbitrary constants.

Now on the basis of the solutions of Equation (5), we obtain the following families of solutions of Equation (10).

Family 1: When $p^2-4qr<0$ and $pq\neq 0$ (or $rq\neq 0$), the periodic form solutions of Equation (10) are,

$$u_1=-\frac{p^2}{6}+\frac{2}{3}qr+p\left(\frac{2\Delta^2\sec^2(\Delta\xi)}{-p+2\Delta\tan(\Delta\xi)}\right)-\left(\frac{2\Delta^2\sec^2(\Delta\xi)}{-p+2\Delta\tan(\Delta\xi)}\right)^2,$$

where $\Delta=\frac{1}{2}\sqrt{4qr-p^2}$, $\xi=x-(p^4-8p^2q\mathrm{r}+16q^2r^2)t$ and p, q, r are arbitrary constants.

$$u_2=-\frac{p^2}{6}+\frac{2}{3}qr-p\left(\frac{2\Delta^2\csc^2(\Delta\xi)}{p+2\Delta\cot(\Delta\xi)}\right)-\left(\frac{2\Delta^2\csc^2(\Delta\xi)}{p+2\Delta\cot(\Delta\xi)}\right)^2,$$

$$u_3=-\frac{p^2}{6}+\frac{2}{3}qr+p\left(\frac{4\Delta^2\sec(2\Delta\xi)(1\pm\sin(2\Delta\xi))}{-p\cos(2\Delta\xi)+2\Delta\sin(2\Delta\xi)\pm 2\Delta}\right)-\left(\frac{4\Delta^2\sec(2\Delta\xi)(1\pm\sin(2\Delta\xi))}{-p\cos(2\Delta\xi)+2\Delta\sin(2\Delta\xi)\pm 2\Delta}\right)^2,$$

$$u_4=-\frac{p^2}{6}+\frac{2}{3}qr-p\left(\frac{4\Delta^2\csc(2\Delta\xi)(1\pm\cos(2\Delta\xi))}{p\sin(2\Delta\xi)+2\Delta\cos(2\Delta\xi)\pm 2\Delta}\right)-\left(\frac{4\Delta^2\csc(2\Delta\xi)(1\pm\cos(2\Delta\xi))}{p\sin(2\Delta\xi)+2\Delta\cos(2\Delta\xi)\pm 2\Delta}\right)^2,$$

$$u_5=-\frac{p^2}{6}+\frac{2}{3}qr-p\left(\frac{2\Delta^2\csc(\Delta\xi)}{p\sin(\Delta\xi)+2\Delta\cos(\Delta\xi)}\right)-\left(\frac{2\Delta^2\csc(\Delta\xi)}{p\sin(\Delta\xi)+2\Delta\cos(\Delta\xi)}\right)^2,$$

$$u_6=-p\left(\frac{4A\Delta^2\left\{\sqrt{A^2-B^2}\cos(2\Delta\xi)-B\sin(2\Delta\xi)-A\right\}\left\{A\sin(2\Delta\xi)+B\right\}}{\left\{A^2\cos^2(2\Delta\xi)-A^2-B^2-2AB\sin(2\Delta\xi)\right\}\left\{pA\sin(2\Delta\xi)+2A\Delta\cos(2\Delta\xi)+pB-2\Delta\sqrt{A^2-B^2}\right\}}\right)$$
$$-\left(\frac{4A\Delta^2\left\{\sqrt{A^2-B^2}\cos(2\Delta\xi)-B\sin(2\Delta\xi)-A\right\}\left\{A\sin(2\Delta\xi)+B\right\}}{\left\{A^2\cos^2(2\Delta\xi)-A^2-B^2-2AB\sin(2\Delta\xi)\right\}\left\{pA\sin(2\Delta\xi)+2A\Delta\cos(2\Delta\xi)+pB-2\Delta\sqrt{A^2-B^2}\right\}}\right)^2$$
$$-\frac{p^2}{6}+\frac{2}{3}qr,$$

$$u_7=-p\left(\frac{4A\Delta^2\left\{\sqrt{A^2-B^2}\cos(2\Delta\xi)+B\sin(2\Delta\xi)+A\right\}\left\{A\sin(2\Delta\xi)+B\right\}}{\left\{A^2\cos^2(2\Delta\xi)-A^2-B^2-2AB\sin(2\Delta\xi)\right\}\left\{pA\sin(2\Delta\xi)-2A\Delta\cos(2\Delta\xi)+pB-2\Delta\sqrt{A^2-B^2}\right\}}\right)$$
$$-\left(\frac{4A\Delta^2\left\{\sqrt{A^2-B^2}\cos(2\Delta\xi)+B\sin(2\Delta\xi)+A\right\}\left\{A\sin(2\Delta\xi)+B\right\}}{\left\{A^2\cos^2(2\Delta\xi)-A^2-B^2-2AB\sin(2\Delta\xi)\right\}\left\{pA\sin(2\Delta\xi)-2A\Delta\cos(2\Delta\xi)+pB-2\Delta\sqrt{A^2-B^2}\right\}}\right)^2$$
$$-\frac{p^2}{6}+\frac{2}{3}qr,$$

where A and B are two non-zero real constants satisfies the condition $A^2 - B^2 > 0$.

$$u_8 = -\frac{p^2}{6} + \frac{2}{3}qr - p\left(\frac{2\Delta^2 \sec(\Delta\xi)\{p\cos(\Delta\xi) + 2\Delta\sin(\Delta\xi)\}}{2(p^2 - 2rq)\cos^2(\Delta\xi) + 4\Delta\, p\sin(\Delta\xi)\cos(\Delta\xi) + 4\Delta^2}\right)$$
$$-\left(\frac{2\Delta^2 \sec(\Delta\xi)\{p\cos(\Delta\xi) + 2\Delta\sin(\Delta\xi)\}}{2(p^2 - 2rq)\cos^2(\Delta\xi) + 4\Delta\, p\sin(\Delta\xi)\cos(\Delta\xi) + 4\Delta^2}\right)^2,$$

$$u_9 = -\frac{p^2}{6} + \frac{2}{3}qr + p\left(\frac{2\Delta^2 \csc(\Delta\xi)\{p\sin(\Delta\xi) - 2\Delta\cos(\Delta\xi)\}}{2(p^2 - 2rq)\cos^2(\Delta\xi) + 4\Delta\, p\sin(\Delta\xi)\cos(\Delta\xi) - p^2}\right)$$
$$-\left(\frac{2\Delta^2 \csc(\Delta\xi)\{p\sin(\Delta\xi) - 2\Delta\cos(\Delta\xi)\}}{2(p^2 - 2rq)\cos^2(\Delta\xi) + 4\Delta\, p\sin(\Delta\xi)\cos(\Delta\xi) - p^2}\right)^2,$$

$$u_{10} = -\frac{p^2}{6} + \frac{2}{3}qr - p\left(\frac{2\Delta^2 \sec(2\Delta\xi)\{1 \pm \sin(2\Delta\xi)\}\{p\cos(2\Delta\xi) + 2\Delta\sin(2\Delta\xi) \pm 2\Delta\}}{(p^2 - 2rq)\cos^2(2\Delta\xi) + 2\Delta\{1 \pm \sin(2\Delta\xi)\}\{2\Delta \pm p\cos(2\Delta\xi)\}}\right)$$
$$-\left(\frac{2\Delta^2 \sec(2\Delta\xi)\{1 \pm \sin(2\Delta\xi)\}\{p\cos(2\Delta\xi) + 2\Delta\sin(2\Delta\xi) \pm 2\Delta\}}{(p^2 - 2rq)\cos^2(2\Delta\xi) + 2\Delta\{1 \pm \sin(2\Delta\xi)\}\{2\Delta \pm p\cos(2\Delta\xi)\}}\right)^2,$$

$$u_{11} = -\frac{p^2}{6} + \frac{2}{3}qr \pm p\left(\frac{2\Delta^2 \csc(2\Delta\xi)\{-p\sin(2\Delta\xi) + 2\Delta\cos(2\Delta\xi) \pm 2\Delta\}}{(2rq - p^2)\cos(2\Delta\xi) - 2\,p\Delta\sin(2\Delta\xi) \pm 2qr}\right)$$
$$-\left(\frac{2\Delta^2 \csc(2\Delta\xi)\{-p\sin(2\Delta\xi) + 2\Delta\cos(2\Delta\xi) \pm 2\Delta\}}{(2rq - p^2)\cos(2\Delta\xi) - 2\,p\Delta\sin(2\Delta\xi) \pm 2qr}\right)^2,$$

$$u_{12} = -\frac{p^2}{6} + \frac{2}{3}qr + p\left(\frac{2\Delta^2 \csc(\Delta\xi)\{p\sin(\Delta\xi) - 2\Delta\cos(\Delta\xi)\}}{2(p^2 - 2rq)\cos^2(\Delta\xi) + 4\Delta\, p\sin(\Delta\xi)\cos(\Delta\xi) - p^2}\right)$$
$$-\left(\frac{2\Delta^2 \csc(\Delta\xi)\{p\sin(\Delta\xi) - 2\Delta\cos(\Delta\xi)\}}{2(p^2 - 2rq)\cos^2(\Delta\xi) + 4\Delta\, p\sin(\Delta\xi)\cos(\Delta\xi) - p^2}\right)^2.$$

Family 2: When $p^2 - 4qr > 0$ and $pq \neq 0$ (or $rq \neq 0$), the soliton and soliton-like solutions of Equation (10) are,

$$u_{13} = -\frac{p^2}{6} + \frac{2}{3}qr + p\left(\frac{2\Omega^2 \sec h^2(\Omega\xi)}{p + 2\Omega\tanh(\Omega\xi)}\right) - \left(\frac{2\Omega^2 \sec h^2(\Omega\xi)}{p + 2\Omega\tanh(\Omega\xi)}\right)^2,$$

where $\Omega = \frac{1}{2}\sqrt{p^2 - 4qr}$, $\xi = x - (p^4 - 8p^2qr + 16q^2r^2)t$ and p, q, r are arbitrary constants.

$$u_{14} = -\frac{p^2}{6} + \frac{2}{3}qr - p\left(\frac{2\Omega^2 \csc h^2(\Omega\xi)}{p + 2\Delta\coth(\Omega\xi)}\right) - \left(\frac{2\Omega^2 \csc h^2(\Omega\xi)}{p + 2\Delta\coth(\Omega\xi)}\right)^2,$$

$$u_{15} = -\frac{p^2}{6} + \frac{2}{3}qr + p\left(\frac{4\Omega^2 \sec h(2\Omega\xi)\left(1 \mp i\sinh(2\Omega\xi)\right)}{p\cosh(2\Omega\xi) + 2\Delta\sinh(2\Omega\xi) \pm i2\Omega}\right)$$
$$-\left(\frac{4\Omega^2 \sec h(2\Omega\xi)\left(1 \mp i\sinh(2\Omega\xi)\right)}{p\cosh(2\Omega\xi) + 2\Delta\sinh(2\Omega\xi) \pm i2\Omega}\right)^2,$$

$$u_{16}=-\frac{p^2}{6}+\frac{2}{3}qr-p\left(\frac{4\Omega^2\csc h(2\Omega\xi)\left(1\pm\cosh(2\Omega\xi)\right)}{p\sinh(2\Omega\xi)+2\Omega\cosh(2\Delta\xi)\pm2\Omega}\right)$$
$$-\left(\frac{4\Omega^2\csc h(2\Omega\xi)\left(1\pm\cosh(2\Omega\xi)\right)}{p\sinh(2\Omega\xi)+2\Omega\cosh(2\Delta\xi)\pm2\Omega}\right)^2,$$

$$u_{17}=-\frac{p^2}{6}+\frac{2}{3}qr-p\left(\frac{\Omega^2\sec h^2(\Omega\xi/2)}{2\left\{\cosh^2(\Omega\xi/2)-1\right\}\left\{p+\Omega\left(\tanh(\Omega\xi/2)+\coth(\Omega\xi/2)\right)\right\}}\right)$$
$$-\left(\frac{\Omega^2\sec h^2(\Omega\xi/2)}{2\left\{\cosh^2(\Omega\xi/2)-1\right\}\left\{p+\Omega\left(\tanh(\Omega\xi/2)+\coth(\Omega\xi/2)\right)\right\}}\right)^2,$$

$$u_{18}=-\frac{p^2}{6}+\frac{2}{3}qr-p\left(\frac{4A\Omega^2\left(A-B\sinh(2\Omega\xi)-\sqrt{A^2+B^2}\cosh(2\Omega\xi)\right)}{\left(A\sin(2\Omega\xi)+B\right)\left(pA\sinh(2\Omega\xi)+pB-2\Omega\sqrt{A^2+B^2}+2A\Omega\cosh(2\Omega\xi)\right)}\right)$$
$$-\left(\frac{4A\Omega^2\left(A-B\sinh(2\Omega\xi)-\sqrt{A^2+B^2}\cosh(2\Omega\xi)\right)}{\left(A\sin(2\Omega\xi)+B\right)\left(pA\sinh(2\Omega\xi)+pB-2\Omega\sqrt{A^2+B^2}+2A\Omega\cosh(2\Omega\xi)\right)}\right)^2,$$

$$u_{19}=-\frac{p^2}{6}+\frac{2}{3}qr-p\left(\frac{4A\Omega^2\left(A-B\sinh(2\Omega\xi)+\sqrt{A^2+B^2}\cosh(2\Omega\xi)\right)}{\left(A\sin(2\Omega\xi)+B\right)\left(pA\sinh(2\Omega\xi)+pB+2\Omega\sqrt{A^2+B^2}+2A\Omega\cosh(2\Omega\xi)\right)}\right)$$
$$-\left(\frac{4A\Omega^2\left(A-B\sinh(2\Omega\xi)+\sqrt{A^2+B^2}\cosh(2\Omega\xi)\right)}{\left(A\sin(2\Omega\xi)+B\right)\left(pA\sinh(2\Omega\xi)+pB+2\Omega\sqrt{A^2+B^2}+2A\Omega\cosh(2\Omega\xi)\right)}\right)^2,$$

where A and B are two non-zero real constants and satisfies the condition $A^2-B^2<0$.

$$u_{20}=-\frac{p^2}{6}+\frac{2}{3}qr-p\left(\frac{2\Omega^2\sec h(\Omega\xi)}{2\Omega\sinh(\Omega\xi)-p\cosh(\Omega\xi)}\right)-\left(\frac{2\Omega^2\sec h(\Omega\xi)}{2\Omega\sinh(\Omega\xi)-p\cosh(\Omega\xi)}\right)^2,$$

$$u_{21}=-\frac{p^2}{6}+\frac{2}{3}qr+p\left(\frac{2\Omega^2\csc h(\Omega\xi)}{2\Omega\cosh(\Omega\xi)-p\sinh(\Omega\xi)}\right)-\left(\frac{2\Omega^2\csc h(\Omega\xi)}{2\Omega\cosh(\Omega\xi)-p\sinh(\Omega\xi)}\right)^2,$$

$$u_{22}=-\frac{p^2}{6}+\frac{2}{3}qr+p\left(\frac{4\Omega^2\sec h(2\Omega\xi)(1\mp i\sinh(2\Omega\xi))}{p\cosh(2\Omega\xi)-2\Omega\sinh(2\Omega\xi)\mp i2\Omega}\right)$$
$$-\left(\frac{4\Omega^2\sec h(2\Omega\xi)(1\mp i\sinh(2\Omega\xi))}{p\cosh(2\Omega\xi)-2\Omega\sinh(2\Omega\xi)\mp i2\Omega}\right)^2,$$

$$u_{23}=-\frac{p^2}{6}+\frac{2}{3}qr+p\left(\frac{4\Omega^2\csc h(2\Omega\xi)(1\pm\cosh(2\Omega\xi))}{2\Omega\cosh(2\Omega\xi)-p\sinh(2\Omega\xi)\pm2\Omega}\right)$$
$$-\left(\frac{4\Omega^2\csc h(2\Omega\xi)(1\pm\cosh(2\Omega\xi))}{2\Omega\cosh(2\Omega\xi)-p\sinh(2\Omega\xi)\pm2\Omega}\right)^2,$$

$$u_{24}=-\frac{p^2}{6}+\frac{2}{3}qr+p\left(\frac{2\Omega^2\csc h(\Omega\xi)}{2\Omega\cosh(\Omega\xi)-p\sinh(\Omega\xi)}\right)-\left(\frac{2\Omega^2\csc h(\Omega\xi)}{2\Omega\cosh(\Omega\xi)-p\sinh(\Omega\xi)}\right)^2.$$

Family 3: When $r=0$ and $pq\neq 0$, the solutions of Equation (10) are,

$$u_{25}=-\frac{p^2}{6}+\frac{2}{3}qr+p\left(\frac{p(\cosh(p\xi)-\sinh(p\xi))}{d+\cosh(p\xi)-\sinh(p\xi)}\right)-\left(\frac{p(\cosh(p\xi)-\sinh(p\xi))}{d+\cosh(p\xi)-\sinh(p\xi)}\right)^2,$$

$$u_{26}=-\frac{p^2}{6}+\frac{2}{3}qr+p\left(\frac{pd}{d+\cosh(p\xi)+\sinh(p\xi)}\right)-\left(\frac{pd}{d+\cosh(p\xi)+\sinh(p\xi)}\right)^2.$$

Family 4: When $q\neq 0$ and $r=p=0$, the solutions of Equation (10) are,

$$u_{27}=-\frac{p^2}{6}+\frac{2}{3}qr-p\left(\frac{q}{q\xi+c_1}\right)-\left(\frac{q}{q\xi+c_1}\right)^2,$$

where c_1 is an arbitrary constant.

Because of the arbitrariness of the parameters p, q and r in the above families of solution, the physical quantities u and v may possess rich structures.

Graph is a powerful tool for communication and describes lucidly the solutions of the problems. Therefore, some graphs of the solutions are given below (Graph 1a to h). The graphs readily have shown the solitary wave form of the solutions.

New approach of (*G`/G*)-expansion method

To convert Equation (10) into ODE we used the following transformation

$$u(x,t)=u(\xi),\ \xi=kx+\omega t, \qquad (17)$$

where k and ω are arbitrary constant. Substituting Equation (17) into (10) and using the chain rule and $\xi_x=k, \xi_t=\omega$, we obtain

$$\omega u'+30k^3uu'''+30k^3u'u''+180ku^2u'+k^5u''''=0. \qquad (18)$$

Integrating the above equation once, ignoring the constant of integration equal to zero we have the following equation

$$\omega u+60ku^3+30k^3uu''+k^5u''''=0.$$

For *m* = 2, we obtained the trail solution

$$u=a_0+a_1\left(\frac{G(\xi)'}{G(\xi)}\right)+a_2\left(\frac{G(\xi)'}{G(\xi)}\right)^2. \qquad (19)$$

where $G(\xi)$ satisfying the following Riccati equation

$$G(\xi)G''(\xi)-\delta_1G^2(\xi)+\delta_2\left(G'(\xi)\right)^2=0. \qquad (20)$$

Putting Equation (20) into (18) coupled with auxiliary equation; the Equation (18) yields an algebraic equation involving power of $\left(\frac{G(\xi)'}{G(\xi)}\right)$ as

$$C_0\left(\frac{G(\xi)'}{G(\xi)}\right)^0+C_1\left(\frac{G(\xi)'}{G(\xi)}\right)^1+C_2\left(\frac{G(\xi)'}{G(\xi)}\right)^2+C_3\left(\frac{G(\xi)'}{G(\xi)}\right)^3+\cdots+C_6\left(\frac{G(\xi)'}{G(\xi)}\right)^6=0.$$

Compare the like powers of $\left(\frac{G(\xi)'}{G(\xi)}\right)$ we have system of equations

$$\left(\frac{G(\xi)'}{G(\xi)}\right)^0: \quad -16k^5a_2\delta_1^3\delta_2-16k^5a_2\delta_1^3+\omega a_0+60ka_0^3+60k^3a_0a_2\delta_1^2=0,$$

$$\left(\frac{G(\xi)'}{G(\xi)}\right)^1: \quad -60k^3a_0a_1\delta_1\delta_2-60k^3a_0a_1\delta_1+60k^3a_1a_2\delta_1^2+\cdots+16k^5a_1\delta_1^2=0,$$

$$\left(\frac{G(\xi)'}{G(\xi)}\right)^2: \quad -60\delta_1a_1^2k^2+180ka_0a_1^2-240k^3a_0a_2\delta_1\delta_2+\cdots+60k^3a_2^2\delta_1^2=0,$$

$$\left(\frac{G(\xi)'}{G(\xi)}\right)^3: \quad -300k^3a_1a_2\delta_1\delta_2+360ka_0a_1a_2-300k^3a_1a_2\delta_1+\cdots-40k^5a_1\delta_1=0,$$

$$\left(\frac{G(\xi)'}{G(\xi)}\right)^4: \quad 180ka_2^2a_0+360k^3a_0a_2\delta_2+180k^3a_0a_2\delta_2+\cdots-240k^5a_2\delta_1=0,$$

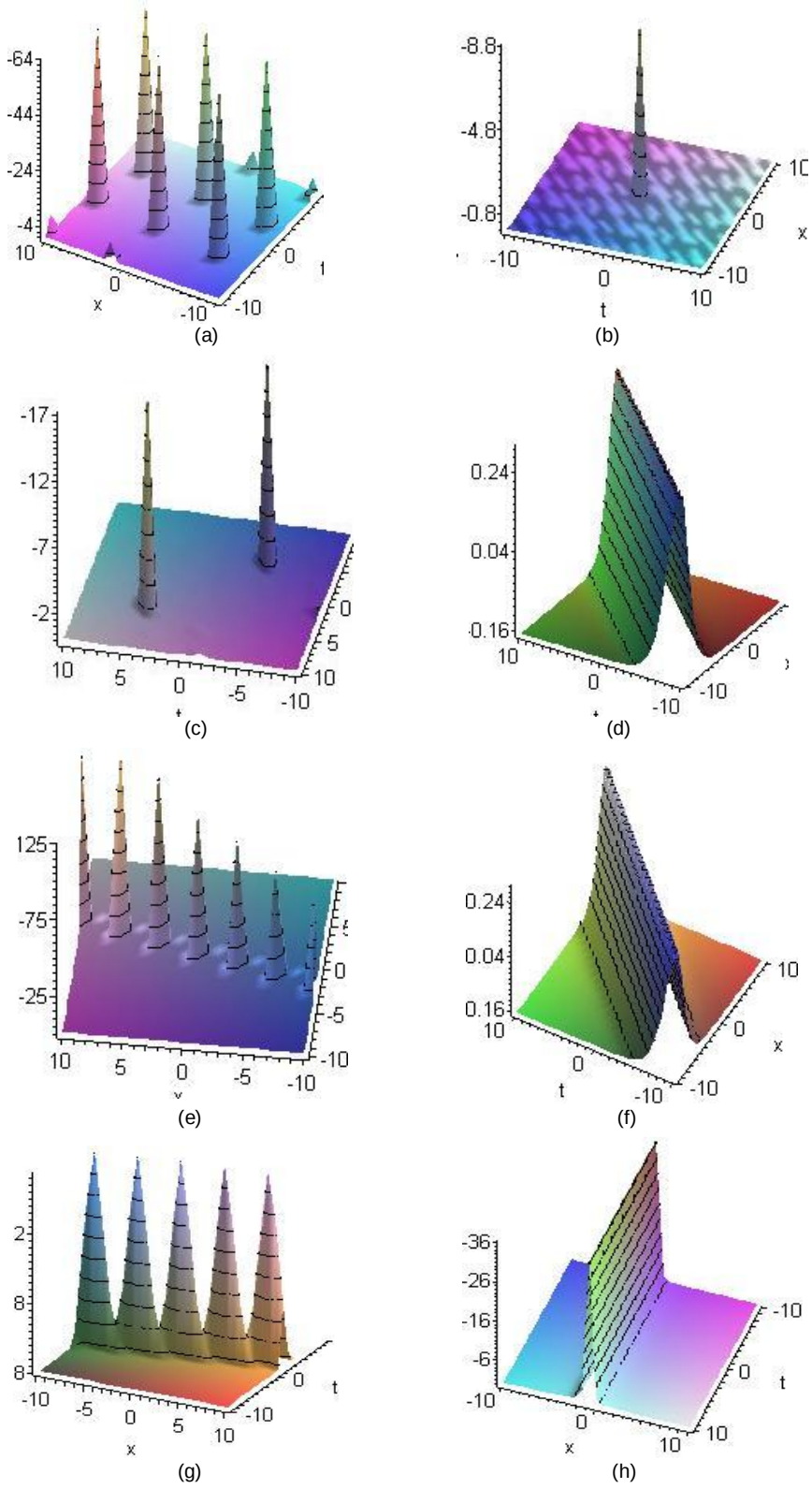

Graph 1. Solitons corresponding to solutions (a) u_1 for $p=q=r=1$ (b) u_2 for $p=q=1, r=2$ (c) u_8 for $p=q=r=2$ (d) u_{13} for $p=3, q=2, r=1$ (e) u_{14} for $p=2, q=1, r=0.5$ (f) u_{20} for $p=3, q=1, r=2$ (g) u_{26} for $p=1.5, q=1, r=0$ (h) u_{27} for $p=0, q=1, r=0$.

$\left(\frac{G(\xi)'}{G(\xi)}\right)^5$: $240k^3a_1a_2\delta_2^2 + 480k^3a_1a_2\delta_2 + 24k^5a_1 + \cdots + 96k^5a_1\delta_2 = 0,$

$\left(\frac{G(\xi)'}{G(\xi)}\right)^6$: $60ka_2^3 + 180k^3a_2^2 + 120k^5a_2\delta_2^4 + 120k^5a_2 + \cdots + 480k^5a_2\delta_2 = 0.$

Solving the above system for unknown parameters, we have the following solution sets.

1st solution set

$k = k, \omega = -16k^5(\delta_2^2 + 2\delta_2 + 1)\delta_1^2, a_0 = k^2\delta_1 + k^2\delta_1\delta_2\ , a_1 = 0, a_2 = -k^2(\delta_2^2 + 2\delta_2 + 1).$

Family 1: When $\delta_1, \delta_2 \neq 0,$

$$u(\xi) = k^2\delta_1 + k^2\delta_1\delta_2 - k^2(\delta_2^2 + 2\delta_2 + 1)\left(\frac{G'(\xi)}{G(\xi)}\right)^2,$$

where $\left(\frac{G'(\xi)}{G(\xi)}\right) = \frac{\left[\cosh\left(2\sqrt{\delta_1(1+\delta_2)}\xi\right)+\sinh\left(2\sqrt{\delta_1(1+\delta_2)}\xi\right)\right]\sqrt{\delta_1}+\sqrt{\delta_1}}{\left[\cosh\left(2\sqrt{\delta_1(1+\delta_2)}\xi\right)+\sinh\left(2\sqrt{\delta_1(1+\delta_2)}\xi\right)\right]\sqrt{1+\delta_2}-\sqrt{1+\delta_2}}.$

Family 2: When $\delta_1 < 0$, and $(1 + \delta_2) > 0$, or $\delta_1 > 0$, and $(1 + \delta_2) < 0$

$$u(\xi) = k^2\delta_1 + k^2\delta_1\delta_2 - k^2(\delta_2^2 + 2\delta_2 + 1)\left(\frac{G'(\xi)}{G(\xi)}\right)^2,$$

where $\left(\frac{G'(\xi)}{G(\xi)}\right) = \frac{\left[\cos\left(2\sqrt{-\delta_1(1+\delta_2)}\xi\right)-\sin\left(2\sqrt{-\delta_1(1+\delta_2)}\xi\right)\right]\sqrt{-\delta_1}+\sqrt{-\delta_1}}{\left[\cos\left(2\sqrt{-\delta_1(1+\delta_2)}\xi\right)+\sin\left(2\sqrt{-\delta_1(1+\delta_2)}\xi\right)\right]\sqrt{1+\delta_2}-\sqrt{1+\delta_2}}.$

Family 3: When $\delta_1 \neq 0$, and $\delta_2 = 0,$

$$u(\xi) = k^2\delta_1 + k^2\delta_1\delta_2 - k^2(\delta_2^2 + 2\delta_2 + 1)\left(\frac{G'(\xi)}{G(\xi)}\right)^2,$$

where $\left(\frac{G'(\xi)}{G(\xi)}\right) = \frac{\left[\cosh\left(2\sqrt{\delta_1}\xi\right)+\sinh\left(2\sqrt{\delta_1}\xi\right)\right]\sqrt{\delta_1}+\sqrt{\delta_1}}{\left[\cosh\left(2\sqrt{\delta_1}\xi\right)+\sinh\left(2\sqrt{\delta_1}\xi\right)\right]-1}.$

Family 4: When $\delta_1 = 0$, and $\delta_2 \neq 0,$

$$u(\xi) = k^2\delta_1 + k^2\delta_1\delta_2 - k^2(\delta_2^2 + 2\delta_2 + 1)\left(\frac{G'(\xi)}{G(\xi)}\right)^2,$$

where $\left(\frac{G'(\xi)}{G(\xi)}\right) = \frac{1}{1+\xi}\frac{1}{1+\delta_2}.$

Family 5: When $\delta_1 = 0$, and $\delta_2 = 0.$

$$u(\xi) = k^2\delta_1 + k^2\delta_1\delta_2 - k^2(\delta_2^2 + 2\delta_2 + 1)\left(\frac{G'(\xi)}{G(\xi)}\right)^2,$$

where $\left(\frac{G'(\xi)}{G(\xi)}\right) = \frac{1}{1+\xi}.$

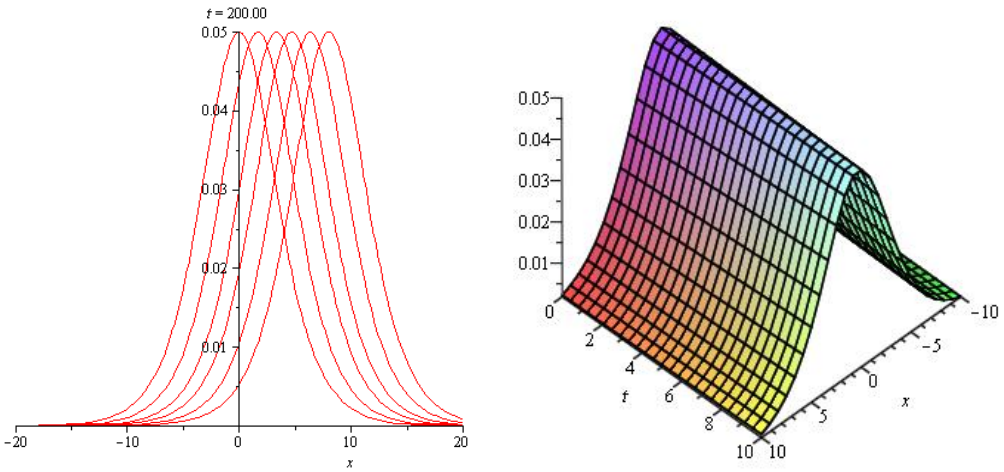

(a) (b)

Graph 2. (a) 2D and (b) 3D travelling wave solutions of Equation (10) for different values of parameters.

In all cases $\xi = kx - 16k^5(\delta_2^2 + 2\delta_2 + 1)\delta_1^2\, t.$

Graph 2a and b show 2D and 3D travelling wave solutions of Equation (10) for different values of parameters.

2nd solution set

$$k = k, \omega = 60k^5\delta_1^2\left(\frac{1}{2}+\frac{1}{30}\sqrt{105}\right)\delta_2^2 + 120k^5\delta_1^2\left(\frac{1}{2}+\frac{1}{30}\sqrt{105}\right)\delta_2 + 60k^5\delta_1^2\left(\frac{1}{2}+\frac{1}{30}\sqrt{105}\right) - 52k^5\delta_1^2\delta_2^2 - 104k^5\delta_2\delta_1^2 - 52k^5\delta_1^2, a_0 = \left(\frac{1}{2}+\frac{1}{30}\sqrt{105}\right)(\delta_2+1)\delta_1k^2, a_1 = 0, a_2 = -k^2(\delta_2^2+2\delta_2+1).$$

Family 1: When $\delta_1, \delta_2 \neq 0,$

$$u(\xi) = \left(\frac{1}{2}+\frac{1}{30}\sqrt{105}\right)(\delta_2+1)\delta_1k^2 - k^2(\delta_2^2+2\delta_2+1)\left(\frac{G'(\xi)}{G(\xi)}\right)^2,$$

where $\left(\frac{G'(\xi)}{G(\xi)}\right) = \frac{\left[\cosh\left(2\sqrt{\delta_1(1+\delta_2)}\xi\right)+\sinh\left(2\sqrt{\delta_1(1+\delta_2)}\xi\right)\right]\sqrt{\delta_1}+\sqrt{\delta_1}}{\left[\cosh\left(2\sqrt{\delta_1(1+\delta_2)}\xi\right)+\sinh\left(2\sqrt{\delta_1(1+\delta_2)}\xi\right)\right]\sqrt{1+\delta_2}-\sqrt{1+\delta_2}}.$

Family 2: When $\delta_1 < 0,$ and $(1+\delta_2) > 0,$ or $\delta_1 > 0,$ and $(1+\delta_2) < 0$

$$u(\xi) = \left(\frac{1}{2}+\frac{1}{30}\sqrt{105}\right)(\delta_2+1)\delta_1k^2 - k^2(\delta_2^2+2\delta_2+1)\left(\frac{G'(\xi)}{G(\xi)}\right)^2,$$

where $\left(\frac{G'(\xi)}{G(\xi)}\right) = \frac{\left[\cos\left(2\sqrt{-\delta_1(1+\delta_2)}\xi\right)-\sin\left(2\sqrt{-\delta_1(1+\delta_2)}\xi\right)\right]\sqrt{-\delta_1}+\sqrt{-\delta_1}}{\left[\cos\left(2\sqrt{-\delta_1(1+\delta_2)}\xi\right)+\sin\left(2\sqrt{-\delta_1(1+\delta_2)}\xi\right)\right]\sqrt{1+\delta_2}-\sqrt{1+\delta_2}}.$

Family 3: When $\delta_1 \neq 0,$ and $\delta_2 = 0,$

$$u(\xi) = \left(\frac{1}{2}+\frac{1}{30}\sqrt{105}\right)(\delta_2+1)\delta_1k^2 - k^2(\delta_2^2+2\delta_2+1)\left(\frac{G'(\xi)}{G(\xi)}\right)^2,$$

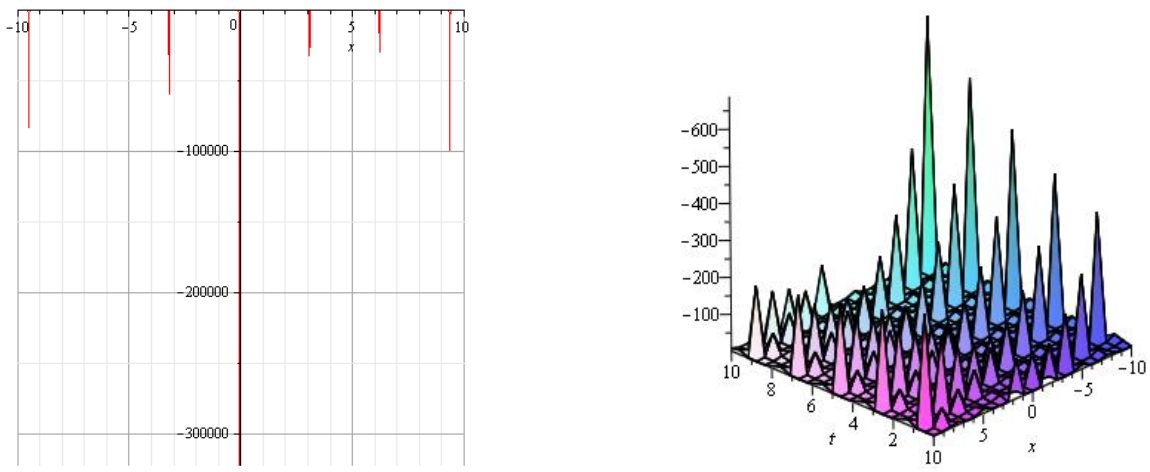

(a) (b)

Graph 3. (a) 2D and (b) 3D periodic wave solutions of Equation (10) for different values of parameters.

where $\left(\frac{G'(\xi)}{G(\xi)}\right) = \frac{[\cosh(2\sqrt{\delta_2}\xi)+\sinh(2\sqrt{\delta_2}\xi)]\sqrt{\delta_2}+\sqrt{\delta_2}}{[\cosh(2\sqrt{\delta_2}\xi)+\sinh(2\sqrt{\delta_2}\xi)]-1}$.

Family 4: When $\delta_1 = 0$, and $\delta_2 \neq 0$,

$$u(\xi) = \left(\frac{1}{2}+\frac{1}{30}\sqrt{105}\right)(\delta_2+1)\delta_1 k^2 - k^2(\delta_2^2+2\delta_2+1)\left(\frac{G'(\xi)}{G(\xi)}\right)^2,$$

where $\left(\frac{G'(\xi)}{G(\xi)}\right) = \frac{1}{1+\xi}\frac{1}{1+\delta_2}$.

Family 5: When $\delta_1 = 0$, and $\delta_2 = 0$.

$$u(\xi) = \left(\frac{1}{2}+\frac{1}{30}\sqrt{105}\right)(\delta_2+1)\delta_1 k^2 - k^2(\delta_2^2+2\delta_2+1)\left(\frac{G'(\xi)}{G(\xi)}\right)^2,$$

where $\left(\frac{G'(\xi)}{G(\xi)}\right) = \frac{1}{1+\xi}$.

In all cases $\xi = kx + \left[\begin{array}{c} 60k^5\delta_1^2\left(\frac{1}{2}+\frac{1}{30}\sqrt{105}\right)\delta_2^2 + 120k^5\delta_1^2\left(\frac{1}{2}+\frac{1}{30}\sqrt{105}\right)\delta_2 + \\ 60k^5\delta_1^2\left(\frac{1}{2}+\frac{1}{30}\sqrt{105}\right) - 52k^5\delta_1^2\delta_2^2 - 104k^5\delta_2\delta_1^2 - 52k^5\delta_1^2 \end{array}\right]t.$

Graph 3a and b show 2D and 3D periodic wave solutions of Equation (10) for different values of parameters.

3rd solution set

$$\begin{aligned} k = k, \omega = {} & 60k^5\delta_1^2\left(\frac{1}{2}-\frac{1}{30}\sqrt{105}\right)\delta_2^2 + 120k^5\delta_1^2\left(\frac{1}{2}-\frac{1}{30}\sqrt{105}\right)\delta_2 \\ & + 60k^5\delta_1^2\left(\frac{1}{2}-\frac{1}{30}\sqrt{105}\right) - 52k^5\delta_1^2\delta_2^2 - 104k^5\delta_2\delta_1^2 - 52k^5\delta_1^2, a_0 \\ & = \left(\frac{1}{2}-\frac{1}{30}\sqrt{105}\right)(\delta_2+1)\delta_1 k^2, a_1 = 0, a_2 = -k^2(\delta_2^2+2\delta_2+1). \end{aligned}$$

Family 1: When $\delta_1, \delta_2 \neq 0$,

$$u(\xi) = \left(\frac{1}{2} - \frac{1}{30}\sqrt{105}\right)(\delta_2 + 1)\delta_1 k^2 - k^2(\delta_2^2 + 2\delta_2 + 1)\left(\frac{G'(\xi)}{G(\xi)}\right)^2,$$

where $\left(\frac{G'(\xi)}{G(\xi)}\right) = \frac{\left[\cosh\left(2\sqrt{\delta_2(1+\delta_2)}\xi\right)+\sinh\left(2\sqrt{\delta_2(1+\delta_2)}\xi\right)\right]\sqrt{\delta_2}+\sqrt{\delta_2}}{\left[\cosh\left(2\sqrt{\delta_2(1+\delta_2)}\xi\right)+\sinh\left(2\sqrt{\delta_2(1+\delta_2)}\xi\right)\right]\sqrt{1+\delta_2}-\sqrt{1+\delta_2}}$.

Family 2: When $\delta_1 < 0$, and $(1 + \delta_2) > 0$, or $\delta_1 > 0$, and $(1 + \delta_2) < 0$

$$u(\xi) = \left(\frac{1}{2} - \frac{1}{30}\sqrt{105}\right)(\delta_2 + 1)\delta_1 k^2 - k^2(\delta_2^2 + 2\delta_2 + 1)\left(\frac{G'(\xi)}{G(\xi)}\right)^2,$$

where $\left(\frac{G'(\xi)}{G(\xi)}\right) = \frac{\left[\cos\left(2\sqrt{-\delta_2(1+\delta_2)}\xi\right)-\sin\left(2\sqrt{-\delta_2(1+\delta_2)}\xi\right)\right]\sqrt{-\delta_2}+\sqrt{-\delta_2}}{\left[\cos\left(2\sqrt{-\delta_2(1+\delta_2)}\xi\right)+\sin\left(2\sqrt{-\delta_2(1+\delta_2)}\xi\right)\right]\sqrt{1+\delta_2}-\sqrt{1+\delta_2}}$.

Family 3: When $\delta_1 \neq 0$, and $\delta_2 = 0$,

$$u(\xi) = \left(\frac{1}{2} - \frac{1}{30}\sqrt{105}\right)(\delta_2 + 1)\delta_1 k^2 - k^2(\delta_2^2 + 2\delta_2 + 1)\left(\frac{G'(\xi)}{G(\xi)}\right)^2,$$

where $\left(\frac{G'(\xi)}{G(\xi)}\right) = \frac{\left[\cosh\left(2\sqrt{\delta_2}\xi\right)+\sinh\left(2\sqrt{\delta_2}\xi\right)\right]\sqrt{\delta_2}+\sqrt{\delta_2}}{\left[\cosh\left(2\sqrt{\delta_2}\xi\right)+\sinh\left(2\sqrt{\delta_2}\xi\right)\right]-1}$.

Family 4: When $\delta_1 = 0$, and $\delta_2 \neq 0$,

$$u(\xi) = \left(\frac{1}{2} - \frac{1}{30}\sqrt{105}\right)(\delta_2 + 1)\delta_1 k^2 - k^2(\delta_2^2 + 2\delta_2 + 1)\left(\frac{G'(\xi)}{G(\xi)}\right)^2,$$

where $\left(\frac{G'(\xi)}{G(\xi)}\right) = \frac{1}{1+\xi}\frac{1}{1+\delta_2}$.

Family 5: When $\delta_1 = 0$, and $\delta_2 = 0$.

$$u(\xi) = \left(\frac{1}{2} - \frac{1}{30}\sqrt{105}\right)(\delta_2 + 1)\delta_1 k^2 - k^2(\delta_2^2 + 2\delta_2 + 1)\left(\frac{G'(\xi)}{G(\xi)}\right)^2,$$

where $\left(\frac{G'(\xi)}{G(\xi)}\right) = \frac{1}{1+\xi}$.

In all cases $\xi = kx + \left[\begin{array}{c} 60k^5\delta_1^2\left(\frac{1}{2} - \frac{1}{30}\sqrt{105}\right)\delta_2^2 + 120k^5\delta_1^2\left(\frac{1}{2} - \frac{1}{30}\sqrt{105}\right)\delta_2 + \\ 60k^5\delta_1^2\left(\frac{1}{2} - \frac{1}{30}\sqrt{105}\right) - 52k^5\delta_1^2\delta_2^2 - 104k^5\delta_2\delta_1^2 - 52k^5\delta_1^2 \end{array}\right]t.$

Graph 4a and b show 2D and 3D periodic wave solutions of Equation (10) for different values of parameters.

(*U`/U*)-expansion method

For *m* = 2, we obtained the trail solution

$$u = a_0 + a_1\left(\frac{U(\xi)'}{U(\xi)}\right) + a_2\left(\frac{U(\xi)'}{U(\xi)}\right)^2. \qquad (21)$$

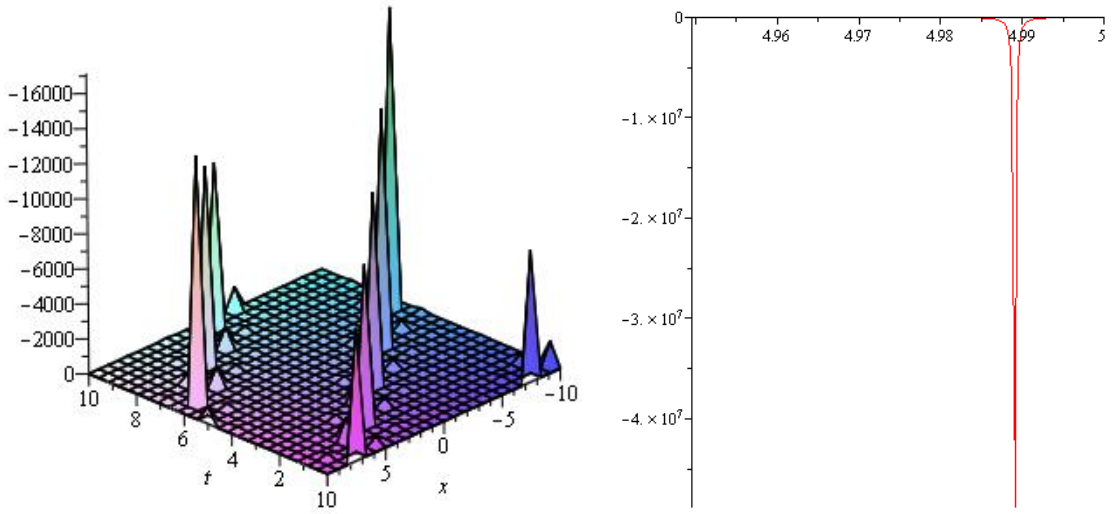

(a) (b)

Graph 4. (a) 2D and (b) 3D periodic wave solutions of Equation (10) for different values of parameters.

where $G(\xi)$ satisfying the following Riccati equation

$$U'(\xi) = AU + B. \tag{22}$$

Putting Equation (22) into (18) coupled with auxiliary equation; the Equation (18) yields an algebraic equation involving power of $\left(\frac{G(\xi)'}{G(\xi)}\right)$ as

$$\frac{1}{U^6}(C_0U^0 + C_1U^1 + C_2U^2 + C_3U^3 + \cdots + C_6U^6) = 0.$$

Compare the like powers of U we have system of equations

$$U^0: \quad 120B^6k^5a_2 + 180k^3B^6a_2^2 + 60ka_2^3B^6 = 0,$$

$$U^1: \quad 180ka_1B^5a_2^2 + 360ka_2^3AB^5 + 240k^3B^5a_1a_2 + \cdots + 24B^5k^5a_1 = 0,$$

$$U^2: \quad 180ka_0a_2^2B^4 + 180ka_1^2B^4a_2 + 900ka_2^3A^2B^4 + \cdots + 60k^3a_1^2B^4 = 0,$$

$$U^3: \quad 1200ka_2^3A^3B^3 + 60k^3B^3a_0a_1 + 150k^3B^3a_1^2A + \cdots + 360ka_0a_1B^3a_2 = 0,$$

$$U^4: \quad 1080ka_0a_1A^2a_2B + 180ka_0^2a_1B + 180ka_1^3A^2B + \cdots + 1080ka_2^2a_0A^2B^2 = 0,$$

$$U^5: \quad 1080ka_0a_1Aa_2B^2 + 180ka_1a_0^2B + 180ka_1^3A^2B + \cdots + 2\omega Aa_2B = 0,$$

$$U^6: \quad 180ka_0a_2^2A^4 + 180ka_0a_1^2A^2 + 180ka_0^2a_1A + \cdots + 180ka_0^2a_1A = 0.$$

Solving the above system for unknown parameters, we have the following solution sets

1st solution set

$$k = k, \omega = -k^5A^4, a_0 = 0\ , a_1 = k^2A, a_2 = -k^2,$$

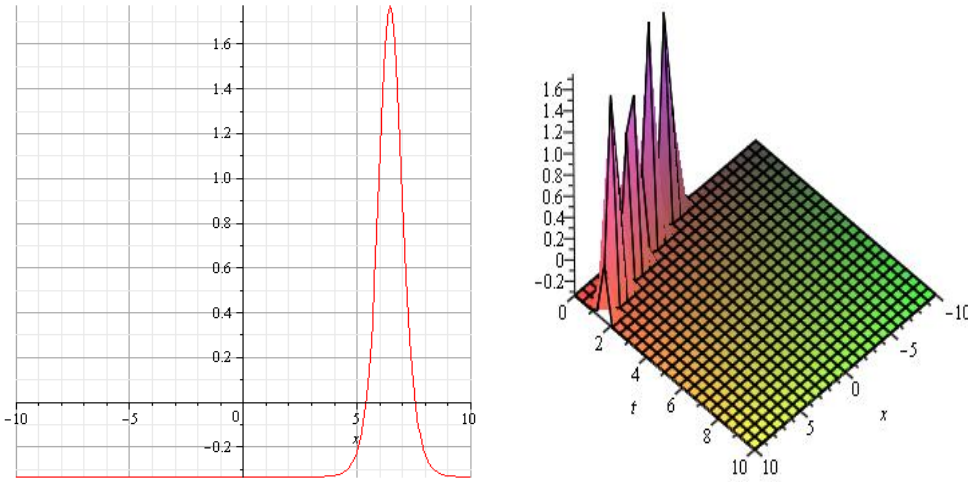

Graph 5. (a) 2D and (b) 3D travelling wave solutions of Equation (10) for different values of parameters.

Substituting the solution set into trial solution

$$u(\xi) = k^2 A \left(\frac{A e^{A(kx-k^5A^4t)}}{-\frac{B}{A}+e^{A(kx-k^5A^4t)}} \right) - k^2 \left(\frac{A e^{A(kx-k^5A^4t)}}{-\frac{B}{A}+e^{A(kx-k^5A^4t)}} \right)^2,$$

Graph 5a and b show 2D and 3D travelling wave solutions of Equation (10) for different values of parameters.

2nd solution set

$$k = \frac{\sqrt{-15a_0+\sqrt{105}\,a_0}}{A}, \omega = -\frac{60\sqrt{-15a_0+\sqrt{105}\,a_0}\,a_0^2}{A}, a_0 = a_0, a_1 = \frac{-15a_0+\sqrt{105}\,a_0}{A}, a_2 = -\frac{-15a_0+\sqrt{105}\,a_0}{A^2},$$

Substituting the solution set into trial solution

$$u(\xi) = a_0 + \frac{-15a_0+\sqrt{105}\,a_0}{A} \left(\frac{A e^{A\frac{\sqrt{-15a_0+\sqrt{105}\,a_0}}{A}(x-60a_0^2t)}}{-\frac{B}{A}+e^{A\frac{\sqrt{-15a_0+\sqrt{105}\,a_0}}{A}(x-60a_0^2t)}} \right) - \frac{-15a_0+\sqrt{105}\,a_0}{A^2} \left(\frac{A e^{A\frac{\sqrt{-15a_0+\sqrt{105}\,a_0}}{A}(x-60a_0^2t)}}{-\frac{B}{A}+e^{A\frac{\sqrt{-15a_0+\sqrt{105}\,a_0}}{A}(x-60a_0^2t)}} \right)^2,$$

Graph 6a and b show 2D and 3D travelling wave solutions of Equation (10) for different values of parameters.

3rd solution set

$$k = -\frac{\sqrt{-15a_0+\sqrt{105}\,a_0}}{A}, \omega = \frac{60\sqrt{-15a_0+\sqrt{105}\,a_0}\,a_0^2}{A}, a_0 = a_0, a_1 = \frac{-15a_0+\sqrt{105}\,a_0}{A}, a_2 = -\frac{-15a_0+\sqrt{105}\,a_0}{A^2},$$

Substituting the solution set into trial solution

$$u(\xi) = a_0 + \frac{-15a_0+\sqrt{105}\,a_0}{A} \left(\frac{A e^{-A\frac{\sqrt{-15a_0+\sqrt{105}\,a_0}}{A}(x-60a_0^2t)}}{-\frac{B}{A}+e^{-A\frac{\sqrt{-15a_0+\sqrt{105}\,a_0}}{A}(x-60a_0^2t)}} \right) - \frac{-15a_0+\sqrt{105}\,a_0}{A^2} \left(\frac{A e^{-A\frac{\sqrt{-15a_0+\sqrt{105}\,a_0}}{A}(x-60a_0^2t)}}{-\frac{B}{A}+e^{-A\frac{\sqrt{-15a_0+\sqrt{105}\,a_0}}{A}(x-60a_0^2t)}} \right)^2,$$

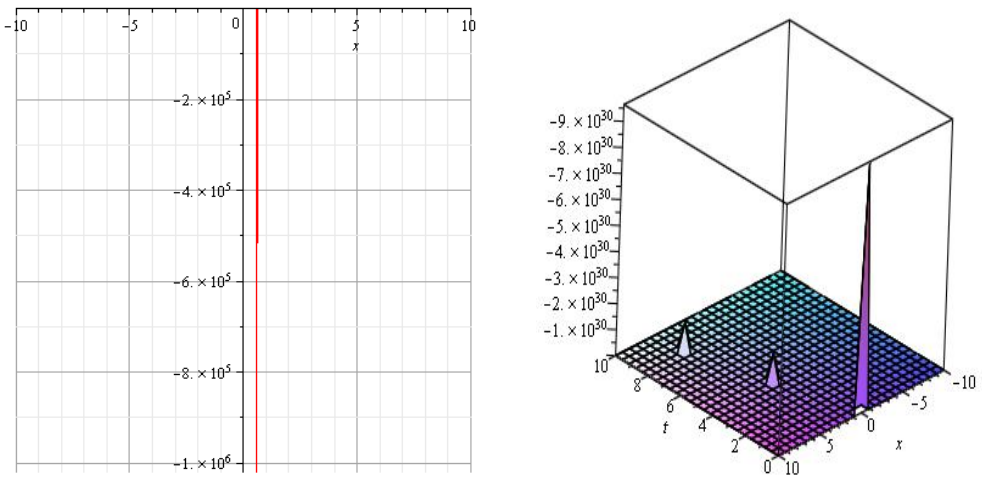

Graph 6. (a) 2D and (b) 3D travelling wave solutions of Equation (10) for different values of parameters.

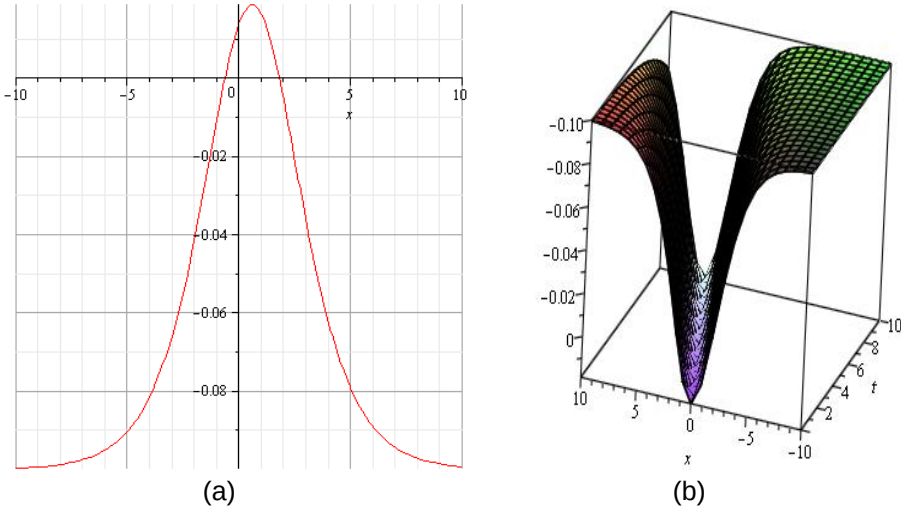

Graph 7. (a) 2D and (b) 3D travelling wave solutions of Equation (10) for different values of parameters.

Graph 7a and b show 2D and 3D travelling wave solutions of Equation (10) for different values of parameters.

4th solution set

$$k=\frac{\sqrt{-15a_0-\sqrt{105}\,a_0}}{A},\omega=-\frac{60\sqrt{-15a_0-\sqrt{105}\,a_0}\,a_0^2}{A},a_0=a_0,a_1=\frac{-15a_0-\sqrt{105}\,a_0}{A},a_2=-\frac{-15a_0-\sqrt{105}\,a_0}{A^2},$$

Substituting the solution set into trial solution

$$u(\xi)=a_0+\frac{-15a_0-\sqrt{105}\,a_0}{A}\left(\frac{Ae^{\frac{\sqrt{-15a_0-\sqrt{105}\,a_0}}{A}\left(x-60a_0^2t\right)}}{-\frac{B}{A}+e^{\frac{\sqrt{-15a_0-\sqrt{105}\,a_0}}{A}\left(x-60a_0^2t\right)}}\right)-\frac{-15a_0-\sqrt{105}\,a_0}{A^2}\left(\frac{Ae^{\frac{\sqrt{-15a_0-\sqrt{105}\,a_0}}{A}\left(x-60a_0^2t\right)}}{-\frac{B}{A}+e^{\frac{\sqrt{-15a_0-\sqrt{105}\,a_0}}{A}\left(x-60a_0^2t\right)}}\right)^2,$$

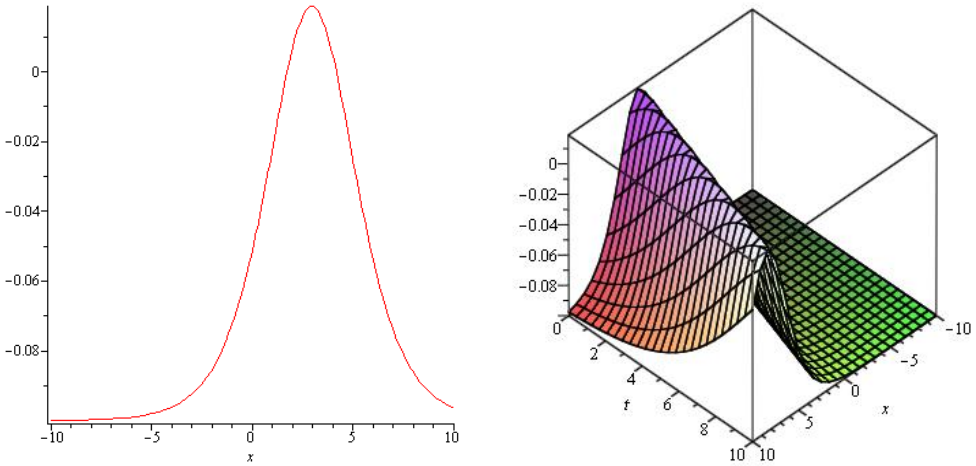

Graph 8. (a) 2D and (b) 3D travelling wave solutions of Equation (10) for different values of parameters.

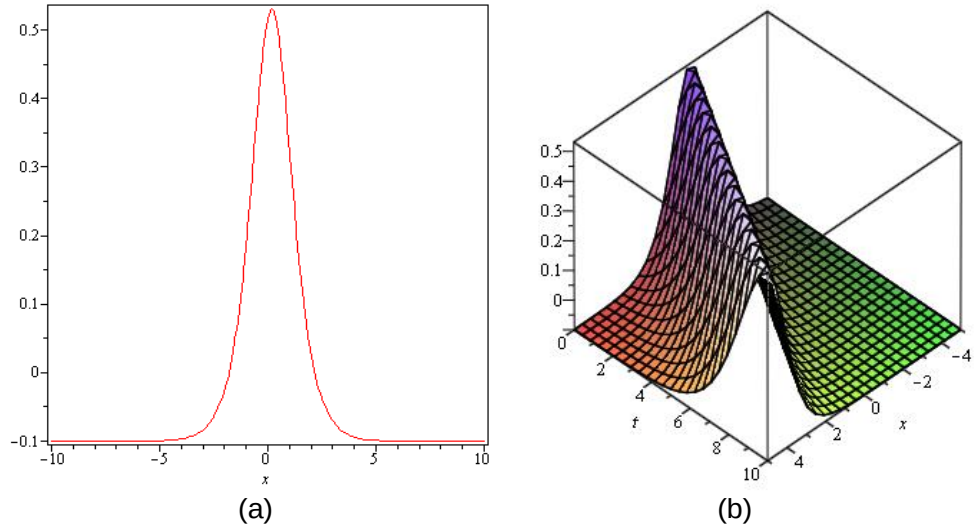

Graph 9. (a) 2D and (b) 3D travelling wave solutions of Equation (10) for different values of parameters.

Graph 8a and b show 2D and 3D travelling wave solutions of Equation (10) for different values of parameters.

5th solution set

$$k = -\frac{\sqrt{-15a_0-\sqrt{105}\,a_0}}{A}, \omega = \frac{60\sqrt{-15a_0-\sqrt{105}\,a_0}\,a_0^2}{A}, a_0 = a_0, a_1 = \frac{-15a_0-\sqrt{105}\,a_0}{A}, a_2 = -\frac{-15a_0-\sqrt{105}\,a_0}{A^2},$$

Substituting the solution set into trial solution

$$u(\xi) = a_0 + \frac{-15a_0-\sqrt{105}\,a_0}{A}\left(\frac{Ae^{-\frac{\sqrt{-15a_0-\sqrt{105}\,a_0}}{A}\left(x-60a_0^2t\right)}}{-\frac{B}{A}+e^{-\frac{\sqrt{-15a_0-\sqrt{105}\,a_0}}{A}\left(x-60a_0^2t\right)}}\right) - \frac{-15a_0-\sqrt{105}\,a_0}{A^2}\left(\frac{Ae^{-\frac{\sqrt{-15a_0-\sqrt{105}\,a_0}}{A}\left(x-60a_0^2t\right)}}{-\frac{B}{A}+e^{-\frac{\sqrt{-15a_0-\sqrt{105}\,a_0}}{A}\left(x-60a_0^2t\right)}}\right)^2,$$

Graph 9a and b show 2D and 3D travelling wave solutions of Equation (10) for different values of parameters.

Conclusion

Alternative (G'/G)-expansion along with the generalized Riccati equation and (U'/U)-expansion methods are successfully used for searching abundant exact travelling wave solutions to the (1+1)-dimensional CDG equation with the help of symbolic computation. Numerical results re-confirm the efficiency of the proposed algorithms. It is concluded that suggested schemes can be extended for other kinds of NLEEs in mathematical physics.

REFERENCES

Abazari R (2010). The (G'/G)-expansion method for Tziteica type nonlinear evolution equations. Math. Comput. Model. 52:1834-1845.

Abbasbandy S (2007a). A new application of He's variational iteration method for quadratic Riccati differential equation by using Adomian's polynomials. J. Comput. Appl. Math. 207:59-63.

Abbasbandy S (2007b). Numerical solutions of nonlinear Klein-Gordon equation by variational iteration method. Int. J. Numer. Meth. Engr. 70:876-881.

Abdollahzadeh M, Hosseini M, Ghanbarpour M, Shirvani H (2010). Exact traveling solutions for fifth order Caudrey-Dodd-Gibbon equation. Int. J. Appl. Math. Comput. 2(4):81-90.

Abdou MA, Soliman AA, Basyony ST (2007). New application of exp-function method for improved Boussinesq equation. Phys. Lett. A 369:469-475.

Adomian G (1994). Solving frontier problems of physics: The decomposition method, Boston, MA: Kluwer Academic.

Akbar MA, Ali NHM (2011a). The modified alternative (G'/G)-expansion method for finding the exact solutions of nonlinear PDEs in mathematical physics. Int. J. Phys. Sci. 6(35):7910-7920.

Akbar MA, Ali NHM (2011b). Exp-function method for Duffing equation and new solutions of (2+1) dimensional dispersive long wave equations. Prog. Appl. Math. 1(2):30-42.

Ali AT (2011). New generalized Jacobi elliptic function rational expansion method. J. Comput. Appl. Math. 235:4117-4127.

Bekir A (2008). Application of the (G'/G)-expansion method for nonlinear evolution equations. Phys. Lett. A 372:3400-3406.

Gardner CS, Greene JM, Kruskal MD, Miura RM (1967). A method for solving the Korteweg–de Vries equation. Phys. Rev. Lett. 19:1095-1099.

He JH, Wu XH (2006). Exp-function method for nonlinear wave equations. Chaos Solit. Fract. 30:700-708.

Hirota R (1971). Exact solution of the KdV equation for multiple collisions of Solitons. Phys. Rev. Lett. 27:1192-1194.

Jiang B, Bi Q (2010). A study on the bilinear Caudrey-Dodd-Gibbon equation. Nonlin. Anal. 72:4530-4533.

Jin L (2010). Application of the variational iteration method for solving the fifth order Caudrey-Dodd-Gibbon equation. Int. Math. Forum 5(66):3259-3265.

Liao SJ (1992a). The Homotopy Analysis Method and its applications in mechanics. Ph.D. Dissertation (in English). Shanghai Jiao Tong University.

Liao SJ (1992b). A kind of linear invariance under homotopy and some simple applications of it in mechanics. Bericht Nr. 520, Institut fuer Schifl'bau der Universitaet Hamburg.

Liu X, Tian L, Wu Y (2010). Exact solutions of the generalized Benjamin-Bona-Mahony equation. Math. Prob. Engr. Article ID 796398, 5 pages, doi:10.1155/2010/796398.

Malfliet M (1992). Solitary wave solutions of nonlinear wave equations. Am. J. Phys. 60:650–654.

Mohyud-Din ST (2007). Homotopy perturbation method for solving fourth-order boundary value problems. Math. Prob. Engr. Article ID 98602, doi:10.1155/2007/98602.

Mohyud-Din ST (2008). Variational iteration method for solving fifth-order boundary value problems using He's polynomials. Math. Prob. Engr. Article ID 954794, doi: 10:1155/2008/954794.

Mohyud-Din ST, Noor MA, Noor KI (2009). Some relatively new techniques for nonlinear problems. Math. Prob. Engr. Article ID 234849, doi:10.1155/2009/234849.

Mohyud-Din ST, Noor MA, Waheed A (2010). Exp-function method for generalized travelling solutions of Calogero-Degasperis-Fokas equation. Zeitschrift für Naturforschung A- A J. Phys. Sci. 65a:78-84.

Mohyud-Din ST, Yildirim A, Demirli G (2011a). Analytical solution of wave system in R^n with coupling controllers. Int. J. Numer. Meth. Heat Fluid Flow, Emerald 21:198-205.

Mohyud-Din ST, Yildirim A, Sariaydin S (2011b). Numerical soliton solution of the Kaup–Kuper shmidt equation. Int. J. Numer. Meth. Heat Fluid Flow, Emerald 21(3):272-281.

Naher H, Abdullah FA, Akbar MA (2011a). The (G'/G)-expansion method for abundant travelling wave solutions of Caudrey-Dodd-Gibbon equation. Math. Prob. Engr. Article ID 218216, 11 pp. doi:10.1155/2011/218216.

Naher H, Abdullah FA, Akbar MA (2011b). The exp-function method for new exact solutions of the nonlinear partial differential equations. Int. J. Phys. Sci. 6(29):6706-6716.

Rogers C, Shadwick WF (1982). Backlund Transformations. Academic Press, New York.

Shi Y, Dai Z, Han S, Huang L (2010). The multi-wave method for nonlinear evolution equations. Math. Comput. Appl. 15(5):776-783.

Taghizadeh N, Mirzazadeh M (2011). The first integral method to some complex nonlinear partial differential equations. J. Comput. Appl. Math. 235:4871-4877.

Usman M, Yildirim A, Mohyud-Din ST (2011). A Reliable algorithm for physical problems, Int. J. Phys. Sci. 6(1):146-153.

Wang ML (1996). Exact solutions for a compound KdV-Burgers equation. Phys. Lett. A 213:279-287.

Wang ML, Li X, Zhang J (2008). The (G'/G)-expansion method and traveling wave solutions of nonlinear evolution equations in mathematical physics. Phys. Lett. A 372:417-423.

Wazwaz MA (2009). Partial Differential Equations and Solitary Waves Theory. Springer Dordrecht Heidelberg, London, New York.

Xu Y, Zhou X, Yao L (2008). Solving the fifth order Caudrey-Dodd-Gibbon (CDG) equation using the Exp-function method. Appl. Math. Comput. 206:70-73.

Zayed EME (2009a). The (G'/G)-expansion method and its applications to some nonlinear evolution equations in the mathematical physics. J. Appl. Math. Comput. 30:89-103.

Zayed EME (2009b). New traveling wave solutions for higher dimensional nonlinear evolution equations using a generalized (G'/G)-expansion method. J. Phys. A: Math. Theor. 42:195202-195214.

Zayed EME, Gepreel KA (2009). The (G'/G)-expansion method for finding traveling wave solutions of nonlinear PDEs in mathematical physics. J. Math. Phys. 50:013502-013513.

Zayed EME, Al-Joudi S (2010). Applications of an extended (G'/G)-expansion method to find exact solutions of nonlinear PDEs in mathematical physics. Math. Prob. Engr. Article ID 768573, doi: 10.1155/2010/768573.

Zayed EME (2011). The (G'/G)-expansion method combined with the Riccati equation for finding exact solutions of nonlinear PDEs. J. Appl. Math. Inf. 29(1-2):351-367.

Zhang S, Tong J, Wang W (2008a). A generalized (G'/G)-expansion method for the mKdV equation with variable coefficients. Phys. Lett. A 372:2254-2257.

Zhang J, Wei X, Lu Y (2008b). A generalized (G'/G)-expansion method and its applications. Phys. Lett. A 372:3653-3658.

Zhang J, Jiang F, Zhao X (2010). An improved (G'/G)-expansion method for solving nonlinear evolution equations. Int. J. Comput. Math. 87:1716-1725.

Zheng C, Qiang J, Wang S (2010). Standing, periodic and solitary wave in (1+1)-dimensional Caudrey-Dodd-Gibbon-sawada-Kotera system.

Commun. Theor. Phys. 54:1054-1058.
Zhou YB, Wang ML, Wang YM (2003). Periodic wave solutions to coupled KdV equations with variable coefficients. Phys. Lett. A 308:31–36.
Zhu S (2008). The generalized Riccati equation mapping method in non-linear evolution equation: Application to (2+1)-dimensional Boiti-Leon-Pempinelle equation. Chaos Solit. Fract. 37:1335-1342.

academicJournals

Vol. 8(37), pp. 1857-1861, 9 October, 2013
DOI: 10.5897/IJPS2013.3952
ISSN 1992 - 1950 © 2013 Academic Journals
http://www.academicjournals.org/IJPS

International Journal of Physical Sciences

Full Length Research Paper

A tuneable metamaterial design using microelectromechanical system (MEMS) based split ring resonator (SRR)

Tanuj Kumar Garg[1]*, S. C. Gupta[2], S. S. Patnaik[3] and Vipul Sharma[1]

[1]Deptartment of Electronics and Communication Engineering, Gurukul Kangri University, Haridwar, India.
[2]Deptartment of Electronics and Communication Engineering, DIT, Dehradun, India.
[3]Deptartment of ETV, NITTTR, Sector-26, Chandigarh, India.

Accepted 26 September, 2013

In this paper, we present a study of tuneable equilateral triangular shaped spilt ring resonator (ETSRR). In this ETSRR we rotate the inner and outer rings by varying the position of the splits in rings. For this we used radio frequency microelectromechanical system (RF MEMS) switches. By making MEMS switches ON/OFF, the positions of splits in the rings were varied which can be considered as rotation of rings. As we rotate the inner and outer rings (by varying the position of splits), the configuration is tuned to different frequency from its basic configuration, thus we get tunability.

Key words: Split ring resonator (SRR), metamaterials, equilateral triangle, radio frequency microelectromechanical system (RF MEMS) switch.

INTRODUCTION

Nowadays, metamaterial becomes most popular among the researchers because it shows simultaneously negative values of effective permittivity (ε_{eff}) and effective permeability (μ_{eff}) over a common frequency band. Metamaterials are also regarded as left handed materials (LHMs) or negative refractive index materials (NIMs) because these materials exhibits the properties like backward propagation, reverse Doppler effect and reverse Vavilov - Cerenkov effect which are not possessed by natural material (Ziolkowski, 2003). The negative values of effective permittivity (ε_{eff}) can be obtained by using metal rod and effective permeability (μ_{eff}) can be obtained by Split ring (Huang et al., 2010). The design of metamaterial based on shape and geometry is most popular work among the others. Various types of ring type structures like circular, square, U-shaped, S- shaped, Ω- shaped, elliptical shaped, phi-shaped (Sharma et al., 2011) have been proposed till now. The split ring resonator (SRR) structures which are most famous, circular or rectangular. The triangular shaped metamaterial resonator was first studied by Sabah and Uckun (2008) although now few studies are there in literature (Zhu et al., 2009; Jalali et al., 2009; Sabah, 2010). Metamaterials can also be used in antenna designing to enhance the gain and directivity of the antennas (Wu et al., 2005; Lee and Hao, 2008; Gil et al., 2006; Qureshi et al., 2005).

Compared to PIN diodes and FET transistors, RF MEMS switches have better performance in terms of isolation, insertion loss, power consumption and linearity (Muldavin et al., 2000a, 2000b).

Wang et al. (2008) purposed a theory about SRR with

*Corresponding author. E-mail: tanujkgarg@rediffmail.com

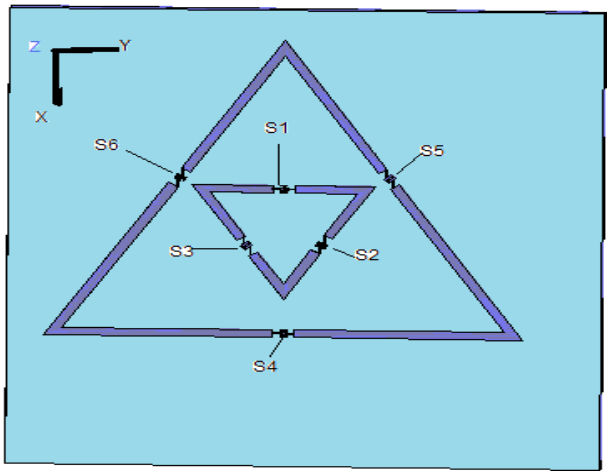

Figure 1. Equilateral triangular spilt ring resonator with splits and RF MEMS switches in each arm.

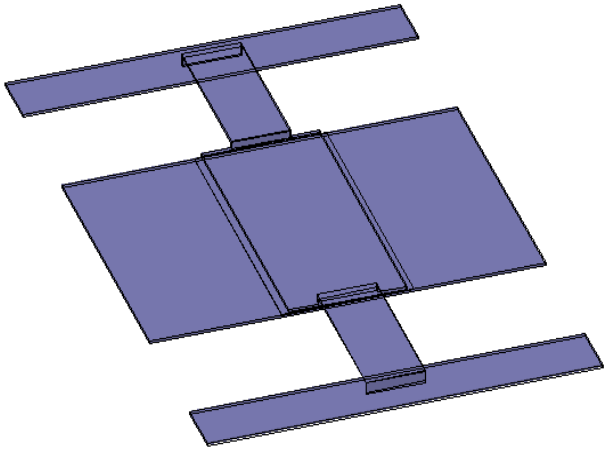

Figure 2. The structure of RF MEMS shunt switch.

rotated inner ring to analyze the controllability of its magnetic resonant frequency. The inner ring was rotated by means of control bars and by rotation of inner ring as the angle between the two splits decreases magnetic resonant frequency increases.

Sabah (2010) proposed tuneable metamaterial (MTM) structure composed of triangular spilt ring resonator and wire strip. These MTMs are formed from FR4 and RT/duriod 5880 substrates show tunability in terms of substrate thickness. The results shown are very promising.

The rotation of rings can also be achieved by putting splits in each arm of rings and then the position of splits can be made ON/OFF by using MEMS switches. By this, the magnetic resonant frequency gets shifted and thus getting tunability.

In present paper, authors have obtained frequency tuneable MTM triangular SRR (Sabah, 2010) by rotating the inner (Wang et al., 2008) and outer ring. The rotation of rings is implemented by change in position of splits in each arm by using MEMS switches. Excellent performance is achieved.

DESIGN

In this design, RogersRT /duriod5880 (relative permittivity = 2.2) is used as a substrate with a thickness of 0.8 mm .The length and width of the substrate is 28 and 30 mm, respectively. The dimensions of outer ETSRR base length is 22.52 mm and height is 19.5 mm; 8.66 and 7.52 mm for inner ETSRR.

The separation between outer and inner ETSRR is 9.5 mm from vertex of outer ETSRR to base of inner ETSRR. The width of each strip is 0.5 mm. The split gap in each ETSRR is 1.0 mm. Splits are made at each arm of inner and outer ETSRR along with RF MEMS switches placed in each split. Switches S1, S2, S3 are placed in inner ETSRR and switches S4, S5, S6 are placed in outer ETSRR. The proposed design is shown in Figure 1.

The structure of RF MEMS shunt switch (Figure 2) consist of thin metal (gold in this case) membrane bridge that is suspended over the central conductor of coplanar waveguide (CPW) and fixed on the ground conductor. The dimensions of shunt switch are: length of the bridge = 200 µm, width of the bridge = 90 µm, thickness of the bridge = 2 µm, silicon nitrate (relative permittivity = 7) is used as the dielectric having a thickness of 0.2 µm, air gap between lower conductor and upper conductor is 0.9 µm.

When a switch is in ON position in a particular arm, that means there is no split in that particular arm; whereas, when the switch is in OFF position, then it means there is presents of a split in that arm. The whole structure is designed and placed in two port waveguide formed by a pair of both perfect magnetic conductor (PMC) walls in z-direction and perfect electric conductor (PEC) walls in y-direction. The whole structure is excited by an electromagnetic wave with propagation vector in x-direction. The structure is designed and simulated by using Ansoft HFSS simulator, finite element based electro-magnetic mode solver.

To show the physical properties of the designed structure, S parameters are calculated and effective permeability is extracted by using effective parameter retrieval method (Smith et al., 2005).

ANALYSIS AND DISCUSSION

Metamaterials type structures can be considered as LC resonant circuit whose resonance frequency can be determined by $\omega = 1/\sqrt{LC}$. When the switch S4 was OFF in outer ETSRR and switch S1 was OFF in inner ETSRR, while rest of switches were ON (Figure 3a); the

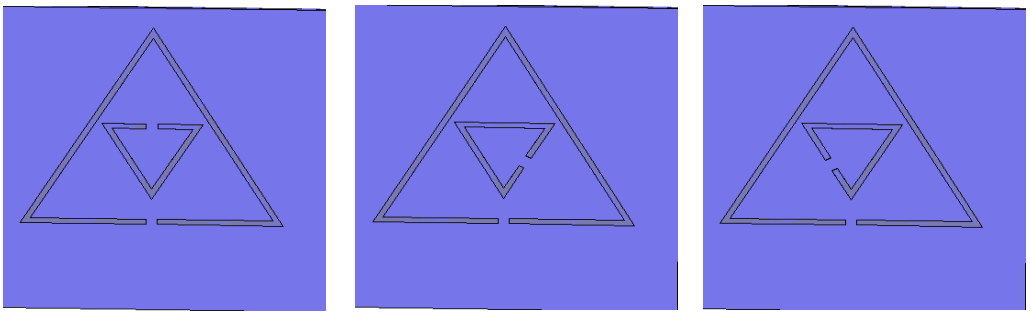

Figure 3. ETSRR Configuration: When switch S4 in outer ETSRR is OFF and (a) switch S1, (b) switch S3, (c) switch S2 in inner ETSRR are OFF; and rest of the switches are ON.

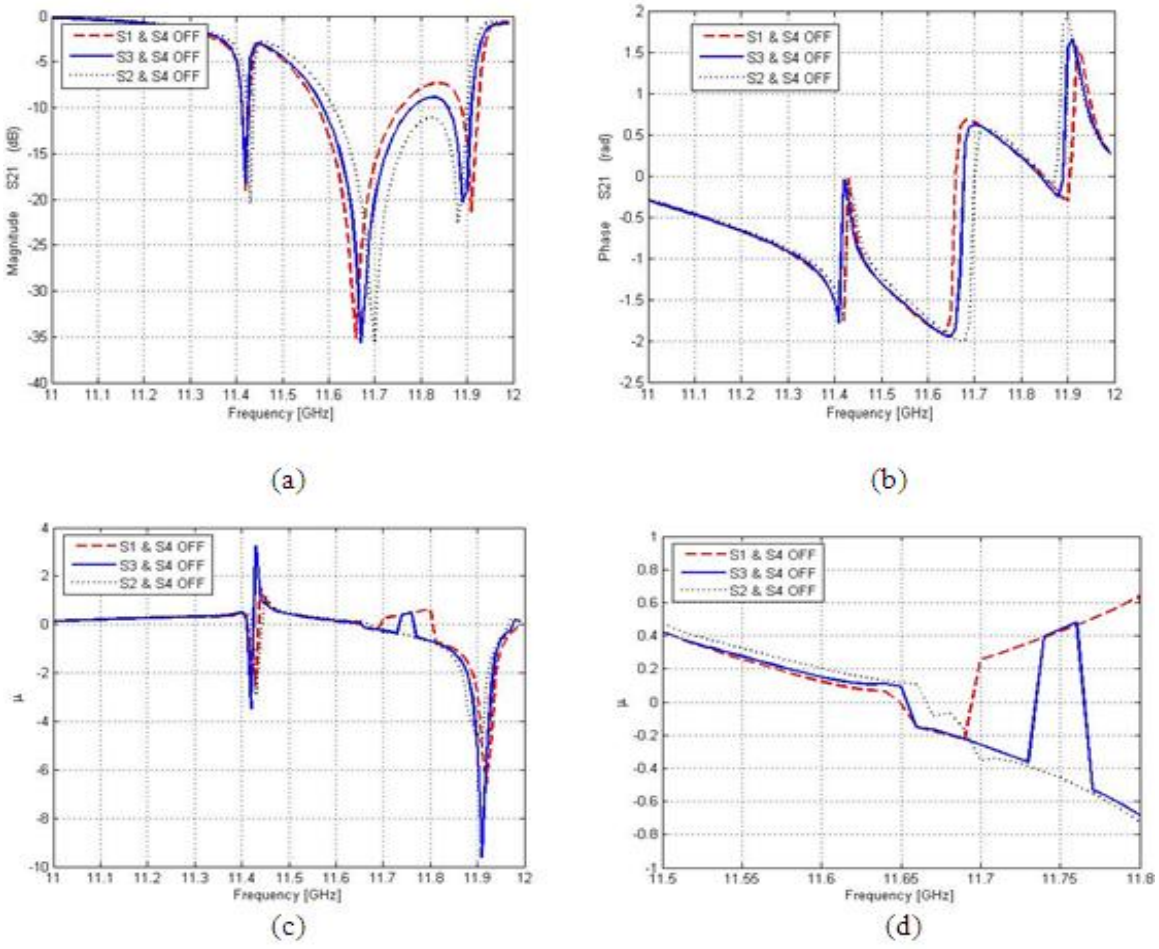

Figure 4. (a) minimum of transmission (S_{21}) in dB, (b) dip in phase of S_{21} (rad), (c) effective permeability, (d) Zoom of effective permeability.

minimum of transmission (S_{21}) was observed at 11.66 GHz (Figure 4a, red curve), the dip in phase of S_{21} was observed at 11.63 GHz, (Figure 4b), red curve), negative permeability occurred in frequency regime 11.65 GHz ~ 11.69 GHz (Figure 4c), red curve), but they overlap each other at frequency 11.66 GHz. Because of negative permeability, EM waves cannot transmit through the structure which result in dip in transmission spectrum. In the original ETSRR the angle between two splits is π.

Now, when we rotated the inner ring by making the

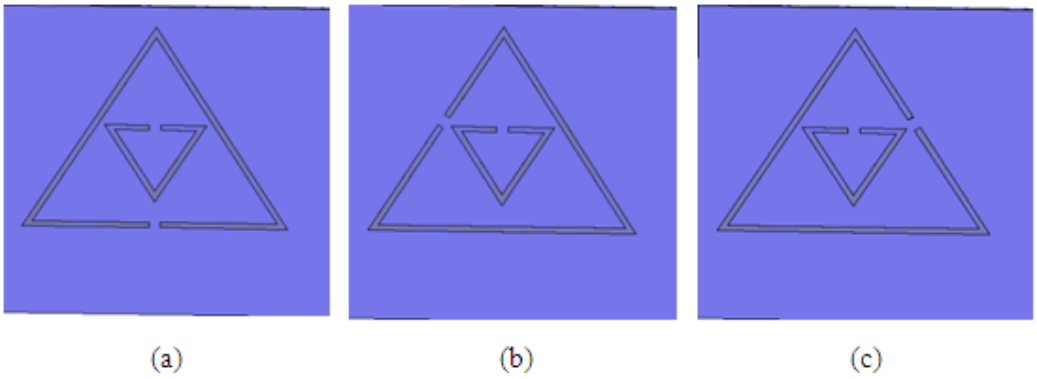

Figure 5. ETSRR Configuration: When switch S1 in inner ETSRR is OFF and (a) switch S4, (b) switch S6, (c) switch S5 in outer ETSRR are OFF; and rest of the switches are ON.

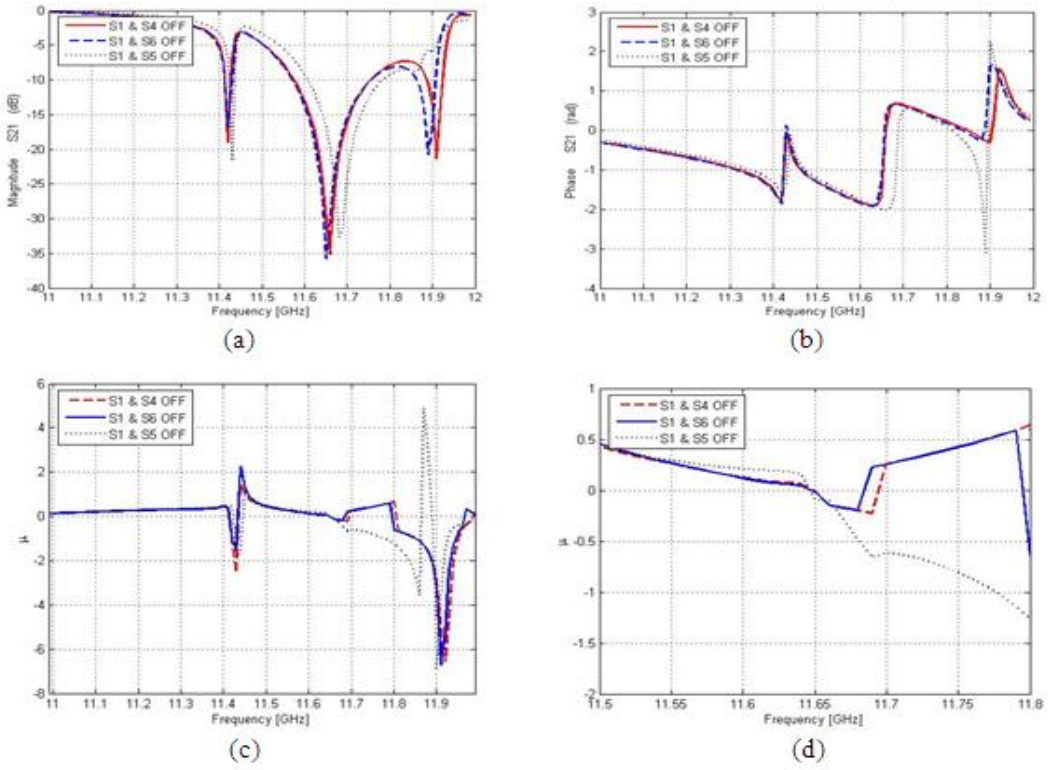

Figure 6. (a) minimum of transmission (S_{21}) in dB, (b) dip in phase of S_{21} (rad), (c) effective permeability, (d) Zoom of effective permeability.

switch S1 transit from OFF to ON position and S3 or S2 were transited from ON to OFF position in inner ETSRR (S4 in outer ETSRR remained OFF) while rest of the switches remained as they were (Figure 3b, c); the minimum of transmission (S_{21}) were shifted to higher frequency 11.67 GHz (Figure 4a) blue curve) and 11.70 GHz (Figure 4a) black curve), and the dip in phase of S_{21} were also shifted to higher frequency (Figure 4b) blue and black curve); accordingly, the negative permeability frequency regime shifted to 11.66 GHz ~ 11.73 GHz (Figure 4c, blue curve) and 11.67 GHz ~11.96 GHz (Figure 4c, black curve), respectively. Thus, by rotating the inner ring, the angle between the two splits decreases, so the resonant frequency shifted to higher side.

When we rotated the outer ring by making the switch S4 transit from OFF to ON position and S6 or S5 were transit from ON to OFF position in outer ETSRR (S1 in inner ETSRR remained OFF) while rest of the switches remained as they were (Figure 5b, c); the minimum of

transmission (S_{21}) were shifted to higher frequency 11.65 GHz (Figure 6a, blue curve) and 11.68 GHz (Figure 6(a) black curve), and the dip in phase of S_{21} were also shifted to higher frequency (Figure 6b, blue and black curve); accordingly, the negative permeability frequency regime shifted to 11.65 GHz ~ 11.68 GHz (Figure 4(c) blue curve) and 11.65 GHz ~11.86 GHz (Figure 4(c) black curve), respectively. Thus, by rotating the outer ring, the angle between the two splits decreases, so the resonant frequency shifted to higher side.

Thus, we can control the magnetic resonant frequency by rotating the inner and outer ETSRR. In each case, the configuration is tuned to different frequency. If we compare this with purposed technique in Sabah (2010) in which he got tunability by varying the substrate thickness; the technique presented in this paper is easy to get tunability because in this we rotate the rings by means of MEMS switches (making then ON/OFF to make splits present or not); as well as from technique presented in Wang et al. (2008) in which they rotated the inner ring by using control bars.

Conclusion

In this paper we design an equilateral triangle shaped split ring resonator with their basic configuration. Then we varied the position of splits in inner ring by using RF MEMS switches (making them ON/OFF) that was considered as the inner ETSRR was rotated. So by rotation of inner ring, the configuration was tuned to different frequency. Similarly, when we rotated the outer ring by varied the position of splits in outer ring using MEMS switches; the configuration was again tuned to different frequency. So, by rotation of inner or outer ring, we can control the magnetic resonant frequency and thus we get tunability. This ETSRR can be used in antenna design to obtain high directivity and high gain of the antennas.

REFERENCES

Gil I, Bonache J, García-García J, Martín F (2006). Tunable Metamaterial Transmission Lines Based on Varactor-Loaded Split-Ring Resonators. IEEE Trans. Microw. Theory Technol. 54:6.

Huang C, Zhao Z, Feng Q, Cui J, Luo X (2010). Metamaterial composed of wire pairs exhibiting dual band negative refraction. Appl. Phys. B Laser Optics 98:365-370.

Jalali M, Sedgji T, Zehforoosh Y (2009). Miniaturization of waveguides dual band antenna using TSRR-WS metamaterials. Int. J. Comput. Electr. Eng. 1:1793-8163.

Lee Y, Hao Y (2008). Characterization Of Microstrip Patch Antennas On Metamaterial Substrates Loaded With Complementary Split-Ring Resonators. Microw. Optical Techn. Lett. 50:8.

Muldavin B, Rebeiz GM (2000a). High-Isolation CPW MEMS Shunt Switches - Part 1: Modeling. IEEE Trans. Microw. Theory Techn. 48:1045-1052.

Muldavin JB, Rebeiz GM (2000b). High-Isolation CPW MEMS Shunt Switches - Part 2: Design. IEEE Trans. Microw. Theory Techn. 48(6):1053-1056.

Qureshi F, Antoniades MA, Eleftheriades GV (2005). A Compact and Low profile Metamaterial Ring Antenna with Vertical Polarization. IEEE Antennas Wireless Propag. Lett. Vol. 4.

Sabah C (2010). Tunable Metamaterial Design Composed of Triangular Split Ring Resonator and Wire Strip for S- and C- Microwave Bands. Prog. Electrom. Res. B, 22:341-357.

Sabah C, Uckun S (2008). Triangular split ring resonator and wire strip to form new metamaterial, Proc. Of XXIX General Assembly of Int. Union of Radio Science.

Sharma V, Pattnaik SS, Garg T, Devi S (2011). A metamaterials inspired miniaturized phi-shaped antenna. Int. J. Phys. Sci. 6(18):4378-4381.

Smith DR, Vier DC, Koschny T, Soukoulis CM (2005). Electromagnetic parameter retrieval from inhomogeneous metamaterials, Phy. Rev. E, 71.

Wang J, Qu A, Xu Z, Ma H, Yang Y, Gu C (2008). A Controllable Magnetic Metamaterial: Split Ring Resonator with Rotated Inner Ring, IEEE Trans. Antennas Propag. 56:7.

Wu BI, Wang W, Pacheco J, Chen X, Grzegorczyk T, Kong JA (2005). A Study Of Using Metamaterials As Antenna Substrate To Enhance Gain. Prog. Electromag. Res., PIER 51:295-328.

Zhu C, Ma JJ, Chen L, Liang CH (2009). Negative index metamaterials composed of triangular open loop resonator and wire structures. Microw. Optical Tech. Lett. 51:2022-2025.

Ziolkowski RW (2003). Design, fabrication, and testing of double negative metamaterials. IEEE Trans. Antennas Propag. 51:1516-152.

academicJournals

Vol. 8(37), pp. 1862-1872, 9 October, 2013
DOI: 10.5897/IJPS2013.3965
ISSN 1992 - 1950 © 2013 Academic Journals
http://www.academicjournals.org/IJPS

International Journal of Physical Sciences

Full Length Research Paper

A Google map-based traffic accident reconstruction system

Chun-Chia Hsu[1], Chih-Yung Lin[2] and Chin-Ping Fung[3]*

[1]Department of Cultural Creativity and Digital Media Design, Lunghwa University of Science and Technology, Gueishan, Taoyuan County, Taiwan, Republic of China.
[2]Department of Multi-media and Game Science, Lunghwa University of Science and Technology, Gueishan, Taoyuan County, Taiwan, Republic of China.
[3]Department of Mechanical Engineering, Oriental Institute of Technology, Panchiao, New Taipei City, Taiwan, Republic of China.

Accepted 26 September, 2013

Both traffic accident reconstruction and responsibility confirmation of traffic accident depend on crash scene diagramming and crash simulation. However, mistakenly recorded road geometry of the crash scene usually causes misunderstandings in the crash scene diagramming and thus the result of accident reconstruction is untrustworthy. Research has thus been continuously done to solve the problem. This study proposed a Google Map-based accident reconstruction system integrating functions of crash scene diagramming and crash simulation. The modulus of crash scene diagramming includes positioning of accident location, Google satellite map and Google Sketch Up to accurately present road geometry and accident vehicle position information. The modulus of crash simulation refers to the vehicle dynamic differential equations generated using the Newton-Euler formulation, and enhances with the calculation of momentum conservation in the collision to predict the vehicle dynamics after collision. The system developed in this study was validated using a real case. The results showed that a crash scene diagramming correctly drawn on the Google satellite map was an ideal platform to present the crush simulation, and help people understand or make a judgment for accident authentication.

Key words: Accident reconstruction, Google map, crash scene diagramming, crash simulation.

INTRODUCTION

The crash scene diagramming is important for making a judgment on accident authentication as it is used to interpret the crash scene and to be frequently contrasted with the police accident record to reconstruct the accident scene. In order to clean up the obstacles on the road after a traffic accident and restore the passage as soon as possible, the police used to make a sketch of crash scene first at the accident site, using paper and pen. Then based on the sketch the police would further draw a crash scene diagramming using computer software for a formal police report. Nowadays the software of crash scene diagramming has developed well to support police and it has been on the market for a period of time. Crash Zone (The CAD Zone, Inc., 2012) is a full-functioned software of crash scene diagramming and crash simulation. It is used to draw a 2-D crash scene diagramming according to the data measured by police from the accident site. The 2-D diagramming can be further transformed to a 3-D scene. With the built-in tools, Crash Zone calculates the sliding speed and angle of each vehicle after crash. Then the traffic accident is reconstructed and showed with an animation after setting

*Corresponding author. E-mail: cpfung@mail.oit.edu.tw. Tel: +886-2-77380145. Fax: +886-2-77386648.

specific before-crash driving paths to separate vehicles. Easy Street Draw (A-T Solutions Inc., 2012) can be used to draw a 2-D crash scene diagramming by selecting a pre-drawn street diagram and editing the diagram according to the real road geometry from the accident scene. With the items in its built-in traffic symbol database, the process of crash scene diagramming is speeded. The office of Traffic Accident Management in China developed the traffic accident scene scale map software (2012) that could quickly draw a scale map of crash scene diagramming according to measurements recorded in a crash scene sketch and using built-in objects in the software such as people, vehicle, road, tyre skid mark, and debris. An Hui Keli Information Industry Co., LTD (2012) also developed a crash scene diagramming system with a laser range finder for police officers to quickly manage traffic accident. The system offers functions of zoom-in and zoom-out, symbols of automobile, non-automobile, human body, path, road, and accident type, and geometry database of line, curve, rectangle, circle, and ellipse. The commercially available software has its own characteristics, however, the accuracy of the crash scene diagramming in road geometry done by those software is based on a crash scene sketch and measurements recorded by police officers. In addition, not all package software has the function of CAD to set relations between different dimensions and maintain the same scale when plotting multiple lines and curves, and therefore, the defect usually causes misunderstanding in the relative positions of the human body, vehicle, tyre skid mark, and debris. If the road geometry of the crash scene is not completely or mistakenly recorded, it usually causes scale distortion in the crash scene diagramming. Most of the problems are not easily detected in the process of drawing crash scene diagramming, and the correction of drawing always takes much more time to finish.

The crash scene diagramming can also be made from photographs. Fenton and Kerr (1997) presented a technique that enables the user to create an accurate accident scene diagram from one photograph of the accident scene, by using a combination of processes called Inverse Camera Projection and Photographic Rectification. Chen and Chao (2006) also developed a fast mapping system for road accident by using digital close range photogrammetric technology. The software includes some functions such as reading the accident image, picking up the calibration points, calibrating, picking up the measurement points, computing the measurement points and mapping. In combination with iWitness and Crash Zone software, Hamzah et al. (2010) reconstructed accident scene using close-range photogrammetric technique to accurately map the crash scenes.

It is difficult to come to a decision for traffic accident judgment just from an accident scene and crash scene diagramming. The statements of the parties in inquiry record are therefore always used to help understand the driving path and direction of the party before traffic accident, the reaction behavior of the party handling vehicle to respond to emergency. The accident is then reconstructed with all the relative materials from crash scene and party statements to infer a conclusion. However, the party statements may not be completely trusted and lead to a distorted accident analysis as the party cannot correctly describe his driving path and reaction behavior because he was terrified during an accident, or the party describes a false statement because he intends to flinch his legal responsibility for an accident. To overcome the problem, a crash simulation constructed on crash scene diagramming can offer the requirements on accident reconstruction and responsibility confirmation of traffic accident. The crash simulation programming in commercial software is well developed. PC-Crash (MEA Forensic Engineers and Scientists, 2012) is a collision and trajectory simulation tool that presents 2D or 3D motor vehicle collisions with its own modulus of crash scene diagramming. Kinematics and dynamics moduli are adopted in the software to simulate vehicle dynamic behaviors. The kinematics modulus is used to calculate the average acceleration of the vehicle from the accelerating or braking force acting on tyres. Then the acceleration is integrated to obtain the velocity and displacement of the vehicle. The dynamics modulus is used to calculate the longitudinal and lateral forces acting on tyres according to the tyre slip angle, accelerating or braking force, and reaction force from suspension system. The forces acted on tyres are then transformed to vehicle body to obtain vehicle's linear and angular acceleration. PC-Crash was first validated by Cliff and Montgomery (1996). The staged collisions were reconstructed using PC-Crash and the trajectories were compared to actual measurements of the skid marks and rest positions. HVE (Engineering Dynamics Corporation, 2012) is a platform for 3D simulation. The EDC's accident reconstruction packages, EDCRASH and EDSMAC, are operated in HVE. EDCRASH calculates impact velocity and impact gravity based on accident side and vehicle damage measurements. EDCRASH is suited for two-vehicle accidents and collisions with immovable barriers. EDSMAC analyzes vehicle response before, during and after impact. Accident investigators can also determinate impact velocity and impact gravity using EDSMAC. M-smac and M-crash (McHenry Software, 2012) are accident reconstruction packages developed by McHenry software, Inc. using SMAC and CRASH3 model, respectively. The packages can present their simulation results on crash scene diagramming plotted using general CAD software. Johnson et al. (2009) reconstructed delta-V, the vehicle change in velocity, for a series of side impact crash tests using reconstruction code CRASH3, and then compared the reconstructed delta-V with the delta-V recorded by the crash test

instrumentation to determine the accuracy of the reconstructed value. WinSMAC and WinCRASH (Trantech Corporation, 2012) in ARSoftware are accident reconstruction programs developed by Trantech Corporation improving SMAC and CRASH3 algorithms for Windows version. The programs can predict velocity change before and after collision and display results in a 2D diagram. WinSMAC and WinCRASH are priced at $769 and $469, respectively. Niehoff and Gabler (2006) investigated the accuracy of WinSmash delta-V estimates as a function of crash mode, vehicle body type, and vehicle stiffness. WinSmash, a direct descendant of crash reconstruction software CRASH3, was found to underestimate delta-V by 23% on average. Johnson and Gabler (2012) further used vehicle damage to estimate absorbed energy and applies momentum conservation to estimate ΔV.

The function and feature of the software for crash scene diagramming and accident reconstruction mentioned above are listed in Table 1. The table indicates that only a few packages own both functions of crash scene diagramming and crash simulation, however, these packages are closed systems. Most packages own one function only, and cannot be extended or integrated with other packages. Therefore, this study developed a Google Map-based accident reconstruction system that consisted of crash scene diagramming and crash simulation. With the system, the crash diagramming can be easily and precisely drawn on a Google map by on-duty police officers using built-in objects from database, and the crash simulation is then clearly animated on the Google map for making a judgment of accident authentication.

METHODS

The system structure of a Google Map-based accident reconstruction system is shown in Figure 1. The system consists of crash scene diagramming and crash simulation. The modulus of crash scene diagramming integrates road network digital maps, Google satellite view, Google SketchUP, and the modulus of crash simulation includes vehicle dynamic simulation and crush simulation programs.

The road network digital maps belonging to Ministry of Transportation and Communication, Taiwan, is a database of map layers with latitude and longitude coordinates. The latitude and longitude coordinates of a location in urban area with an address, an intersection, and a point in rural area without address can be found using different methodologies. By entering address of a location, the latitude and longitude coordinates of the location with address is easily found. By disassembling the names of the streets meeting at an intersection and comparing the words in the street name with database, the latitude and longitude coordinates of the intersection is also easily found. For a point in rural area without address or street name, the coordinate information on Taiwan Power Company's grid numbers, available on every electric pole and switching box throughout Taiwan, can be transformed into latitude and longitude coordinates by grid conversion computation.

With the latitude and longitude coordinates of a location wherever in urban or rural area, the satellite map of an accident site can be obtained from Google's mapping service. The satellite map is then imported into Google SketchUp as a base map, and the modulus of crash scene diagramming is done in the environment of Google SketchUp. Google SketchUp is a 3D model builder software, and it offers functions of line, curve, color etc. in graphic tools to draw traffic lane lines or zebra stripes on a crash scene diagramming easily step by step. In addition, traffic symbols such as cars and trucks, traffic signs and road markings, roadway objects etc. can be built in advance in database. Then a symbol needed in accident reconstruction is selected, stamped onto a diagram, and modified by adjusting its magnitude and direction to simplify the process of drawing traffic symbol. Locating the vehicle after accident and size marking are the last steps to finish a crash scene diagramming. A fixed object such as a traffic light pole in the accident scene is usually used as a datum point to locate the position of the vehicle after accident. After selecting a datum point and importing horizontal and vertical distances between the vehicle's front and rear tyres and the datum point, the accident vehicle can be automatically located to exact position on the diagram in Google SketchUp. Finally, size marking can be done using size marking tool in Google SketchUp.

The vehicle dynamic simulation program calculates driving path before the vehicle crushed. The formulas of vehicle dynamics in the program are derived referring to Light Vehicle Driving System (Andrzej, 1992). Based on Newton-Euler Formulation, the vehicle dynamic differential equations are generated to obtain the vehicle's longitudinal acceleration $\dot{U}$, lateral acceleration $\dot{V}$, and yaw angular acceleration $\dot{r}$:

$$\dot{U}(t_0) = \frac{F_{x1}(t_0) + F_{x2}(t_0) + F_{x3}(t_0) + F_{x4}(t_0)}{m} + V(t_0)r(t_0)$$
$$\dot{V}(t_0) = \frac{F_{y1}(t_0) + F_{y2}(t_0) + F_{y3}(t_0) + F_{y4}(t_0)}{m} - U(t_0)r(t_0) \quad (1)$$
$$\dot{r}(t_0) = \frac{a\left(F_{y1}(t_0) + F_{y2}(t_0)\right) - b\left(F_{y3}(t_0) + F_{y4}(t_0)\right) + \frac{T_f}{2}\left(F_{x2}(t_0) - F_{x1}(t_0)\right) + \frac{T_f}{2}\left(F_{x4}(t_0) - F_{x3}(t_0)\right)}{I_{zz}}$$

where

$$F_{xi}(t_0) = -\frac{1}{4}mga'_x(t_0)\cos\delta_i(t_0), \quad i=1, 2, 3, 4$$

$$F_{yi}(t_0) = -\frac{1}{4}mga'_x(t_0)\sin\delta_i(t_0), \quad i=1, 2, 3, 4$$

F_{xi} and F_{yi} are the force acting on the vehicle's wheel. a'_x is the driving or braking acceleration from accelerator or brake pedal. δ_i is the steer angle of each wheel.

Then the velocity *U*, *V*, *r* of the vehicle are obtained by integrating the vehicle's acceleration:

Table 1. The function and feature of the software for crash scene diagramming and accident reconstruction.

Software	Crash scene diagramming	Crash simulation	Database	Price
Crash Zone	√	√	√	$699
Easy Street Draw	√	—	√	$199
The office of traffic accident management in China	√	—	√	
AnHui Keli Information Industry Co., LTD	√	—	—	
PC-Crash	√	√	√	$4,995
HVE	√	√	√	
m-crash/ m-smac	—	√	—	
WinCRASH/ WinSMAC	—	√	—	$469/$769

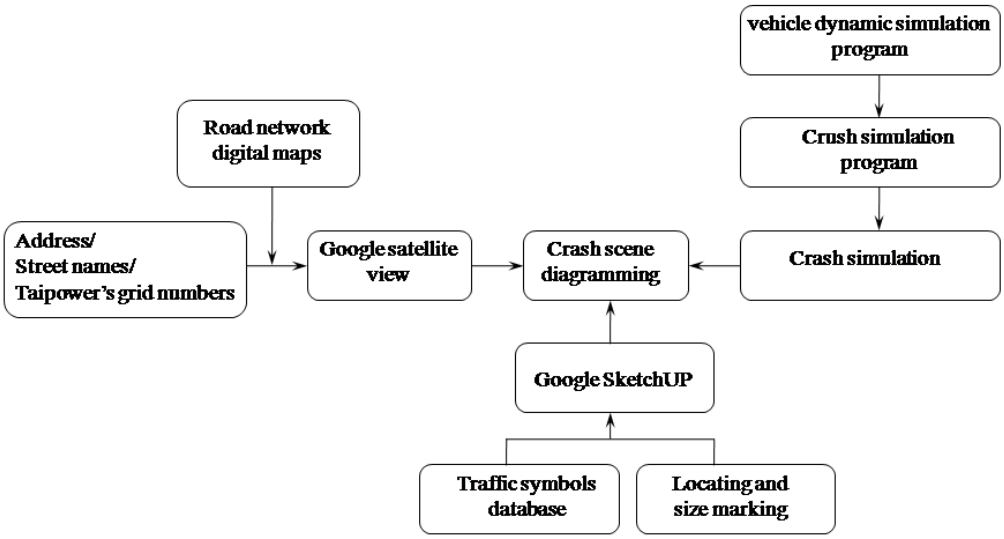

Figure 1. The system structure of a Google Map-based accident reconstruction system.

$$U(t_1) = \dot{U}(t_0)dt + U(t_0)$$
$$V(t_1) = \dot{V}(t_0)dt + V(t_0) \quad (2)$$
$$r(t_1) = \dot{r}(t_0)dt + r(t_0)$$

and the position X, Y, Ψ of the vehicle are obtained by integrating the vehicle's velocity:

$$X(t_1) = [U(t_0)Cos\,\Psi(t_0) - V(t_0)Sin\,\Psi(t_0)]dt + X(t_0)$$
$$Y(t_1) = [U(t_0)Sin\,\Psi(t_0) + V(t_0)Cos\,\Psi(t_0)]dt + Y(t_0) \quad (3)$$
$$\Psi(t_1) = r(t_0)dt + \Psi(t_0)$$

The crush simulation program, based on the law of momentum of conservation, calculates velocity vectors $(\dot{X}'_a, \dot{Y}'_a)$ and yaw angular velocity r'_a of vehicle A after vehicle collision:

$$(\dot{X}'_a(t_n), \dot{Y}'_a(t_n)) = (V'_{Na}x_{ab} + V'_{Ta}x_{ab},\ V'_{Na}y_{ab} - V'_{Ta}y_{ab})$$

$$r'_a(t_n) = r_a(t_n) = r_a \quad (4)$$

Where

$$V'_{Na} = \frac{m_a - em_b}{m_a + m_b}V_{Na} + \frac{(1+e)m_b}{m_a + m_b}V_{Nb}$$

V'_{Na} and V_{Na} are the velocity components of vehicle A in the normal direction of collision plane after and before collision, respectively. m_a and m_b are the mass of vehicle A and B, and e is the coefficient of restitution. $(x_{ab}, -y_{ab})$ is the tangent directional unit vector of collision plane of vehicle A.

The position X_a, Y_a, Ψ_a of the vehicle A after collision are

$$X_a(t_{n+1}) = \dot{X}'_a(t_n)dt + X_a(t_n)$$
$$Y_a(t_{n+1}) = \dot{Y}'_a(t_n)dt + Y_a(t_n) \quad (5)$$
$$\Psi_a(t_{n+1}) = r'_a(t_n)dt + \Psi_a(t_n)$$

The velocity and position of vehicle B after collision are derived in

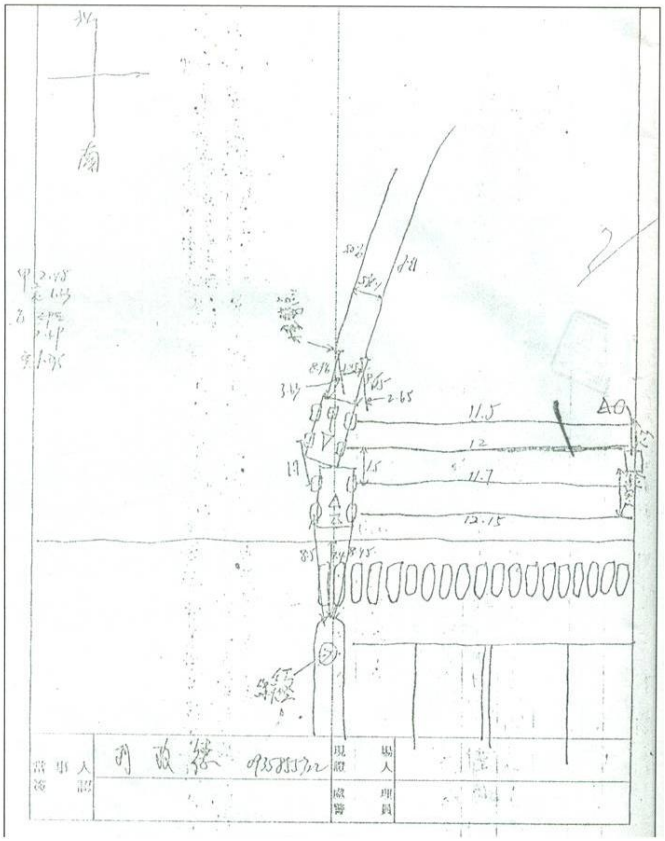

Figure 2. The original hand-drawn crash scene diagramming for a real traffic accident case.

the same process.

RESULTS

Owing to the complexity of traffic accident, the accident reconstruction and analysis are quite difficult. To exclude unreasonable or unexplainable phenomena caused by unpredictable conditions, the validation of the newly developed system in this study first focuses on a relatively simple real case analyzed by a specialist previously (Chen, 2005).

The real traffic accident case for system validation is selected from a case study of crush between two passenger cars (Chen, 2005). The original hand-drawn crash scene diagramming is shown in Figure 2.

Crash scene diagramming

The first step of drawing a crash scene diagramming is downloading a Google Map as a base map. To save time and avoid typing error, a pull-down menu is developed in the system for importing street names. By clicking on the pull-down menu, the names of two streets meeting at the intersection where an accident was happened are selected one by one, as shown in Figure 3a and b. In addition, an application programming interface is programmed to be used as an interface by road network digital maps and Google satellite maps to communicate with each other. Without entering the website of Google Map API Service, Google satellite view and GPS coordinates are directly shown in the system, as shown in Figure 3c and d, using the application programming interface.

The second step is importing the Google satellite view of the intersection where the real accident case as a base map, shown in Figure 4a. Then road markings such as compulsory ahead only, compulsory turn right ahead, yellow box junction etc. beforehand built in the traffic symbol database of Google SketchUp are selected and stamped onto the base map. A crash scene diagramming is finished by adjusting the road marking's magnitude and direction to fit the base map, shown in Figure 4b.

Crush simulation

Follow the driving conditions derived from the analysis in the reference (Chen, 2005); the driving routes and driving behavior sequence of the two passenger cars were set in the system. The ranges of speed entering the intersection are 80~84 and 32~34 km/h, respectively for car A and car B, respectively. By trying out various speeds for car A and car B until the simulation results, including the location of vehicle impact, and the locations of the vehicles coming to rest after impact, coincide with the locations recorded by police at accident scene. It was found that setting the initial velocity of car A and car B entering the intersection to 83 and 34 km/h, respectively results in a simulation relating well with the known facts. Figure 5a~c show the results of simulation presented on the Google map for vehicles before, at, and after crush, respectively.

DISCUSSION

The diagram shown in Figure 2 clearly shows the positions of the two accident vehicles, however, only part of the intersection is drawn. In addition, road dimensions are not recorded completely and road geometry is thus not correct. The drawbacks and mistakes of the hand-drawn crash scene diagramming are clearly revealed by the diagram. As contrasted with the hand-drawn sketch of crash scene from police, it is evident that the proposed system in this study offers more information about the road geometry for further making a judgment on accident authentication. The system is also an accurate, speedy, free and opened software for police officers to manipulate traffic accident.

For the real accident case of crush between two passenger cars, the analysis in the reference (Chen,

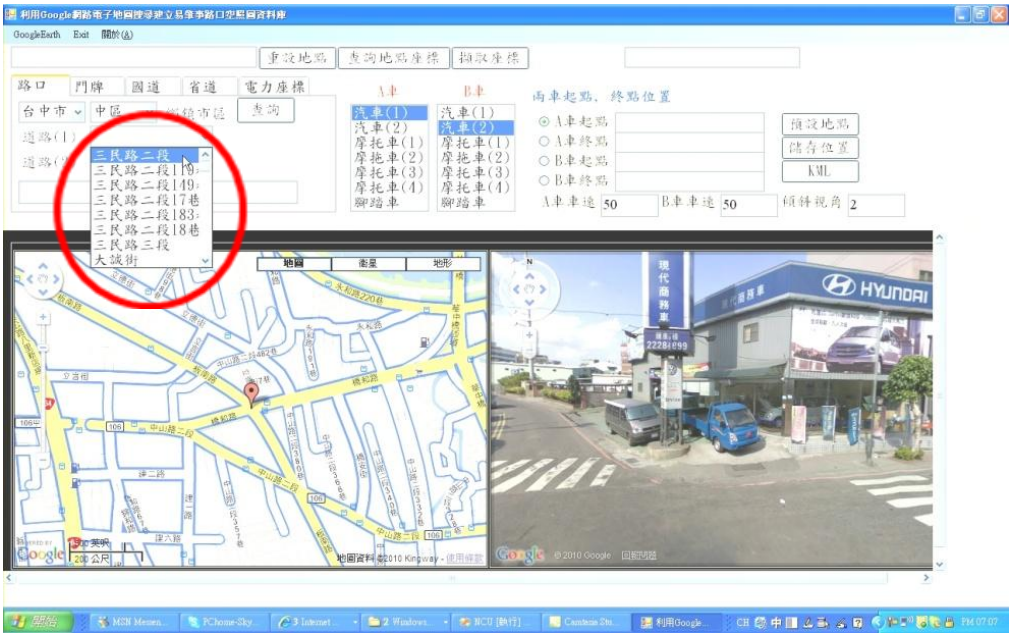

(a)

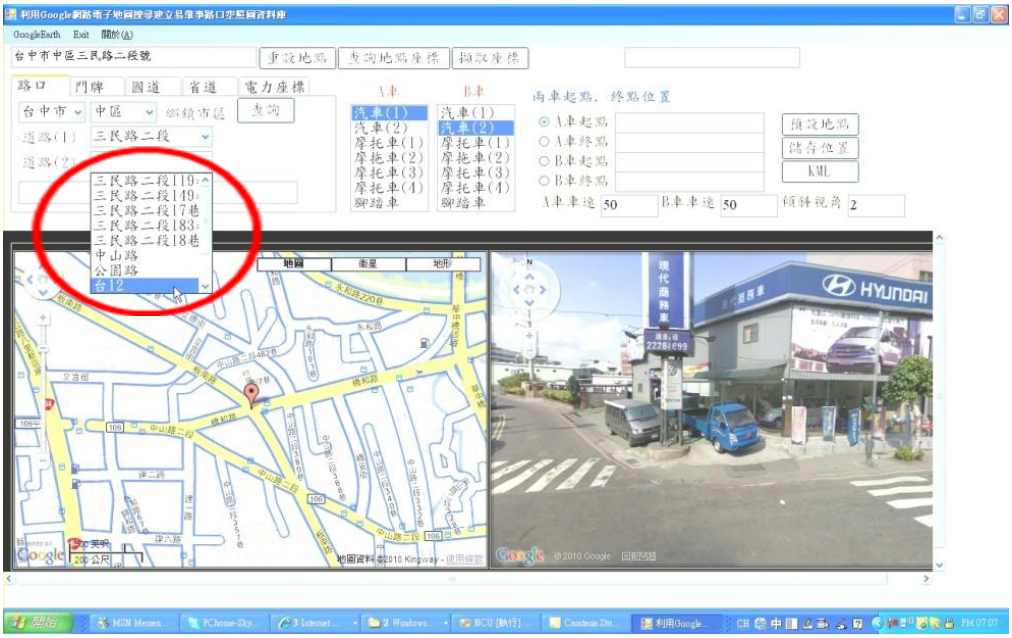

(b)

Figure 3. To select the (a) first and (b) second street name at the intersection where an accident happened by clicking on the pull-down menu.

2005) derived the drivers' behaviors before the crush from reports made by police, and evidences left behind at the accident scene. Car A entered the interaction at the speed of 80~84 km/h, then applied brakes to reduce speed with a deceleration of around 10 m/s^2, and a skid mark was left around 14 m. On the other hand, car B entered the interaction at the speed of 32~34 km/h, then applied brakes to reduce speed with a deceleration of around 10 m/s^2, and a skid mark was left around 4 m. When the two cars collided with each other, the speeds of car A and car B were around 53~58 and 10~15 km/h, respectively. The location of vehicles impact, and the location of vehicles coming to rest after impact, analyzed by the reference are shown in Figure 6. As the initial velocities of car A and car B entering the intersection are set to 83 and 34 km/h in a simulation using the system

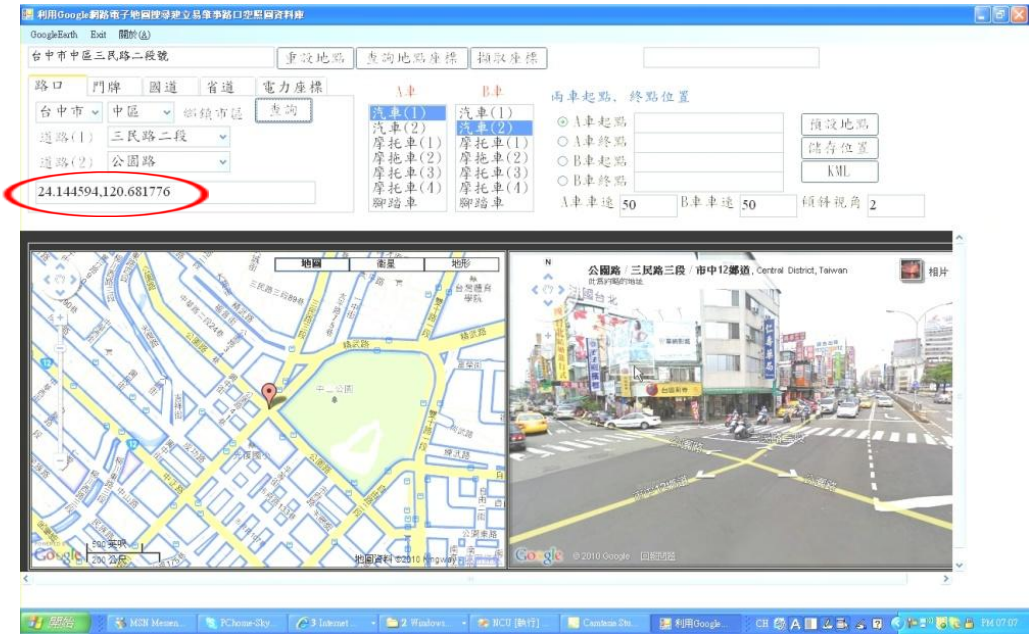

Figure 3c. GPS coordinates are directly shown in the system without entering the website of Google Map API Service.

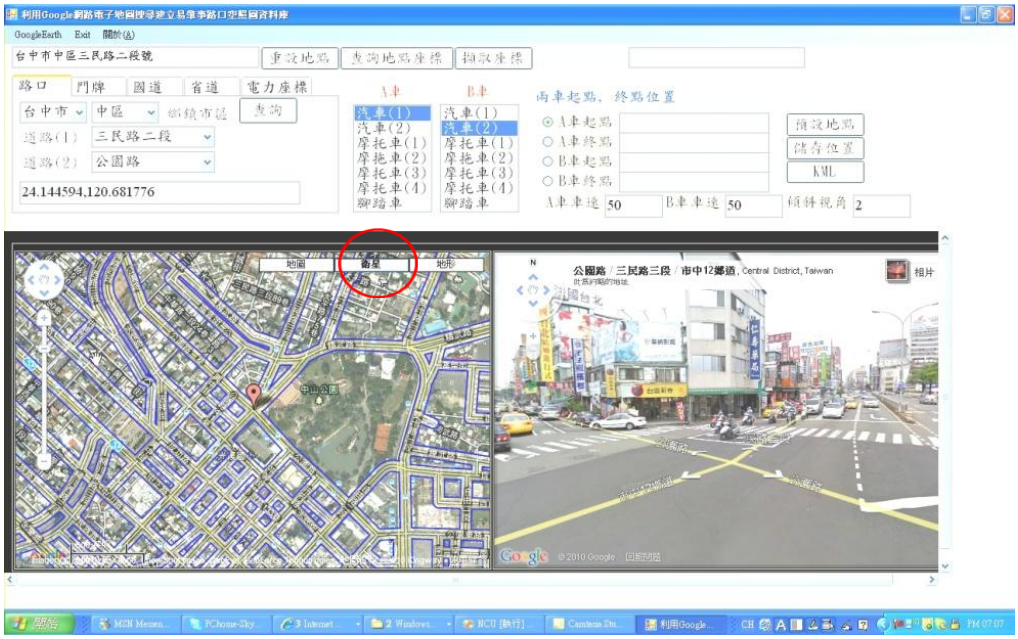

Figure 3d. Google satellite view is directly shown in the system without entering the website of Google Map API Service

proposed in this study, the location of vehicles impact can be presented on the crash scene diagramming. The results are further compared with that from the reference. Figure 7a shows the diagram of vehicle impact location given in this study and that from the reference separately, and Figure 7b is the result of superimposing the two diagrams. The figure shows that the location obtained from this study coincides quite well with that from the reference.

Conclusions

This study developed a Google Map-based accident

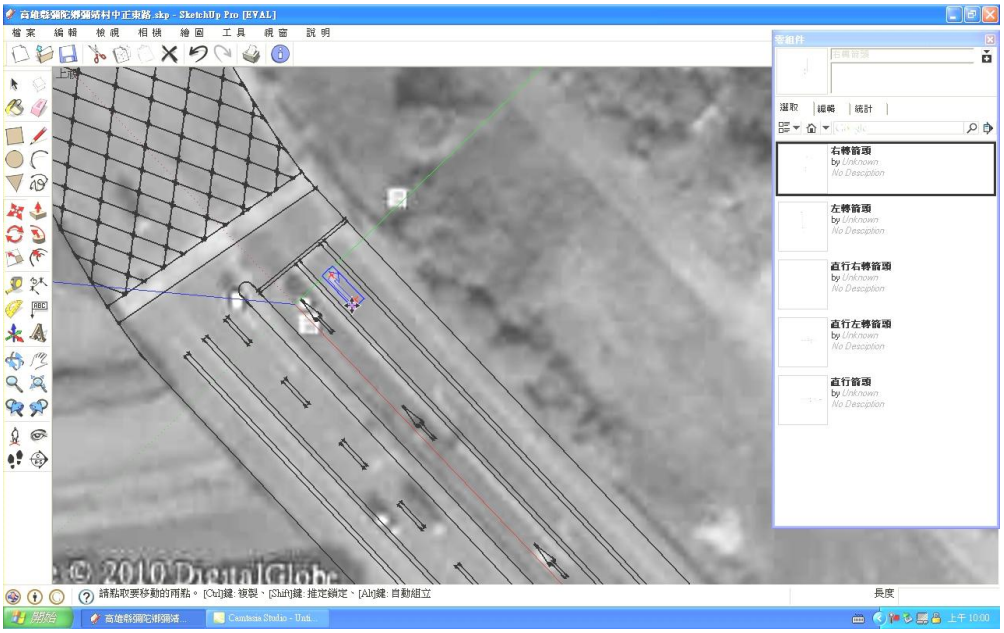

Figure 4a. Importing the Google satellite view of the intersection as a base map and selecting road markings.

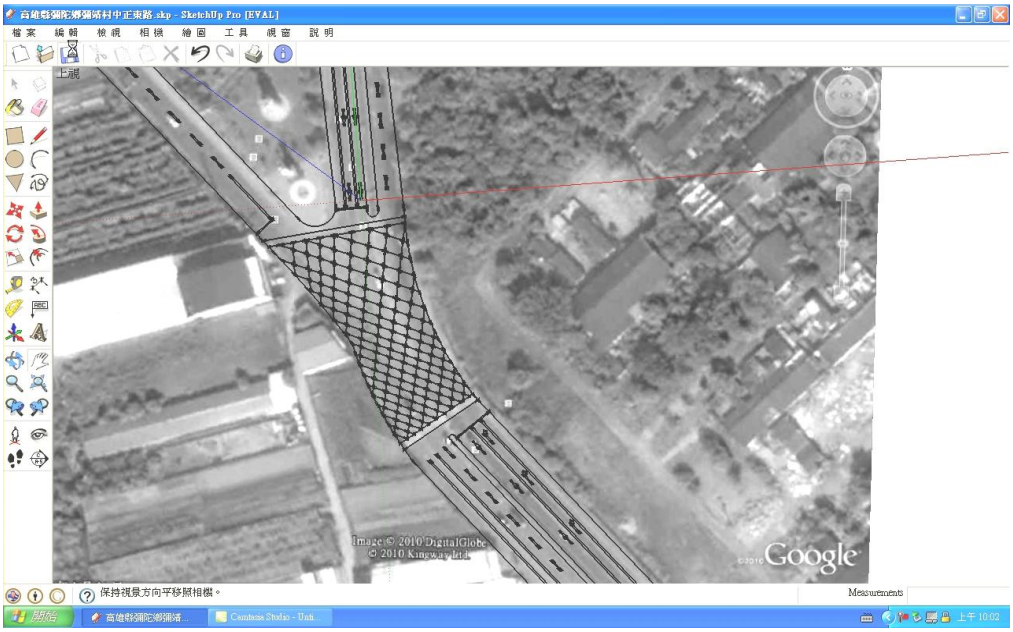

Figure 4b. A finished crash scene diagramming based on Google satellite map.

reconstruction system. The system is a free, opened, and extendable software that consisted of crash scene diagramming and crash simulation. The results are summarized as follows:

1. The modulus of crash scene diagramming integrates road network digital maps, Google satellite view, and Google SketchUP. Without entering the website of Google Map API Service, the Google satellite view and GPS coordinates of the accident location are directly shown in the system by operating a pull-down menu. Then a crash scene diagramming is done in the environment of Google SketchUp by selecting pre-drawn traffic symbols and stamping onto the Google satellite map.
2. The modulus of crash simulation includes vehicle

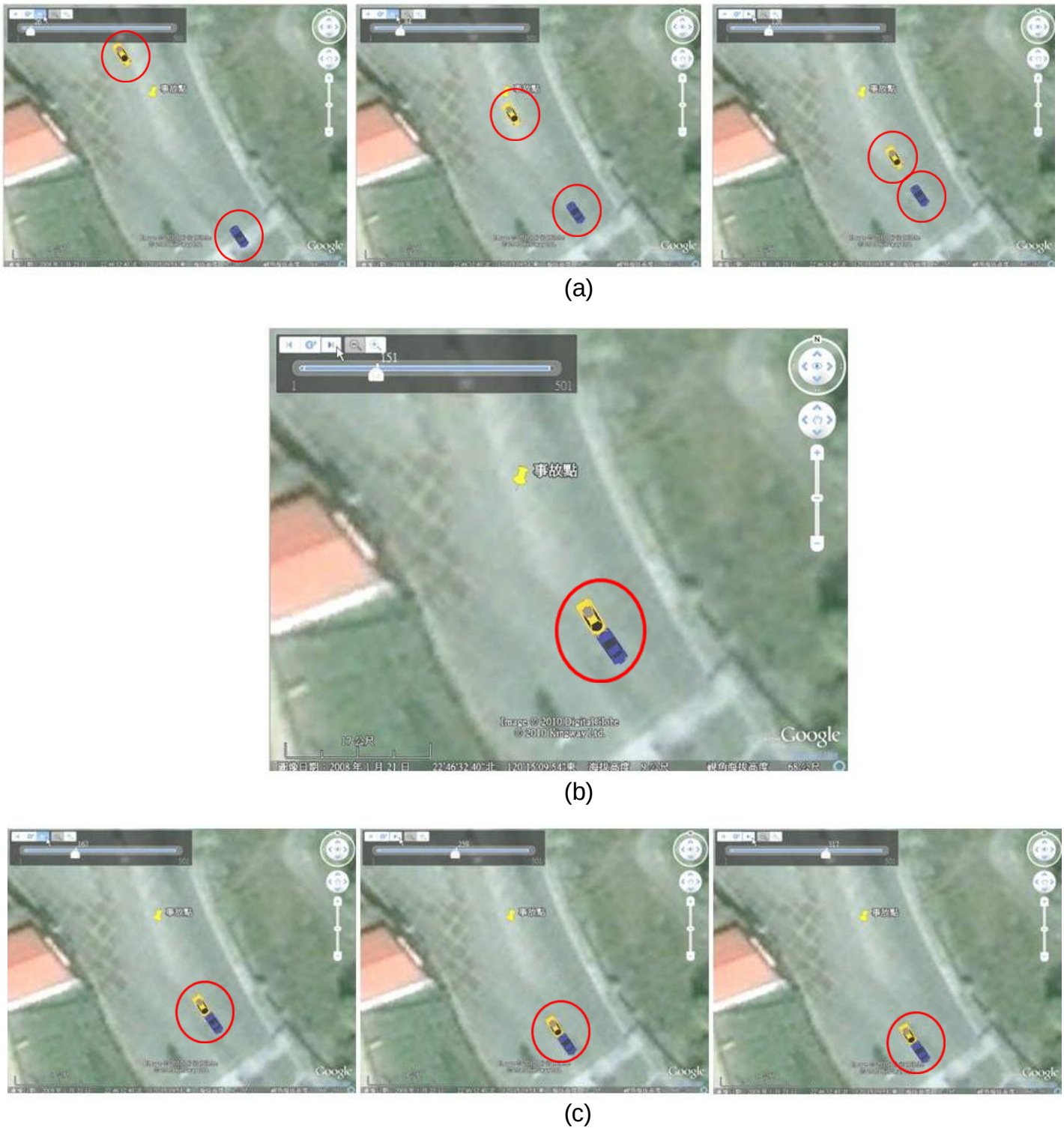

Figure 5. Crush simulation presented on the Google map for vehicles (a) before (b) at, and (c) after crush.

dynamic simulation and crush simulation programs. The vehicle dynamic simulation program calculates driving path before the vehicle crushed based on Newton-Euler Formulation, and the crush simulation program calculates velocity vectors and displacements after vehicle collision using the law of momentum of conservation to predict the vehicle motion.

3. The results of crush simulation could be presented on

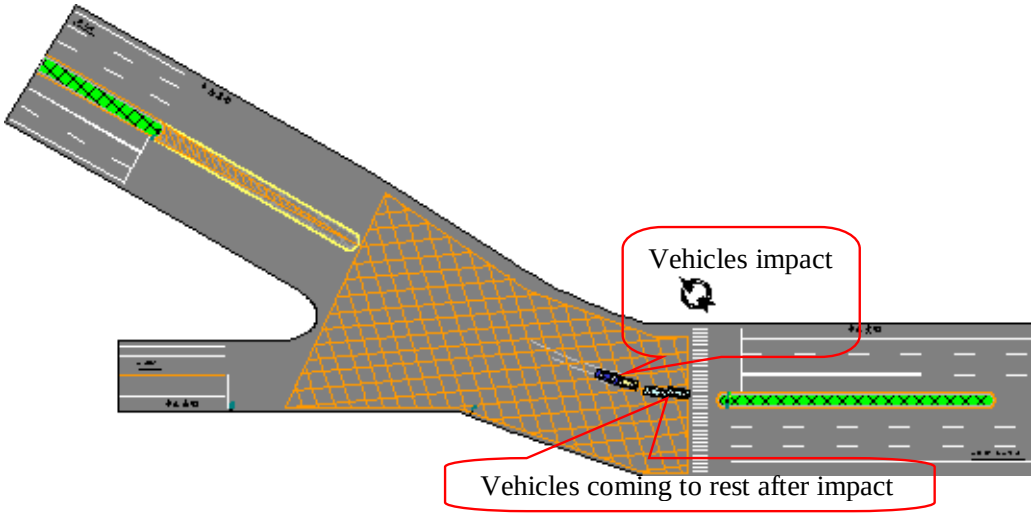

Figure 6. The location of vehicles impact, and the location of vehicles coming to rest after impact, analyzed by the reference.

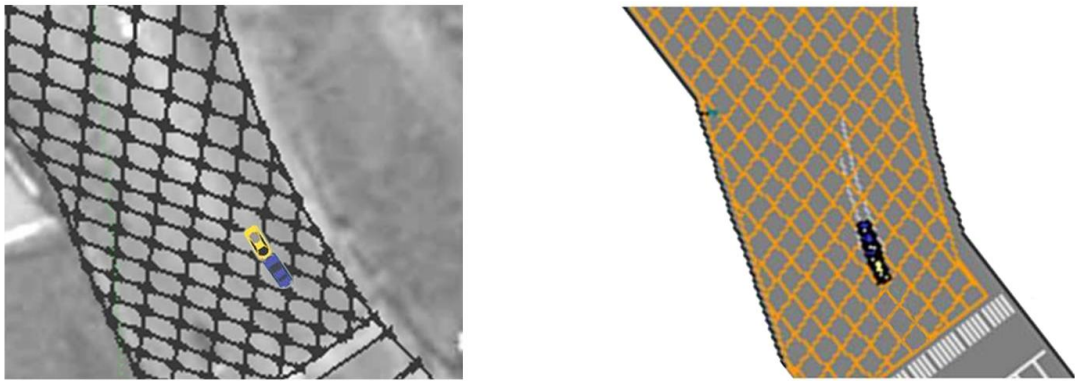

Figure 7a. The diagram of vehicle impact location given in this study (left) and that from the reference (right) separately.

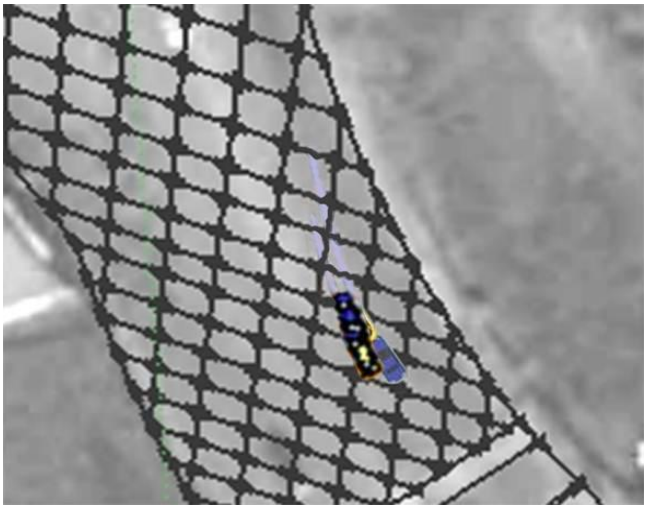

Figure 7b. The result of superimposing the diagram of vehicle impact location given in this study on that from the reference.

the Google map in the form of animation to help people understand or make a judgment for accident authentication.

REFERENCES

Andrzej NG (1992). Develop and Validation of Light Vehicle Dynamics Simulation (LVDS). SAE Paper No. 920056.

AnHui Keli Information Industry Co., LTD (2012). Crash scene diagramming system [online]. Avail from: http://www.ahkeli.com/productcontent.aspx?id=59 [Accessed 12 June 2013].

A-T Solutions Inc. (2012). Easy Street Draw [online]. Avail from: http://www.trancite.com/pro_esd.php [Accessed 12 June, 2013].

Chen KT (2005). Management and authentication of traffic accident (in Chinese). Sun-Wei Press Inc., New Taipei City, Taiwan, pp. 306-329.

Chen Q, Chao KN (2006). Research on Fast Surveying and Mapping System for Road Traffic Accident. J. Shandong Jiaotong Univ. 14:17-21.

Cliff WE, Montgomery DT (1996). Validation of PC-Crash - A Momentum-Based Accident Reconstruction Program. SAE Paper No. 960885.

Engineering Dynamics Corporation (2012). HVE [online]. Available from: http://www.edccorp.com/products/hve.html [Accessed 12 June 2013].
Fenton S, Kerr R (1997). Accident scene diagramming using new photogrammetric technique. SAE Paper No. 970944.
Hamzah NB, Setan H, Majid Z (2010). Reconstruction of traffic accident scene using close-range photogrammetry technique. Geoinf. Sci. J. 10:17-37.
Johnson N, Gabler HC (2012). Accuracy of a damage-based reconstruction method in NHTSA side crash tests. Traffic Inj. Prev. 13:72-80.
Johnson N, Hampton C, Gabler HC (2009). Evaluation of the accuracy of side impact crash test reconstructions. Biomed. Sci. Instrum. 45:250-255.
McHenry Software (2012). M-smac and M-crash [online]. Avail from: http://www.mchenrysoftware.com/ [Accessed 12 June 2013].
MEA Forensic Engineers and Scientists (2012). PC-Crash [online]. Available from: http://www.pc-crash.com/product_pccrash.php [Accessed 12 June 2013].
Niehoff P, Gabler HC (2006). The accuracy of WinSmash delta-V estimates: the influence of vehicle type, stiffness, and impact mode. Annu. Proc. Assoc. Adv. Automot. Med. 50:73-89.
Office of Traffic Accident Management in China (2012). The traffic accident scene scale map software [online]. Available from: http://www.e122.com/drawing.htm [Accessed 12 June 2013].
The CAD Zone, Inc. (2012). Crash Zone [online]. Available from: http://www.cadzone.com/products/the-crash-zone [Accessed 12 June 2013].
Trantech Corporation (2012). WinSMAC and WinCRASH [online]. Avail from: http://www.arsoftware.com/products.htm [Accessed 12 June 2013].

14th International Conference on Accelerator and Large Experimental Physics Control Systems. The Hyatt Regency Embarcadero Center San Francisco, California October 6-11, 2013

December 6-7, 2013 Sydney, Australlia 2013 5th International Conference on Signal Processing Systems

Conferences and Advert

October 2013
14th International Conference on Accelerator and Large Experimental Physics Control Systems. The Hyatt Regency Embarcadero Center San Francisco, California October 6-11, 2013

December 2013
5th International Conference on Signal Processing Systems Sydney, Australlia, December 6-7, 2013

International Journal of Physical Sciences

Related Journals Published by Academic Journals

- *African Journal of Pure and Applied Chemistry*
- *Journal of Internet and Information Systems*
- *Journal of Geology and Mining Research*
- *Journal of Oceanography and Marine Science*
- *Journal of Environmental Chemistry and Ecotoxicology*
- *Journal of Petroleum Technology and Alternative Fuels*

academicJournals